APPLIED COMPUTATIONAL ELECTROMAGNETICS SOCIETY JOURNAL

May 2014
Vol. 29 No. 5
ISSN 1054-4887

The ACES Journal is abstracted in INSPEC, in Engineering Index, DTIC, Science Citation Index Expanded, the Research Alert, and to Current Contents/Engineering, Computing & Technology.

The illustrations on the front cover have been obtained from the research groups at the Department of Electrical Engineering, The University of Mississippi.

EMERITUS EDITORIAL ASSISTANTS

APRIL 2014 REVIEWERS

THE APPLIED COMPUTATIONAL ELECTROMAGNETICS SOCIETY

JOURNAL

Vol. 29 No. 5 May 2014

TABLE OF CONTENTS

Price-Performance Aspects of Accelerating the FDTD Method Using the Vector Processing Programming Paradigm on GPU and Multi-Core Clusters

Robert G. Ilgner and David B. Davidson

Department of Electrical and Electronic Engineering
University of Stellenbosch, Matieland, Private Bag X1, Western Cape, South Africa
bobilgner@gmail.com, davidson@sun.ac.za

Abstract ─ The parallelization of the FDTD on GPUs has become popular due to the low cost, low power and high compute performance achieved with these devices. In recent years, manufacturers of multi-core processors have enhanced the vector processing capability inherent in conventional processing cores, to the extent that these are now contributing considerably to the acceleration of the FDTD and competing with GPUs. This paper will compare the power consumption and purchase cost versus the performance benefits of several parallel FDTD implementations, in order to quantify the effect of parallelizing the FDTD using various processing paradigms. The purchase cost of hardware, computational performance and power consumption are used to compare the parallel FDTD deployments on the BlueGene/P, GPU clusters and the multi-core clusters using SSE. It is shown that the deployment of the parallel FDTD using a hybrid programming paradigm achieves the best computational performance for the lowest purchase cost and power consumption.

Index Terms – AVX, cluster, FDTD, GPU, multi-core, performance, SSE and vector processing.

I. INTRODUCTION

The Finite Difference Time Domain (FDTD) method is inherently highly parallel and has been accelerated by coding the FDTD in parallel form on a variety of platforms. Contemporary examples included the BlueGene/P, multi-core clusters and clusters using Graphical Processing Units (GPU). These systems can all achieve similar computational throughput, depending on the scale of the system. Upfront purchase cost and power consumption are crucial considerations when evaluating high performance computing hardware. Recent years have seen a sustained effort by manufacturers to reduce both, but nonetheless maintain an increase in computational performance [1].

This paper will compare the performance related cost of purchase and power consumed by the FDTD implementations on three different high performance computing architectures. To avoid the effect of scaling on the comparison, computational performance, price and power consumption will be normalized on a per core basis. The FDTD will be implemented using a task parallel method on the BlueGene/P and the multi-core clusters and by a combination of data parallel and task parallel methods; i.e., hybrid methods on the GPU cluster and multi-core clusters. The multi-core clusters make use of their Vector Arithmetic Logic Units (VALU), such as the Streaming SIMD Extensions (SSE) or the Advanced Vector Extensions (AVX), to achieve good performance for the FDTD. The computational performance of these parallelised FDTD implementations will be used to compare the cost and power consumption for the FDTD on high performance computers on a per core basis. These results are the main contribution of this paper, as most results in the literature for parallel FDTD deployments do not compare across entirely different architectures. With the exception of results for an i7-3960x and the GPU cluster (which are taken from the literature), results to be compared were obtained from parallel code

Submitted On: June 18, 2013
Accepted On: April 21, 2014

developed and deployed by the present authors in C on the different platforms. As such, another contribution made by this work is in removing the bias, which can be associated with different programming styles, programming languages and differing test data.

II. PARALLEL FDTD ON HIGH PERFORMANCE COMPUTERS

A. The FDTD method as a computational load

The FDTD method is based on a finite differences approximation of Maxwell's equations in both the time and spatial domains [2]. The computation is performed on a lattice of electric grid values offset by one half a grid spacing from the magnetic grid values. The FDTD remains the most widely-used time domain based Computational Electromagnetic (CEM) solver and overall is one of the most widely-used CEM methods

In the serial form of the FDTD process, program profiling shows that typically more than 98% of the process load is dominated by the repeated calculation of the updated FDTD grid. These calculations are also referred to as iterations, or sometimes leap-frogging and comprise several sets of three level deep computational loops (in three dimensions) [2].

The FDTD process is readily decomposed for parallelisation in either a task parallel or data parallel sense, as described by the methods that follow next.

In this paper, a compute node usually consists of several processors, each processor having several cores, following widely-used terminology in the high performance computing field.

B. Techniques used to parallelise the FDTD method.

Accelerating the FDTD on different architectures requires that the method of parallelisation matches the architecture of the High Performance Computing (HPC) system. There are currently three principal methods used to parallelise the FDTD on specific architectures. These are:

1) Message Passing Interface (MPI) - appropriate for a multi-core cluster or BlueGene [3]. The FDTD is parallelised as independent processing threads that will exchange FDTD grid data between iteration cycles. The MPI interface provides the communication protocol for the exchange of FDTD grid data fringes between successive iterations of the FDTD process [3].
2) openMP - appropriate for multi-core processors or shared memory processors [4,5]. The FDTD is parallelised on the basis of loop parallelism. openMP is a parametric language construct that is embedded in the program code before compilation. The openMP directive spawns FDTD threads that operate in the same memory space.
3) Vector processors or vector processor like architectures - i.e., GPU or vector registers, such as SSE or AVX [6,7,8,9,10,11]. The FDTD grid data is presented to the GPU's streaming multi-core processor as a data array for processing in an SIMD-like manner. Good performance can be achieved by optimizing the SIMD processing on the vector devices by adhering to best practice rules for data alignment and coalescence of the processing cores with the data being computed. Although the processing of the FDTD with a SIMD processor has gained great popularity over recent years with the emergence of the GPU, SIMD processing of the FDTD has been well documented in the literature dating back nearly 20 years [12].

In terms of programming complexity and effort required to code the FDTD with these methods, the rating in Table 1 is based on the subjective experience of programming the FDTD on the respective CHPC systems. A rating of 1 is "best," i.e., implies least effort to parallelise.

Table 1: Coding effort required to parallelise the FDTD

Technique	Implementation Effort
MPI	2
openMP	1
GPU	4
VALU	3

In practice, contemporary HPC systems are a combination of several of these basic architectures. The method with which the FDTD is implemented on these architectures reflects this. As an example, consider the FDTD implemented on a GPU cluster. The GPU cluster hardware

architecture consists of a collection of multi-core nodes using GPUs as acceleration devices. The corresponding parallel FDTD program consists of a data parallel program processing the FDTD on the GPU nodes, with an MPI process providing the communication between the multi-core compute nodes.

III. PARALLEL FDTD IMPLEMENTATIONS

The parallel FDTD implementations on the BlueGene/P, Xeon 5670 cluster and the discrete GPUs described here have been deployed by the present authors on various computing systems of the national South African Centre for High Performance Computing (CHPC), located in Cape Town, South Africa, using code developed by the authors. The results of these implementations are compared to those from a variety of publications as referenced.

The size of the models processed in this paper are limited by the memory available to each node and the extent to which the physical hardware has been scaled. A 32 bit system is obviously at a disadvantage in this respect, in that it will require many more nodes to process the same data volume as a 64 bit system. None the less, all of the multi node systems examined here, process models in the order of several billion grid points.

A. Parallel FDTD on the BlueGene/P

The BlueGene/P is a collective of compute nodes that communicate via a sophisticated interconnect system, as is shown schematically in Fig. 1. The communication interconnect between the compute nodes can be configured to reflect different processing strategies and topologies. The four core PowerPC 450 processors available on this machine each have access to two GB of memory. A schematic of this assembly is shown in Fig. 1.

The BlueGene/P allows the interconnect to be configured to map the topology of the hardware to the requirements of the FDTD. The Torus memory interconnect is particularly suitable for the processing of the 3D FDTD, as the physical topology reflects the structure of the FDTD in a 3D cubic mesh [13,14].

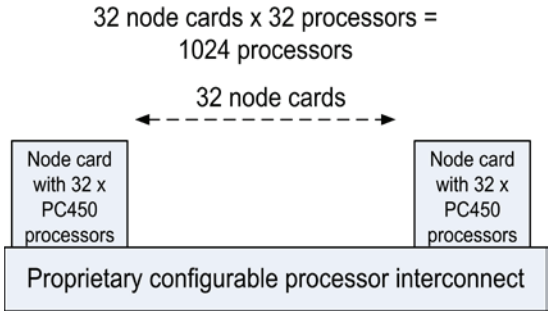

Fig. 1. BlueGene/P architecture as seen by the FDTD application.

The parallel FDTD is built using the MPI application interface. Equal FDTD grid allocations are computed on each processor, one MPI thread per core. Some implementations make use of the shared memory nature of the BlueGene's processing nodes, to process the FDTD grids local to these nodes with the openMP method [14,15]. The efficiency of the FDTD implemented on the BlueGene/P, as described in this paper, is compared to an implementation undertaken for the BlueGene/L (the earlier model of the system) in Fig. 2. The efficiency is calculated as (noting that "ideal" implies linear speed-up):

$$Efficiency(\%) = \frac{Measured\ FDTD\ cell\ throughput}{Ideal\ FDTD\ cell\ throughput} \times 100 \quad (1)$$

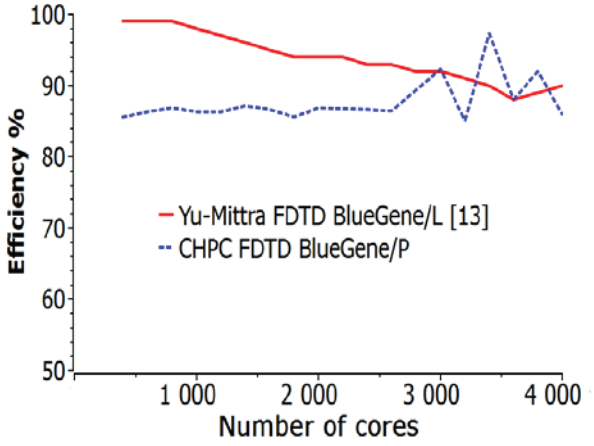

Fig. 2. Efficiency of the FDTD on two BlueGene models with a FDTD grid of two billion cells.

B. Parallel FDTD on the multi-core cluster

The Xeon 5670 cluster computer has the simplest architecture of all the HPC platforms compared here. This cluster is a collection of processors in a blade configuration, as shown schematically in Fig. 3. The blades communicate via a local area network system, the physical network structure comprised by a system of Quad Data Rate (QDR) Infiniband switches (note that some clusters use Ethernet as the interconnect fabric, but proprietary systems such as Infiniband are usually much faster.) The blade configurations are comprised of multi-core chips, which are in themselves tightly coupled using the Quick Path Interconnect (QPI) fabric [16]. It is worthwhile noting that the 6275 Blade configuration allows the memory to be accessed via three physical channels, a feature which greatly improves the access to memory [17] and reduces the data bottleneck experienced by the parallel FDTD on multi-core processors. The QPI fabric will provide cache coherency between the processing cores on all of the CPUs [16] connected with QPI.

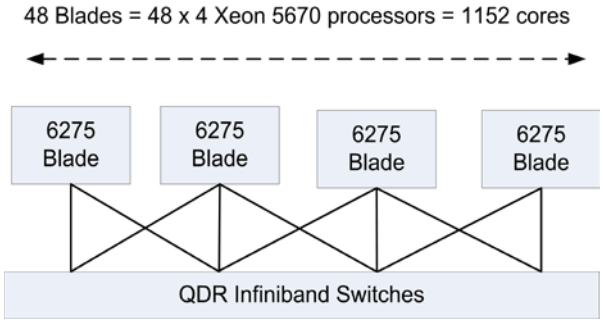

Fig. 3. Schematic architecture of the CHPC multi-core cluster.

All of the blades on the network will contend for network communication bandwidth, as required by the process running on the system. The Infiniband connection does not possess any switching logic to provide features such as parallel memory access to one thread, as is found in interconnects such as the one used by the BlueGene/P.

For this paper, the FDTD is implemented on the clusters using the Message Passing Interface (MPI) threading. The shared memory architecture of the multi-core processors has also been exploited by some [4] to produce hybrid implementations of the FDTD using both the openMP and MPI threading methods.

Figure 4 shows a comparison of the efficiency achieved by the parallel FDTD on a Xeon 5670 multi-core cluster at the CHPC, parallelized using the MPI method.

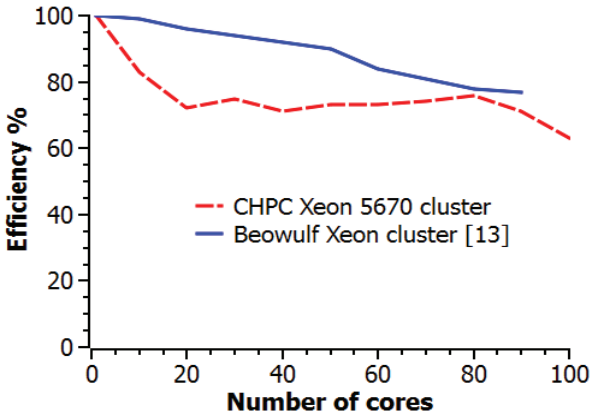

Fig. 4. A comparison of the efficiency of the parallel FDTD with MPI on a cluster at the CHPC with results from [13].

C. Parallelisation using Vector registers on multi-core processors

The SSE and Advanced Vector Extensions (AVX) are also described as Vector Arithmetic Logical Units (VALU) in some publications. Their functionality is based on a collection of vector registers resident on the die of contemporary microprocessor cores. The SSE and AVX registers allow the parallelisation of the FDTD in a data parallel manner [10], by using a Single Instruction Multiple Data (SIMD) approach, as is shown schematically in Fig. 5; i.e., the SSE and AVX can respectively process four or eight single precision floating point values simultaneously [18]. Figure 6 illustrates the benefit in terms of FDTD throughput when processing with AVX on a contemporary four core processor. Figure 7 demonstrates the performance improvement when using SSE on the CHPC's Xeon 5670 clusters. Also shown in Figure 7 is an implementation of the FDTD on a cluster of i7-3960x multi-core processors with the AVX functionality [8]. One particular feature of the i7-3960x's architecture is the presence of four dedicated memory channels supplying data to processors using the processing cores, thereby mitigating the effect of memory

bandwidth bottlenecking associated with processing of large FDTD data sets.

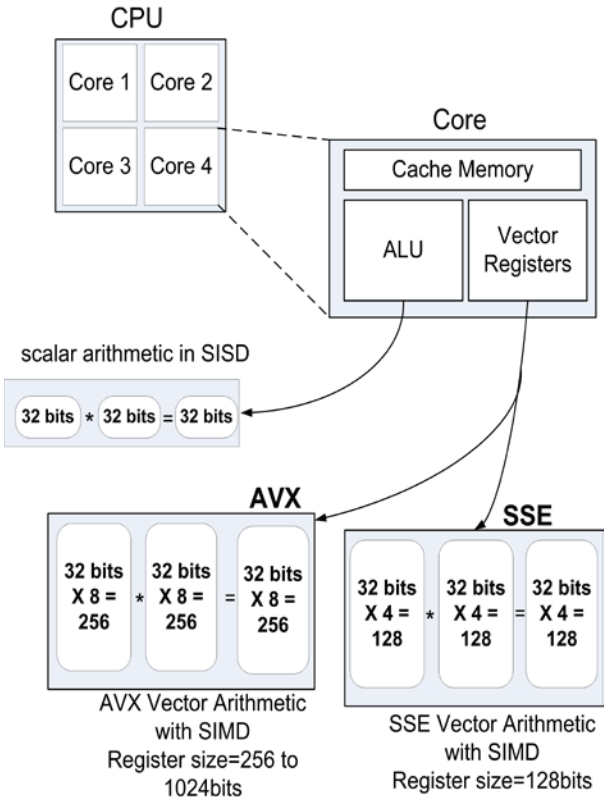

Fig. 5. A comparison of AVX and SSE on a multi-core processor.

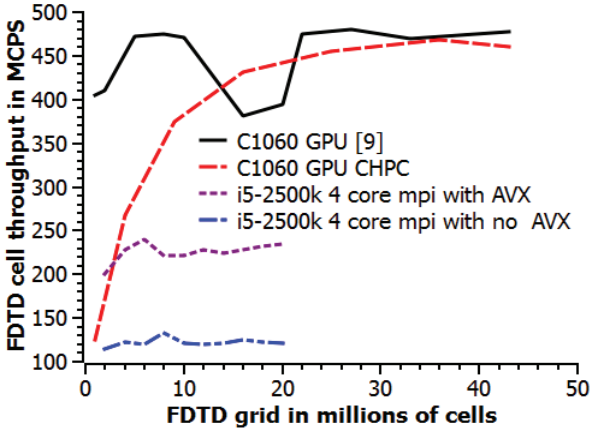

Fig. 6. A comparison of the acceleration of the FDTD on a GPU and on a four core processor using the AVX functionality.

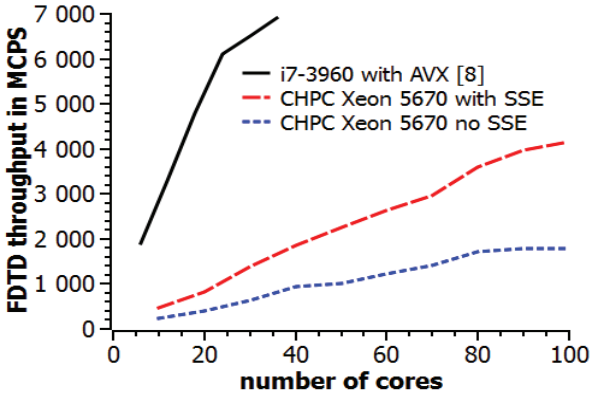

Fig. 7. Comparing AVX and SSE on a cluster.

D. Parallel FDTD on the GPU cluster

The discrete GPU is typically configured to a host computer via a Peripheral Component Interconnect express (PCIe) bus, as is shown in Fig. 8. The cluster GPU architecture shown in Fig. 10 is in effect, still a multi-core cluster architecture and uses the S870 GPU boards as accelerators connected to the multi-core worker nodes.

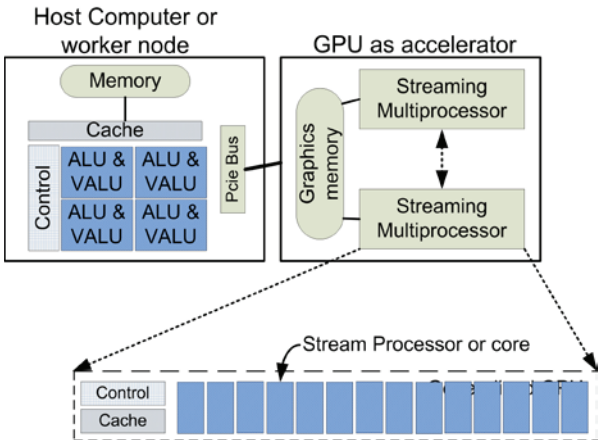

Fig. 8. Discrete GPU attached to host computer consisting of a four core multi-core processor.

The programming of the GPU allows some programming flexibility over and above that provided by the VALU technology [11,19], in that each GPU core or Stream Processor (SP) in Nvidia terminology, is allocated a dedicated program thread [20,21]. All cores in a Streaming Multiprocessor (SM) will execute the same thread.

Figure 8 illustrates the physical relationship between the SP and the SM. Nvidia has coined the term Single Instruction Multiple Threads (SIMT) to differentiate this style of programming from the purist SIMD. The difference between SIMT and SIMD, is that with SIMT one can use conditional (IF) logic within the SIMT program flow. The discrete GPU on its own can achieve good FDTD throughput, as is shown in Figs. 6 and 9. The two GPUs compared in Fig. 9 are NVIDIA's C1060 and the C2070 GPUs. The C2070 has 448 stream processors and 6 GB of global memory, whereas the C1060 has 240 stream processors, as shown in the architectural sketch of Fig. 8. The GPU is programmed in a data parallel sense and optimal performance is gained by the alignment and coalescence of data with the processing cores [7,9,22,23,24,25,26].

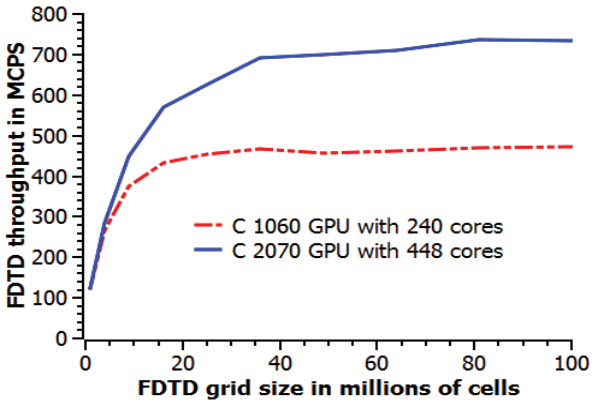

Fig. 9. Performance comparison of the FDTD on two different GPUs.

The architecture in Fig. 10 illustrates the configuration of multiple GPUs attached to a worker node or host PC. The multiple GPUs are attached to the worker node via a dedicated switch, which uses a single PCIe form connection. The CHPC achieves a similar architectural configuration, although individual GPUs are attached to the worker node by dedicated PCIe form factors; i.e., the worker node uses multiple PCIe channels to accommodate several GPUs directly. For these results the GPU used is Nvidia's S870 node, a collection of four low power GPUs, each with 128 stream processors. Power consumption per S870 is a low 800 watt.

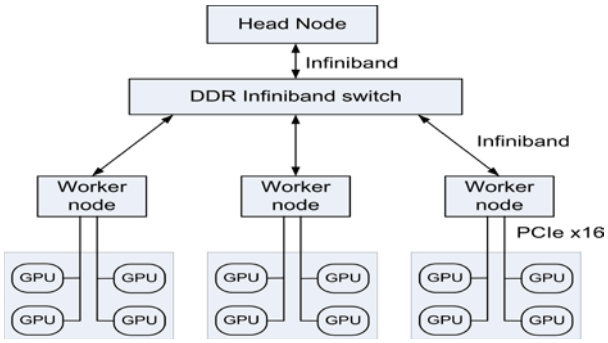

Fig. 10. Schematic of a cluster using GPUs as FDTD accelerators.

The processing of the FDTD on a cluster of GPUs overcomes the memory limitation of processing the FDTD on a single discrete GPU. All of the FDTD data processed by a discrete GPU needs to be transferred on to the GPU's physically dedicated memory before the computation commences. A comparison of the data sizes that the systems described in this paper are capable of processing, is shown in Fig. 11. It must also be born in mind that the data processing capability of a cluster will depend on the scale of a specific system.

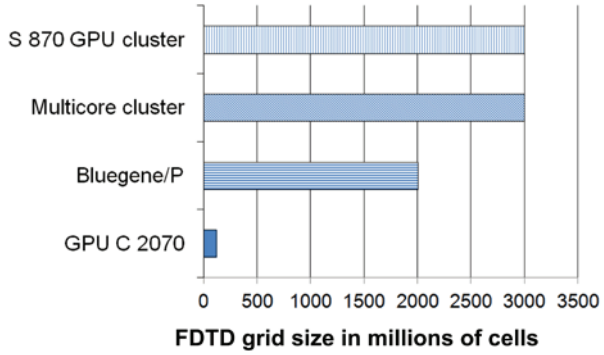

Fig. 11. A comparison of the processing capability of various systems described in the article.

The GPU and multi-core clusters compared in Fig. 12 show very similar performance characteristics for a low number of cores. Both systems compared here show a reduction in efficiency as the number of cores deployed on increases. Of note is the performance of the i7-3960x cluster, which achieves the greatest FDTD throughput per core, as is listed in Table 3.The reduction in efficiency as the size of a system

increases is very probably due to the communication overhead between a larger number of processors.

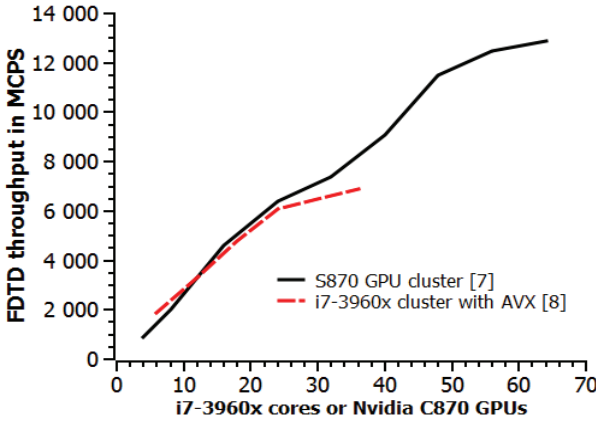

Fig. 12. FDTD throughput compared for a GPU cluster and a cluster using AVX optimised multi-cores.

IV. PERFORMANCE COMPARISON

A. Performance summary

The performance summary in Table 2 is an indication of the computational performance of the parallel FDTD implementations discussed in this paper. The rating used for the performance is the FDTD throughput on the respective platforms, in Millions of Cells Per Second (MCPS). In order to compare the performance on these platforms, the peak MCPS has been normalized on a per core basis, as is shown in Table 3.

Table 2: Computational throughput of the FDTD method on various computing platforms

Platform	Cores	Peak MCPS	Peak MCPS Per Core	Release Date
BlueGene/P	4096	8900	2.2	June 2007
S870 node cluster	8192	12 900	1.6	Mar. 2008
x5670 SSE cluster	100	4155	41.6	Mar. 2010
i7-3960x AVX cluster	36	6900	192	Nov 2011

B. Price and performance

Typical cost of purchase, pricing of HPC systems are shown in Table 3. These pricings were obtained from the Centre of High Performance Computing in Cape Town. The prices given in Table 3 are approximates for the year 2012/2013. Prices have been normalized to the peak FDTD throughput in MCPS per core.

Table 3: Performance/purchase cost comparison. CPS=FDTD grid cells per second.

Platform	Cost In USD 2012	Price Per Core In USD	Peak MCPS	Peak CPS Per USD
BlueGene/P	750000	183	8900	11900
S870 node cluster	46000	6	12900	262000
x5670 cluster	37000	370	4155	112000
i7-3960x cluster	15000	416	6900	462000

The normalized prices show that best computational performance per dollar is achieved by the optimized FDTD using the AVX on the i7-3960x multi-core cluster [8]. The GPU cluster lies in second position and is a better proposition than the BlueGene/P, when considering processing performance for the FDTD. It is not surprising that these performance ratings are all roughly ordered with the age of the hardware, as this accords with Koomey's law.

Two pricing considerations that have not been factored into the study are the maintenance costs for the HPC systems and for the system life expectancy before it is overtaken by newer technology. According to Koomey's law [1], the life cycle of a HPC system may currently be only one to two years before it is overtaken by newer technology.

Large computing systems require sophisticated servicing and sub systems, such as cooling racks and clean rooms. The costs attached to a maintenance plan for a HPC system in terms of capital expenditure and in terms of dependence on a specific vendor are not included in this paper.

C. Power consumption per core

Table 4 shows that for the systems compared in this paper, the multi-core cluster at the CHPC consumes the least power for the performance achieved when processing the parallel FDTD. The variation in the normalized power consumption between the lowest and highest consumers is not large and is a reflection of the low power design criterion for all of these systems.

Table 4: Performance/power comparison

Platform	System Power (kW)	Cores	Power Per Core (W)	MCPS Per W
BlueGene/P	31.5	4096	7.7	0.285
S870 node cluster	16	8192	2.0	0.860
x5670 cluster	4	100	40	1.004
i7-3960x cluster	2	36	56	0.571

The power consumption is a limiting factor for the size of the computing system from the aspect of being able to dissipate enough heat without physically destroying the computing hardware. Larger clusters will need dedicated cooling systems.

V. CONCLUSION

The performance of four parallel FDTD implementations, different in hardware and programming technique, have been compared to show that FDTD deployments accelerated with a combination of vector processing paradigm and the MPI threading interface, presently provide the best performance for cost and best performance for power consumed. However, the comparisons are of course subject to Koomey's law - it would have been instructive to repeat the comparison with a BlueGene/Q, had one been available to the authors (the very high cost of these systems means they are often not readily available, of course). Even with this note, the price/performance and power/performance results are not conclusive because whilst the acceleration of the FDTD on the i7-3960x cluster provides the best performance, it does so at a cost of consuming 50% more power per core than the Xeon 5670 cluster. This work also provides a framework for the comparison of the FDTD on nascent low power technology, such as the Intel Phi.

It should also be noted that memory is another major constraint for the FDTD and one which GPUs have been slow to overcome, due to the relatively small amount of RAM usually associated with a GPU.

ACKNOWLEDGMENT

DBD and RGI acknowledge the support of SKA South Africa, the South African Research Chairs Initiative of the Department of Science and Technology (DST), National Research Foundation (NRF) and the Centre of High Performance Computing.

REFERENCES

[1] J. G. Koomey, S. Berard, M. Sanchez, and H. Wong, "Implications of historical trends in the electrical efficiency of computing," *IEEE Annals of the History of Computing*, vol. 33, pp. 46-54, 2011.

[2] A. Taflove and S. C. Hagness, "Computational electrodynamics: the finite-difference time-domain method," Third Edition*, Artech House*, chapters 3-7, 2005.

[3] C. Guiffaut and K. Mahdjoubi, "A parallel FDTD algorithm using the MPI library," *IEEE Antennas and Propagation Magazine*, vol. 43, no 2, pp. 94-103, April 2001.

[4] D. Luebke, White Paper, "Nvidia® GPU architecture and implications," 2007.

[5] openMP website: available at *http://www.openMP.org*.

[6] W. Yu, X. Yang, Y. Liu, and R. Mittra, "A novel hardware acceleration technique for high performance parallel conformal FDTD method," *27th Annual Review of Progress in Applied Computational Electromagnetics (ACES)*, Virginia, USA, pp. 903-908, March 2011.

[7] S. E. Krakiwsky, L. E. Tumer, and M. M. Okoniewski, "Acceleration of finite-difference time-domain (FDTD) using graphics processor units (GPU)," *IEEE MTT-S International Microwave Symposium Digest*, vol. 2, pp. 1033-1036, June 2004.

[8] W. Simon, A. Lauer, and A. Wien, "FDTD simulations with 10^{11} unknowns using AVX and SSD on a consumer PC," *IEEE Antennas and Propagation Society International Symposium (APSURSI),* Chicago, IL, USA, pp. 1-2, July 2012.

[9] V. Demir and A. Z. Elsherbeni, "Programming finite-difference time-domain for graphics processor units using compute unified device

architecture," *IEEE Antennas and P ropagation Society International Symposium*, Toronto, Ontario, Canada, July 2010.

[10] L. Zhang, X. Yang, and W. Yu, "Enhanced parallel FDTD method using SSE instruction sets," *Applied Computational Electromagnetics Society (ACES) Journal*, vol. 27, no. 1, pp. 1-8, January 2012.

[11] W. Yu and W. Li, "An enhanced hardware acceleration FDTD technique for parallel signal line simulation," *28th Annual Review of Progress in Applied Computational Electromagnetics (ACES)*, Ohio, USA, pp. 411-416, April 2012.

[12] D. B. Davidson and R. W. Ziolkowski, "A connection machine implementation of a three dimensional parallel finite difference time-domain code for electromagnetic field simulation," *International Journal of Numerical Modelling: Electronic Networks, Devices and Fields*, vol. 8, pp. 221-232, 1995.

[13] W. Yu, X. Yang, Y. Liu, L. Ma, T. Su, N. Huang, R. Mittra, R. Maaskant, Y. Lu, Q. Che, R. Lu, and Z. Su, "A new direction in computational electromagnetics: solving large problems using the parallel FDTD on the bluegene/l supercomputer providing teraflop-level performance," *IEEE Antennas and Propagation Magazine*, vol. 50, no. 2, pp. 26-41, April 2008.

[14] W. Yu, M. Hashemi, R. Mittra, D. de Araujo, M. Cases, N. Pham, E. Matoglu, P. Patel, and B. Herrman, "Massively parallel conformal FDTD on a bluegene supercomputer," *IEEE Int. Conf. on Systems, Man and Cybernetic*, San Antonia, Texas, 2009.

[15] M. F. Su, I. El-Kady, D. Bader, and Y. Lin, "A novel FDTD application featuring openMP-MPI hybrid parallelization," *IEEE International Conference on Parallel Processing*, Montreal, QC, Canada, 2004.

[16] R. Maddox, G. Singh, and R. Safranek, "Weaving high performance multiprocessor fabric," *Intel Press*, chapters 1-2, 2009.

[17] U. Drepper, "What every programmer should know about memory," *Swiss Federal Institute of Technology*, 2007, available at: http://www.akkadia.org/drepper/cpumemory.pdf.

[18] W. Yu, X. Yang, Y. Liu, R. Mittra, J. Wang, and W. Yin, "Advanced features to enhance the FDTD method in GEMS simulation software package," *IEEE International Symposium on A ntennas and Propagation (APSURSI)*, Washington, USA, pp. 2728-2731, July 2011.

[19] V. Demir, "An algorithm to improve solution efficiency of FDFD method on GPU," *28th Annual Review of Progress in Applied Computational Electromagnetics (ACES)*, Ohio, USA, pp. 364-369, April 2012.

[20] V. Demir and A. Z. Elsherbeni, "CUDA-openGL interoperability to visualize electromagnetic fields calculated by FDTD," *Applied Computational Electromagnetics Society (ACES) Journal*, vol. 27, no. 2, pp. 206-214, February 2012.

[21] V. Demir, "A stacking scheme to improve the efficiency of finite-difference time-domain solutions on graphics processing units," *Applied Computational Electromagnetics Society (ACES) Journal*, vol. 25, no. 4, pp. 323-330, April 2010.

[22] "CUDA programming manual," available at: http://www/nvidia.com.

[23] J. Stack and Jr., "Accelerating the finite difference time domain (FDTD) method with CUDA," *27th Annual Review of Progress in Applied Computational Electromagnetics (ACES)*, Virginia, USA, pp. 897-902, March 2011.

[24] M. Weldon, L. Maxwell, D. Cyca, M. Hughes, C. Whelan, and M. Okoniewski, "A practical look at GPU-accelerated FDTD performance," *Applied Computational Electromagnetics Society (ACES) Journal*, vol. 25, no. 4, pp. 314-322, April 2010.

[25] M. Ujaldon, "Using GPUs for accelerating electromagnetic simulations," *Applied Computational Electromagnetics Society (ACES) Journal*, vol. 25, no. 4, pp. 294-302, April 2010.

[26] J. Stack, B. Suchoski, and J. Infantolino, "CUDA implementation of moving window finite difference time domain," *28th Annual Review of Progress in Applied Computational Electromagnetics (ACES)*, Ohio, USA, pp. 300-304, April 2012.

Robert G. Ilgner obtained his B.Sc. and B.Sc. (Hons) degrees in Geophysics from the University of Witwatersrand in 1982 and 1983, respectively. As a Geophysicist he conducted geophysical exploration surveys for mining houses. He then worked in London for Siemens in the Information Technology industry building large database systems and received his M.Sc. in 1991 from the University of Surrey in Guildford, UK. He was awarded his Ph.D. from the University of Stellenbosch in 2013. He was employed by Schlumberger in the Seismic division, creating parallel processing applications used for Seismic data reduction and modeling. He built software for the creation of panoramic images and advertising on the internet. He is currently a Postdoctoral Researcher at the University of Stellenbosch.

David B. Davidson received his B.Eng., B.Eng. (Hons) and M.Eng. degrees (all cum laude) from the University of Pretoria, South Africa, in 1982, 1983 and 1986, respectively. He received his Ph.D. degree from the University of Stellenbosch, Stellenbosch, South Africa, in 1991. In 1988, he joined the University of Stellenbosch. As of 2011, he holds the South African Research Chair in Electromagnetic Systems and EMI Mitigation for SKA there. He has held a number of visiting appointments, including at the University of Arizona; Cambridge University, England; Delft University of Technology, The Netherlands and the University of Manchester, England. His main research interest through most of his career has been Computational Electromagnetics (CEM) and he has published extensively on this topic. He is the author of "Computational Electromagnetics for RF and Microwave Engineering" (Cambridge, U.K.: Cambridge Univ. Press, 1st ed., 2005, 2nd ed., 2011). Recently, his interests have expanded to include engineering electromagnetics for radio astronomy. Davidson is a Fellow of the IEEE and a member of the South African Institute of Electrical Engineers and the Applied Computational Electromagnetic Society. He was a recipient of the South African FRD (now NRF) President's Award in 1996. He received the Rector's Award for Excellent Research from the University of Stellenbosch in 2005. He is the editor of the "EM Programmer's Notebook" column of the IEEE Antennas and Propagation Magazine. He was Chair of the local organizing committee of ICEAA'12-IEEE APWC-EEIS'12, held in Cape Town in September 2012.

Radiation from Slotted Cylinder Embedded in Cylindrical Capped Corner Reflector

Hassan A. Ragheb and Essam E. Hassan

Department of Electrical Engineering
King Fahd University of Petroleum and Minerals, Dhahran, Saudi Arabia
hragheb@kfupm.edu.sa, ehassan@kfupm.edu.sa

Abstract ─ An integral equation is formulated for the current distribution on slotted cylinder placed in a cylindrical capped corner reflector. The moment method is used to obtain the current distribution on the antenna conducting surfaces. The radiation pattern of the antenna is then calculated for different corner angles. Interesting results are obtained for different corner angle. The advantage of this geometry over the traditional corner reflector antenna is that it can be part of a ship or aircraft, in which the slotted cylinder is embedded in a conducting corner.

Index Terms - Corner reflector antenna, integral equation formulation and slotted cylinder.

I. INTRODUCTION

Radiation from axial slot on a circular conducing cylinder is the subject of considerable investigations, for its numerous applications in the communication and airspace industry. The residue series and the geometrical optics representation [1], the Green's function formulation [2] and the Fourier integral representation [3] have been employed for analytical treatment of different slots on a circular conducting cylinder. The dielectric coated cylindrical antennas were also investigated using similar methods [4-5]. The concentric case of a dielectric coated slotted conducting cylinder in a ground plane has been also tackled in [6]. Further, radiation from a dielectric coated slotted elliptic cylinder has been also the subject of many investigations [7]-[12]. In all of the previous work, the effect of mounting the antenna on any communication system has not been considered. The present work is generalizing the problem by considering the metallic slotted cylinder embedded in a caped conducting corner. This arrangement can be used to enhance the antenna characteristics and to optimize its radiation pattern. The ground plane can be used to support the slotted conducting circular cylindrical antenna. This plane could be the body of an air craft, a ship or any other mobile system. The integral equation formulation along with the moment method is employed here to obtain the radiation pattern of this antenna. It should be mentioned that an exact solution to this problem has been published by the first author [13]. The difference is in the exact solution the reflector is considered infinitely long, while in the present numerical solution a finite reflector is considered, which is more practical.

II. INTEGRAL EQUATION FORMULATION

A two dimensional cross section of the geometry of the problem is illustrated in Fig. 1. A slotted conducting cylinder of radius "*a*" is embedded in a cylindrical capped corner reflector of corner angle θ extending from $\phi = \theta/2$ to $\phi = -\theta/2$ and cap radius "*b*". The conducting corner planes have finite length "*R*". The axial slot is centered at $\phi = \phi_o$ and has an angular width equals to 2α.

To formulate an integral equation for electric and magnetic current distribution on the surface of the antenna, Green's second identity is employed, i.e.:

$$\oint\!\!\!\oint_{s}\left[G\frac{\partial\psi}{\partial n}-\psi\frac{\partial G}{\partial n}\right]ds = \iiint_{vol.}\left[\psi\nabla^2 G - G\nabla^2\psi\right]dv \quad . \quad (1)$$

Submitted On: May 24, 2013
Accepted On: April 17, 2014

The wave equation can be written as:

$$\nabla^2\psi(\bar{r}) + k^2\psi(\bar{r}) = 0\,. \qquad (2)$$

It is assumed that there is no variation of $\psi(\bar{r})$ along z-direction. Therefore, only one is concerned with a two dimensional Laplcian operator and a two dimensional space (x-y) plane.

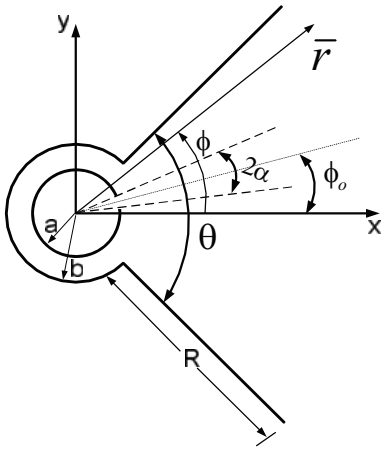

Fig. 1. Geometry of the problem.

The wave equation of an infinite line source of unit density in terms of the Green's function is:

$$\nabla^2 G(\bar{r},\bar{r}') + k^2 G(\bar{r},\bar{r}') = \delta(\bar{r}-\bar{r}')\,. \qquad (3)$$

Multiplying equation (2) by G and equation (3) by $\psi(\bar{r})$ and subtract then using it in (1), consider the two dimensional contour in Fig. 2, it results in:

$$\psi(\bar{r}) = \oint_C \psi(\bar{r})\frac{\partial G(\bar{r},\bar{r}')}{\partial n}d\ell' - \oint_C G(\bar{r},\bar{r}')\frac{\partial \psi(\bar{r})}{\partial n}d\ell' \qquad .(4)$$

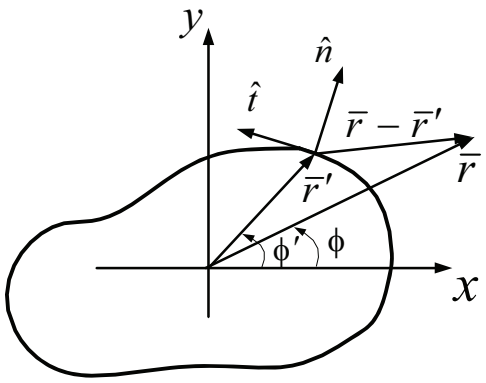

Fig. 2. Contour of a conducting surface.

The scalar function for TM case is associated with the E_z component of the field, i.e.:

$$\psi(\bar{r}) = E_z\,, \qquad (5)$$

$$\bar{H}_T = \frac{-j}{\omega\mu}\frac{\partial\psi}{\partial n}\hat{t} \quad \text{tangential}\,\bar{H}\,. \qquad (6)$$

These field components may then be related to the equivalent surface current by:

$$\bar{M} = \bar{E}\times\hat{n}\,, \qquad (7)$$

$$\bar{J} = \hat{n}\times\bar{H}\,. \qquad (8)$$

Using (5) and (6) in (7) and (8), one obtains:

$$\bar{M} = \psi(\bar{r})\,\hat{t}\,, \qquad (9)$$

$$\bar{J} = \frac{-j}{\omega\mu}\frac{\partial\psi(\bar{r})}{\partial n}\hat{z}\,. \qquad (10)$$

Upon substituting these definitions into the boundary integral equation (4), we obtain:

$$E_z(\bar{r}) = \oint_C M(\bar{r}')\frac{\partial G(\bar{r},\bar{r}')}{\partial n}d\ell' - j\omega\mu\oint_C \bar{J}(\bar{r}')G(\bar{r},\bar{r}')d\ell' \qquad .(11)$$

Equation (11) is the general integral equation for the field component E_z due to equivalent magnetic and electric current sources. On the perfectly conducting surface the total tangential field E_z must vanish. Upon applying this boundary condition, one may get:

$$\int_{\substack{slots\\ only}} E_z(\bar{r}')\frac{\partial G(\bar{r},\bar{r}')}{\partial n}d\ell' - j\omega\mu\oint_{\substack{C\\ except\\ on\ slots}} \bar{J}(\bar{r}')G(\bar{r},\bar{r}')d\ell' = \begin{cases} E_z(\varphi) & on\ slots \\ 0 & otherwise \end{cases}, \qquad (12)$$

where

$$G(\bar{r},\bar{r}') = \frac{1}{4j}H_0(k\,|\,\bar{r}-\bar{r}'\,|)\,. \qquad (13)$$

Equation (12) can be manipulated for the geometry illustrated in Fig. 1, to obtain:

$$-\frac{k}{4j}\int_{slot} E_z(\bar{r}')\frac{a - r\cos(\varphi-\varphi')}{\sqrt{r^2+a^2-2ra\cos(\varphi-\varphi')}}H_1^{(2)}(k\,|\,\bar{r}-\bar{r}'\,|)d\ell' = j\omega\mu\oint_{\substack{C\\ except\\ on\ slot}} \bar{J}(\bar{r}')G(\bar{r},\bar{r}')d\ell' + \begin{cases} E_z(\varphi) & on\ slots \\ 0 & otherwise \end{cases} \qquad .(14)$$

To solve for the current density $J(\bar{r}')$, the conducting surface denoted by the arc length C is divided into N segments ΔC_n and the current density $J(\bar{r}')$ may then be represented by:

$$J = \sum_{n=1}^{N} \alpha_n f_n , \tag{15}$$

where f_n is the basis function defined by:

$$f_n(r) = \begin{cases} 1 & over\ \ \Delta C_n \\ 0 & otherwise \end{cases} .$$

In this case, equation (14) can be re-written as:

$$-\frac{k}{4j}\int_{slot} E_z(\bar{r}')\frac{a - r\cos(\phi-\phi')}{\sqrt{r^2+a^2-2ra\cos(\phi-\phi')}}$$
$$H_1^{(2)}(k\,|\,\bar{r}-\bar{r}'\,|)d\ell'_n = \frac{\omega\mu}{4} \tag{16}$$
$$\sum_{n=1}^{N}\int_{\Delta C}\alpha_n H_0^{(2)}(k\,|\,\bar{r}-\bar{r}'_n)d\ell'_n + \begin{cases} E_z(\phi) & on\ slots \\ 0 & otherwise \end{cases}$$

In order to calculate the unknown coefficients α_n in the above equation, one may discrete the above equation on the conducting surface, i.e. for the m[th] segment:

$$\frac{\omega\mu}{4}\sum_{n=1}^{N}\int_{\Delta C_n}\alpha_n H_0^{(2)}(k\,|\,\bar{r}_m-\bar{r}'_n)d\ell'_n$$
$$= \frac{-k}{4j}\int_{slot} E_z(\bar{r}')\frac{a - r_m\cos(\phi_m-\phi')}{\sqrt{r_m{}^2+a^2-2r_m a\cos(\phi_m-\phi')}}, \tag{17}$$
$$H_1^{(2)}(k\,|\,\bar{r}_m-\bar{r}'\,|)d\ell'_n$$

where m in equation (17) can take values from 1 to N (on the conducting surface only). Equation (17) can be written as:

$$[L_{mn}][\alpha_n] = [G_m], \tag{18}$$

where

$$L_{mn} = -j\eta_o\Delta C_n$$
$$H_0^{(2)}(k\sqrt{(x_m-x_n)^2+(y_m-y_n)^2}) , \tag{19}$$

and for $n=m$

$$L_{mn} = -j\eta_o\Delta C_n\left[1 - j\frac{2}{\pi}\left(\gamma + \ln\left(\frac{\Delta C_n k}{4e}\right)\right)\right], \tag{20}$$

and M is the number of segments on the slot

$$G_m = \sum_{l=1}^{M} E_z(\phi_l)\frac{a - r_m\cos(\phi_m-\phi_l)}{\sqrt{r_m{}^2+a^2-2r_m a\cos(\phi_m-\phi_l)}} \cdot$$
$$H_1^{(2)}(k\,|\,\bar{r}_m-\bar{r}_l\,|)\Delta C_l \tag{21}$$

Upon solving the matrix equation (18), one can obtain the current distribution on the conducting surface and radiation pattern can then be obtained from (11) as:

$$E_z(\bar{r}) = \frac{-k}{4j}\int_{slot} E_z(\bar{r}')\frac{a - r_m\cos(\phi_m-\phi')}{\sqrt{r_m{}^2+a^2-2r_m a\cos(\phi_m-\phi')}}$$
$$H_1^{(2)}(k\,|\,\bar{r}_m-\bar{r}'\,|)d\ell' - \frac{\omega\mu}{4} \tag{22}$$
$$\oint_{\substack{except\\slot}} J(\bar{r}')\,H_0^{(2)}(k\,|\,\bar{r}_m-\bar{r}'_n\,|)d\ell'_n$$

The far field Hankel function can be replaced by its asymptotic expression for large argument, i.e.:

$$H_n^{(2)}(x) = j^n\sqrt{\frac{2}{\pi x}}\,e^{-j(x-\pi/4)} .$$

Also, the approximation $|\,\bar{r}-\bar{r}'\,| = r - r'\cos(\phi-\phi')$ can be used. This gives:

$$E_z(\bar{r}) = \frac{-k}{4j}\int_{slot} E_z(\bar{r}')\frac{\frac{a}{r}-\cos(\phi-\phi')}{\sqrt{1+\left(\frac{a}{r}\right)^2-2\frac{a}{r}\cos(\phi-\phi')}}$$
$$j\sqrt{\frac{2}{\pi k\,|\,\bar{r}-\bar{r}'\,|}}e^{-jk|\bar{r}-\bar{r}'|}e^{j\pi/4}d\ell' \tag{23}$$
$$-\frac{\omega\mu}{4}\oint_{\substack{except\\slot}} J(\bar{r}')\sqrt{\frac{2}{\pi k\,|\,\bar{r}-\bar{r}'\,|}}\,e^{-jk|\bar{r}-\bar{r}'|}e^{j\pi/4}d\ell'$$

Since $r >> a$, the term a/r may be neglected. Employing this approximation one can get:

$$E_z(\bar{r}) = \frac{k}{4}\sqrt{\frac{2}{\pi kr}}e^{j\pi/4}e^{-jkr}$$
$$\left[\int_{slot} E_z(\bar{r}')\cos(\phi-\phi')\,e^{jkr'\cos(\phi-\phi')}d\ell' , \right. \tag{24}$$
$$\left. -\eta_o\oint_{\substack{except\\slot}} J(\bar{r}')\ e^{jkr'\cos(\phi-\phi')|}d\ell'\right]$$

which can be written as:

$$E_z(\bar{r}) = \sqrt{\frac{k}{8\pi r}}e^{j\pi/4}e^{-jkr}f(\phi) , \tag{25}$$

where

$$f(\phi) = \sum_{l=1}^{M} E_z(\phi_l)\cos(\phi-\phi_l)\,e^{jkr_l\cos(\phi-\phi_l)}$$
$$\Delta C_l - \eta_o\sum_{n=1}^{N}\alpha_n e^{jkr_n\cos(\phi-\phi_n)|}\Delta C_n \tag{26}$$

The electric field on the slot may be assumed [6] as:

$$E_z(\phi_1) = E_o \cos\left(\frac{\pi(\phi_1 - \phi_o)}{2\theta}\right). \qquad (27)$$

The circular waveguide can be excited by a probe such that it will propagate the mode, which produces field distribution on the slot given in (27).

III. NUMERICAL RESULTS

To check the accuracy of our computation, comparison between radiation patterns using the numerical solution is presented here and the exact solution in [13] will be presented. Throughout all examples, the slot angle is taken as $2\alpha = 10^o$ centered at $\phi_o = 0$. The geometrical parameters for the following two examples are $a = 0.5\lambda$, $b = 0.6\lambda$ and $R = 3\lambda$.

In Fig. 3, the radiation patterns corresponding to the numerical and the exact solutions for corner angle $\theta = 180^o$ is presented. It is clear that they are in good agreement. The discrepancy after $|\phi| > 65^o$, is due to the fact that in numerical solution the reflector surface is considered finite while in the exact solution it is considered infinite.

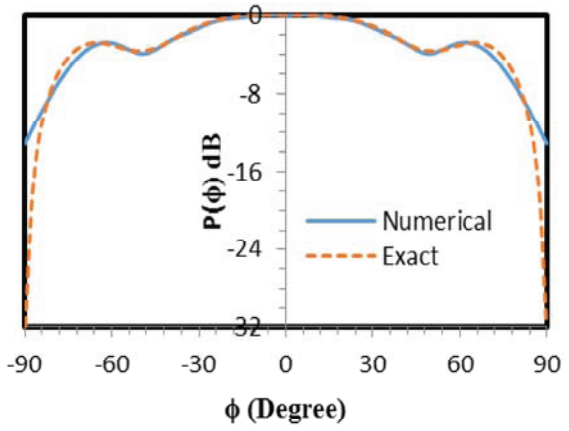

Fig. 3. Comparison between radiation pattern using numerical and exact solutions for corner angle $\theta = 180^o$.

Another example is illustrated in Fig. 4 for the same geometrical parameters of Fig. 3, except that the corner angle here is $\theta = 90^o$. Comparison between numerical and exact solutions is also excellent, except for $|\phi| > 40^o$, due to finite reflector length considered in the numerical solution.

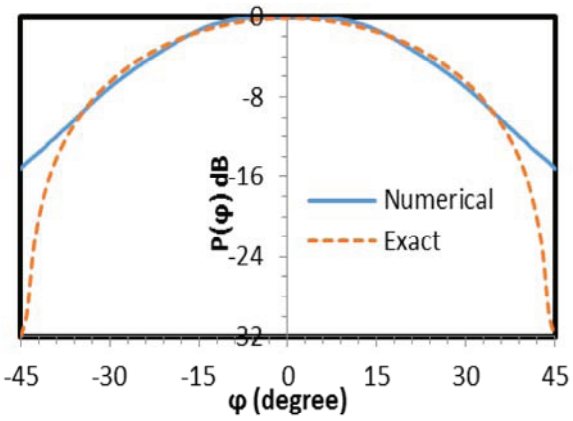

Fig. 4. Comparison between radiation pattern using numerical and exact solutions for corner angle $\theta = 90^o$.

Figure 5 shows the radiation patterns for corner angle $\theta = 180^o$ and geometrical parameters $b = 0.8\lambda$ and $R = 3\lambda$ at different values of slotted cylinder radius.

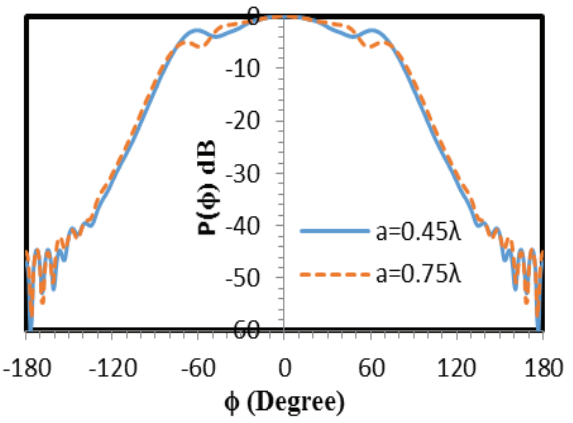

Fig. 5. Radiation patterns for corner angle $\theta = 180^o$ and different slotted cylinder radius.

As can be seen from Fig. 5, the change in radiation pattern is minimal, but as one decreases the corner angle to $\theta = 120^o$ for the same geometrical parameters, the radiation pattern gets

narrower as the slotted cylinder radius gets smaller. This is shown in Fig. 6.

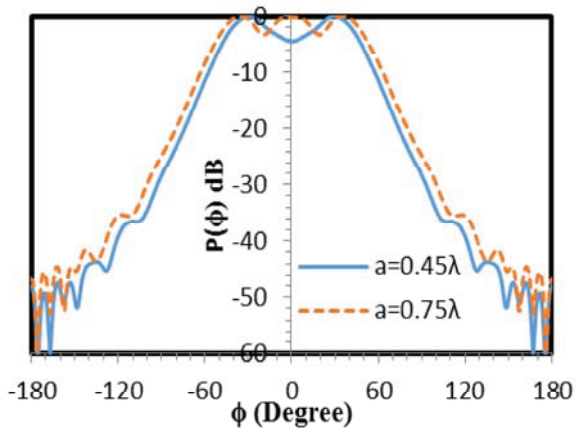

Fig. 6. Radiation patterns for corner angle $\theta = 120^o$ and different slotted cylinder radius.

The radiation patterns corresponding to different slotted cylinder radii, are illustrated in Fig. 7 with the same geometrical parameters as presented earlier, but the corner angle is reduced to $\theta = 90^o$. As one can see from Fig. 7, the smaller the radius of the slotted cylinder, the narrower the radiation pattern is. The deviation between radiation patterns in this case corresponding to lower and upper slotted cylinder radii is the largest in this case.

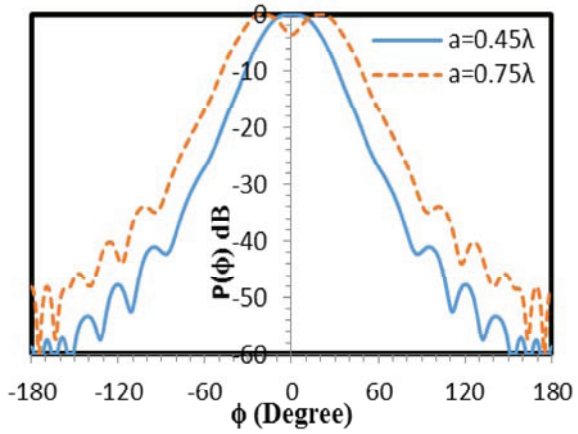

Fig. 7. Radiation patterns for corner angle $\theta = 90^o$ and different slotted cylinder radius.

In the next example shown in Fig. 8, the corner angle is considered as $\theta = 60^o$. Radiation patterns corresponding to different slotted cylinder radii are considered. As shown in this figure, the deviation in radiation patterns in this case is minimal. Accordingly, the above results show that for corner angles between 120^o and 90^o, the radiation pattern gets narrower as the slotted cylinder radius gets smaller.

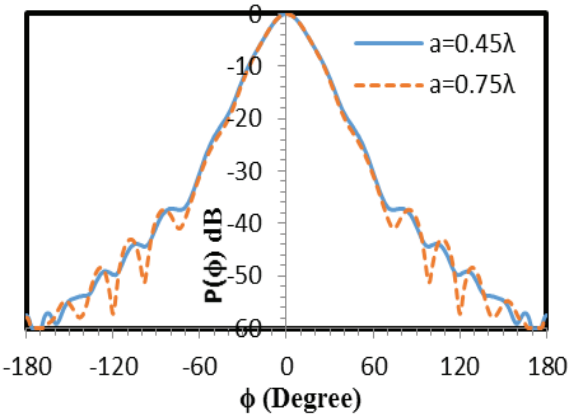

Fig. 8. Radiation patterns for corner angle $\theta = 60^o$ and different slotted cylinder radius.

The final example is for the geometrical parameters $a = 0.45\lambda$, $b = 0.8\lambda$ and $\theta = 90^o$. The radiation patterns corresponding to different reflector length are shown in Fig. 9. The radiation pattern in this case is the same for $-30^o < \phi < 30^o$, while for larger angles the level of the radiation gets higher as the reflector length gets lower.

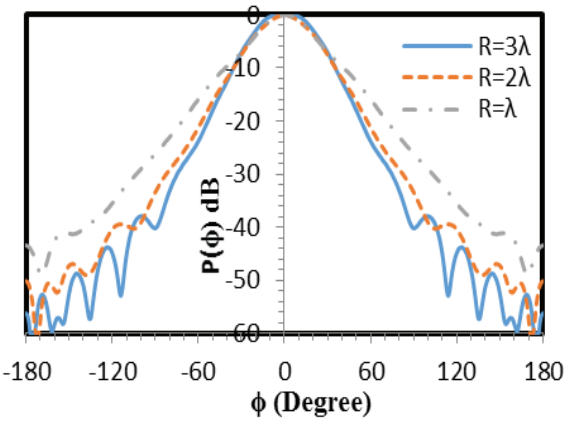

Fig. 9. Radiation patterns for corner angle $\theta = 90^o$ and different reflector length.

CONCLUSION

The axial slot on a conducting circular cylinder embedded in a capped corner reflector has been analyzed. Results corresponding to different geometrical parameters are presented. The geometry is supporting the antenna instead of using the mechanical mounting supporting system. The results show that one can shape the antenna pattern by changing the slotted cylinder radius or the reflector angle.

ACKNOWLEDGMENT

The author would like to thank KFUPM for providing all the facilities required to perform this research, and the financial assistance through the fast track project no. FT-111005.

REFERENCES

[1] S. Sensiper, "Cylindrical radio waves," *IRE Transactions on Antennas and Propagation*, vol. AP-5, pp. 56-70, January 1957.

[2] C. H. Papas, "Radiation from a transverse slot in an infinite cylinder," *J. Of Mathematics and Phys.*, vol. XXVIII, pp. 227-236, 1949.

[3] S. Silver and W. K. Saunders, "The radiation from a transverse rectangular slot in a circular cylinder," *J. Appl. Phys*., vol. 21, pp. 153-158, February 1950.

[4] L. Shafai, "Radiation from an axial slot antenna coated with a homogeneous material," *Canadian J. Of Phys*., vol. 50, pp. 3072-3077, 1972.

[5] W. Crosswell, G. Westrick and C. Knop, "Computations of the aperture admittance of an axial slot on a dielectric coated cylinder," *IEEE Trans. on Antennas and Prop*., vol. AP-20, pp. 89-92, 1972.

[6] H. A. Ragheb and U. M. Johar, "Radiation characteristics of an infinite dielectric-coated axially slotted cylinderical antenna partly embedded in a cround plane," *IEEE Transactions in Microwave Theory and Tech*., vol. MTT-46, pp. 1542-1547, October 1998.

[7] O. Akgol, D. Erricolo, and P. L. E. Uslenghi, "Radiation of a line source by a slotted semielliptical trench filled with DNG metamaterial," *Proceedings 2009 3rd IEEE International Symposium on Microwave, Antenna, Propagation and EMC Technologies for Wireless Communications, MAPE 2009*, art. no. 5355774, pp. 107-110, 2009.

[8] W. Li, J. Qiu, W. Deng, and Y.Suo, "Research on an axially slotted cylinder antenna coated with plasma sheath," *2008 International Conference on Microwave and Millimeter Wave Technology Proceedings, ICMMT* 4, art. no. 4540849, pp. 1875-1878, 2008.

[9] A. K. Hami and M. I. Hussein, "Exact radiation for slotted circular or elliptical antenna coated by a concentric isorefractive metamaterials," *International Journal of Applied Electromagnetics and Mechanics*, 26 (1-2), pp. 101-111, 2007.

[10] D. H. Shin and H. J. Eom, "Radiation from narrow circumferential slots on a conducting circular cylinder," *IEEE Transactions on Antennas and Propagation*, 53 (6), pp. 2081-2088, 2005.

[11] J. Y. Li, J. Li Guo, Y. L. Zou, and Q. Z. Liu, "Analysis of a cylindrical dielectric radome covering omnidirectional waveguide slot antennas," *Applied Computational Electromagnetics Society (ACES) Journal*, vol. 23, no. 2, pp. 166-173, June 2008.

[12] A K. Hamid, M. I. Hussein, and M. Hamid, "Exact radiation by isorefractive slotted elliptic cylindrical antenna," *Applied Computational Electromagnetics Society (ACES) Newsletter*, vol. 22, no. 2, pp. 42-57, 2007.

[13] H. Ragheb, "Radiation from a dielectric coated conducting circular cylinder buried in a conducting corner (TM case)," *Applied Computational Electromagnetic Society Journal*, vol. 28, no. 3, pp. 203-209, March 2013.

Hassan Ragheb was born in Port-Said, Egypt in 1953. He received his B.Sc. degree in Electrical Engineering from Cairo University, Egypt in 1977. He received his M.Sc. and Ph.D. degrees in Electrical Engineering from the University of Manitoba, Winnipeg, Canada, in 1984 and 1987, respectively. From 1987 to 1989, he was a Research Assistant in the Department of Electrical Engineering, University of Manitoba. In 1989, he joined the Department of Electrical Engineering at the King Fahd University of Petroleum and Minerals, where he is now a Professor of Electrical Engineering. His research interests include electromagnetic scattering by multiple and coated objects, micro strip antennas, phased arrays and slot and open ended waveguide antennas.

Essam E. Hassan obtained his B.Sc. from Alexandria University, Egypt in 1970 and his M.Sc. and Ph.D. from the University of Manitoba in 1974 and 1978, respectively. Hassan worked with Northern Telecom Canada in the Digital Switching Division from

1977 to 1979. Since then, he joined the Electrical Engineering Department at King Fahd University of Petroleum and Minerals at Dhahran, Saudi Arabia, where he is now a Professor in the EE Department. He is an author or coauthor of over 50 papers in this field or closely related fields. Hassan's research interests is primarily in the microwave filters and devices and electromagnetic field and anomalous propagation.

Direct Antenna Modulation (DAM) with Switched Patch Antenna– Performance Analysis

Hengzhen Crystal Jing [1], Xiaojing Jessie Xu [2], and Yuanxun Ethan Wang [2]

[1] QuinStar Technology Inc.
Torrance, CA 90505, U.S.A.

[2] Department of Electrical Engineering
University of California at Los Angeles, Los Angeles, CA 90095, U.S.A.
ywang@ee.ucla.edu

Abstract ─ Resonant antennas, such as patch antennas, can be directly modulated with high speed switch devices that were integrated onto the radiation aperture, as the radiation can be turned on or shut off in real-time. Such an antenna is found to be able to radiate pulses with rich spectrum components far beyond the antenna's originally defined bandwidth. In this paper, the efficiency bandwidth product of such an antenna is examined to determine whether it can potentially surpass the usual limit defined by the antenna quality factor. For this purpose, a thorough study on the time-varying behavior of a directly modulated microstrip patch antenna is carried out. The theoretical performance of such an antenna in its radiation power and efficiency is discussed. The time-domain analysis starts with the transmission line model of the patch antenna and the equivalent circuit models. A full-wave Finite Difference Time Domain (FDTD) code that incorporates time-varying switching devices in its mesh is then used to simulate the dynamics of the antenna. The study has demonstrated the capability of improving the radiation efficiency and bandwidth performance over the conventional 1/Q limit, with the so-called Direct Antenna Modulation (DAM) technique.

Index Terms ─ Direct antenna modulation, impulse radio, switched resonator, time-varying systems and ultra-wideband antennas.

I. INTRODUCTION

Ultra-Wideband (UWB) antennas are traditionally designed in the frequency domain by enlarging their impedance matching bandwidth. However, transmitting broadband pulse signals not only requires the antenna to radiate energy across a broad spectrum, but also a linear phase response and a constant radiation pattern over the frequency band so that the pulse shape is not distorted [1-3]. It is difficult for existing broadband antennas to meet these requirements, especially when the antenna dimension is constrained. Recently, Direct Antenna Modulation (DAM) techniques have been proposed to radiate pulses from a narrow band antenna [4-10]. Instead of using the antenna as a passive component of the transmitter, the antenna is directly modulated through turning on and off the integrated switch devices. Different from those in reconfigurable antennas [11-15], the purpose of using switching devices on the antenna in DAM systems, is to create boundary conditions that are varying in real time. A number of experiments [6-8] have demonstrated that a DAM system with a switched microwave patch antenna can radiate rich spectrum components beyond the original antenna bandwidth limit. Similar techniques have been proposed and experimented [16-18] for high power impulse radiations through TEM horn antennas. With DAM techniques, it is possible to simplify the design of a broadband wireless transmitter by transmitting high speed pulses from antennas with low profiles and simple feeding structures or even electrically small antennas [19].

This paper is to study the theoretical potential of the DAM on whether or how it can overcome the conventional limit of efficiency bandwidth product in a high-Q antenna system [20]. In a

Submitted On: June 8, 2013
Accepted On: April 17, 2014

conventional antenna system, the antenna gain and efficiency drops as the radiation bandwidth is enlarged. In a DAM system, the loss of the switches certainly degrades the antenna efficiency to some extent depending on the available semiconductor technology. An even more fundamental loss mechanism in DAM is the energy loss due to the switching action itself, which may happen when a non-zero-voltage capacitor is short-circuited or a non-zero-current inductor is open-circuited. This type of phenomena can not be predicted by frequency domain analyses, but a complete study of the time-domain behavior of the antenna. In this paper, the transient behavior of a directly modulated microstrip patch antenna is obtained in the following three steps. First, the energy building up and release process in the antenna resonator is observed. Second, a bounce diagram analysis with the transmission-line equivalence of the antenna is performed. Lastly, 3-D full-wave simulations are carried out based on a Finite Difference Time Domain (FDTD) code that incorporates non-linear devices in its mesh. From those analyses, the power and efficiency performance is analytically derived and quantitatively evaluated. It is discovered that the energy conversion between the storage mode and radiation mode in time domain dominates the overall performance of the DAM system. To achieve high radiation efficiency, one needs to mount switch devices on one edge of the antenna and switch them at the zero-voltage moment, in order to avoid the energy loss due to the switching action itself. Another interesting phenomenon is that the instantaneous power of the short pulses radiated after switching can be greater than the available source power at the antenna input, which is related to the pulse compression phenomenon of switched resonators [21]. Similar phenomena have also been observed in [16-18].

II. PHYSICAL PRINCIPLE

A microstrip patch antenna integrated with switches is used as an example to test the performance of DAM. The physical structure of the antenna is illustrated in Fig. 1 (a). The length of the patch between two radiation edges is approximately half of a substrate wavelength at the desired radiation frequency. The antenna is excited by a single-tone RF source through a feeding probe, with the frequency coinciding with the antenna's resonant frequency to inject the carrier energy to the antenna, as shown in Fig. 1 (a). A number of switch devices, such as diodes or transistor switches connecting the top patch to the ground plane are mounted at one of the radiation edges, while the other edge is connected to the ground through a perfect conductor strip. The switches are driven by a modulation signal that controls the radiation through the biasing voltages. As it will be explained in the latter sections, short-circuiting the other radiation edge is to provide a complete period of continuous radiation. The two non-radiation edges can be considered to be terminated by Perfect Magnetic Conductor (PMC). Thus, the equivalent cavity model of this particular patch antenna is derived as Fig. 1 (b). When the switches are turned on, the structure behaves like a cavity that resonates at the carrier frequency and supports the TEM mode as its fundamental cavity mode. The radiation behavior of the antenna under switching in real-time is determined by both the antenna's transient behavior and the device's characteristics. A simplified analysis, however, is possible when the process of energy accumulation and release in resonant antennas is followed step-by-step. For example, the following steps are taken for each radiation/storage cycle:

1. Switches are turned on: the patch antenna works as a resonator that starts to accumulate the RF energy at the resonant frequency f_c in the antenna.
2. RF energy is being injected into the antenna resonator. No radiation is created at this stage, except the leakage from non-radiation edges. The antenna operates in a non-radiating resonant mode, which is characterized with a half-sinusoid distribution spatially in its vertically polarized electric field, with two zeros at the edges and the maximum in the center.
3. Energy dissipation in the antenna eventually reaches the same rate as the energy injection. Sources of energy dissipation include Ohmic and dielectric losses of the antenna, leakage from the non-radiation edges and conduction loss on switch devices.
4. Switches are turned off: the previous resonant boundary condition is changed. The electric field at the radiating slot appears immediately and starts to form magnetic currents radiating into the free space. As the

radiation is from the previously stored energy that is accumulated to a great amount, the instantaneous power radiated can be greater than the injected power through pulse compression [21].

5. Radiation continues for a certain period before the discontinuity in the electric field appears at the radiating aperture. The length of the patch determines this delay. For example, the current λ/2 design allows the continuous radiation of one RF cycle without seeing discontinuity in the radiation. The radiated spectrum of monopulse is an ultra-wideband spectrum centered at the injected carrier frequency.
6. When the switch is kept off for more than one RF cycle, the radiated wave will change its phase by 180 degrees for every RF cycle. The radiated spectrum will now be shifted to be clusters around the ($f_c/2$, $3f_c/2$…), instead of the original RF frequency, as it is supported by the λ/4 mode and the odd-integer higher order modes of the patch in the frequency domain.
7. Switches are turned on again after the radiation lasts for an integer number of cycles. The antenna returns to the storage mode at the original resonant frequency.

Therefore, with switches turned on and off in a certain pattern through the above steps, information can be coded into the radiation with modulation methods, such as pulse width or position modulations [22].

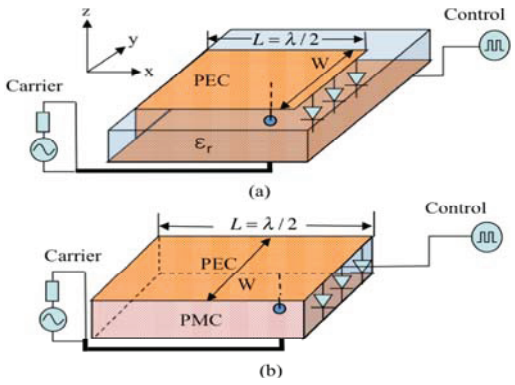

Fig. 1. (a) Physical structure of the patch antenna for pulse transmission and (b) equivalent cavity model of the patch antenna.

III. TRANSMISSION LINE ANALYSIS

The transmission line equivalence model [23] applies when only the dominant mode of the patch is considered and it characterizes the field underneath the patch as a TEM wave bouncing back and forth between the two radiation edges. The model includes the excitation, the short circuit on one of the edges, the switches on the other edge and the radiation impedance of the slot on that edge, as shown in Fig. 2. L is the length of the patch and L_1 is the length between the feeding to the switched edge. R_s is the source impedance in the excitation, R_{on}/R_{off} is the total on/off resistance of the switches and G_r and B_r are the radiation conductance and susceptance of the radiating slot, respectively. It is practical to assume $R_{off} >> R_r$. When the switches are on, the structure becomes a transmission-line resonator with both ends short-circuited. This allows a standing wave between two edges. Once the switches are turned off, the resonant condition changes.

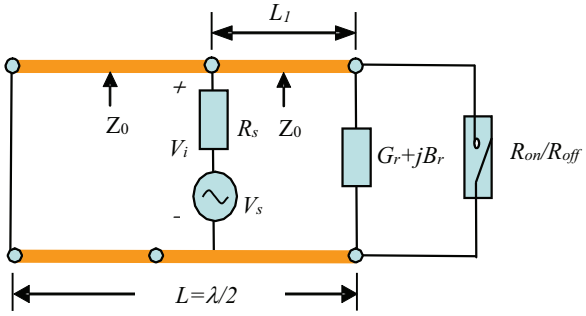

Fig. 2. Transmission line model of the switched mode microstrip antenna.

In order to observe how the field structure evolves in real time following the switching, the standing wave is separated into forward and backward propagating waves and the voltage is formulated in (1);

$$\Phi(t,z) = f^{+}(t,z) + f^{-}(t,z), \tag{1}$$

and

$$f^{+}(t,z) = A^{+}\cos(\omega t - kz), \tag{2a}$$

$$f^{-}(t,z) = A^{-}\cos(\omega t + kz), \tag{2b}$$

where $0 \le z \le L$, A^{+} and A^{-} are the amplitudes of the forward and backward propagating waves. During the switch-on period, the voltage at the two edges satisfies the boundary conditions:

$$\Phi(t, z=0)=0\,, \qquad \Phi(t, z=L)=0, \tag{3}$$

which gives:

$$A^{-}=-A^{+}. \tag{4}$$

This also implies that the forward and backward propagating waves are of equal amplitude and 180-degree phase difference so that they cancel with each other completely on two edges. The final voltage distribution underneath the patch is thus given by:

$$\Phi(t,z)=A^{+}[\cos(\omega t-kz)-\cos(\omega t+kz)]. \tag{5}$$

Once the switches are turned off at the moment t_0, the boundary condition at the radiation edge instantly becomes a high impedance value. This value is approximately given by the radiation impedance of the slot when the edge capacitance is neglected. The reflection coefficient at that edge changes from -1 to approximately 1 and the backward propagating wave is flipped in polarity starting from that moment, e.g., $A^{-}\approx A^{+}$. To reveal how the field structure changes in time-domain, bouncing diagrams for both forward and backward propagating waves are generated as the functions of both time and position in the following:

Case 1: $t_0 \le t < t_0 + T/2$;

$$f^{+}(t,z)=A^{+}\cos(\omega t-kz) \qquad 0\le z\le\frac{\lambda}{2}, \tag{6a}$$

$$f^{-}(t,z)=\begin{cases} -A^{+}\cos(\omega t+kz) & 0\le z<(\frac{\lambda}{2}-\frac{t-t_0}{T}\lambda) \\ A^{+}\cos(\omega t+kz) & (\frac{\lambda}{2}-\frac{t-t_0}{T}\lambda)\le z\le\frac{\lambda}{2} \end{cases}. \tag{6b}$$

Case 2: $t_0 + T/2 \le t < t_0 + T$;

$$f^{+}(t,z)=\begin{cases} -A^{+}\cos(\omega t-kz) & 0\le z<(\frac{t-t_0}{T}\lambda-\frac{\lambda}{2}) \\ A^{+}\cos(\omega t-kz) & (\frac{t-t_0}{T}\lambda-\frac{\lambda}{2})\le z\le\frac{\lambda}{2} \end{cases}, \tag{7a}$$

$$f^{-}(t,z)=A^{+}\cos(\omega t+kz) \qquad 0\le z\le\frac{\lambda}{2}. \tag{7b}$$

The bouncing diagram is simulated in MATLAB based on Eq. (6-7) and plotted in Fig. 3 by setting A^{+}=1. The voltages are combined to demonstrate the final voltage distribution underneath the patch at each snapshot. In each plot, the two dashed lines represent voltage distribution of the forward and the backward propagating waves at a time snapshot along the longitudinal direction, while the solid line indicates the combined voltage. The first plot shows a standing wave pattern as the result of the antenna resonance at the beginning of the time coordinate. Immediately after that, the switches are turned off and the instantaneous voltage distribution is plotted for every quarter of the carrier cycle, as displayed in Fig. 3 (b-f).

It is evident that the voltage at the radiation edge is no longer zero after the switches are turned off, but given by the constructive summation of the two waves. This indicates the emergence of the radiation associated with a non-zero magnetic current on that edge. The magnetic current behaves as a sinusoid function of time and lasts continuously for one RF cycle, as shown in Fig. 3 (b-f). There will be a 180 degree phase shift in the magnetic current after one RF cycle and if the switches remain off, as the voltage discontinuity in the backward wave resulting from switching action arrives at the radiation edge after it has traveled a round trip through the transmission line. Therefore, the switches should be turned on right before the discontinuity happens so that the magnetic current appears as a complete monocycle pulse on the radiating slot. The radiated field is directly related to the magnetic current and should also be a pulse. Therefore, if the edge capacitance is neglected, the radiation can rapidly start and stop without the typical delay caused by the high-Q bandpass behavior of the patch antenna.

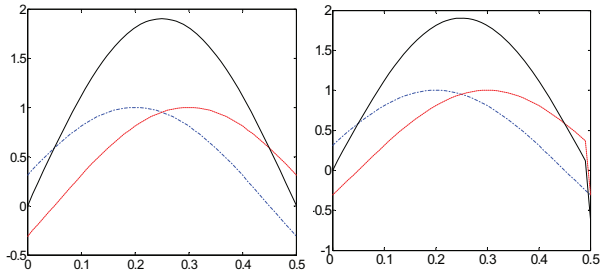

(a) $t=0^{-}T$ (switch on) (b) $t=0^{+}T$ (switch off)

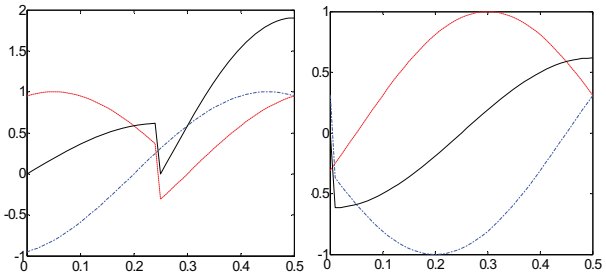

(c) $t=1/4T$ (d) $t=1/2T$

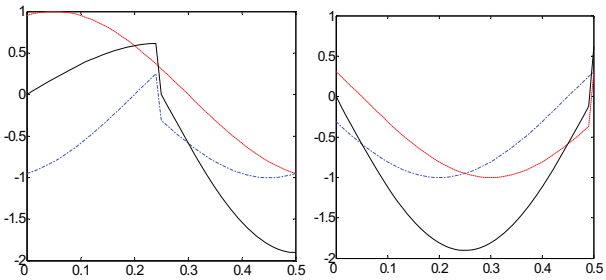

(e) *t=3/4T* (f) *t=1T*

Fig. 3. Time variation of the voltage distribution along the longitudinal direction underneath the patch during the switching process (forward –-, backward --- and total —).

IV. PULSE COMPRESSION AND RADIATION

According to the analysis in section II, the instantaneous power from the antenna in a DAM system radiated immediately after the switches are turned off, which is determined by the initial energy stored in the non-radiating mode. The amount of stored energy is related to the charging time and the Q-factor of the antenna resonator for the switch-on case. If lower on-resistance switches (higher Q-factors) and longer charge times are used, the instantaneously radiated power over a short duration can be greater than that of conventional patch antennas driven by a single-tone carrier. This is the so-called pulse compression phenomenon which exists in many switched resonant structures and has been well described in [20]. For the same amount of input power, one may define the pulse compression gain as the ratio between the instantaneously radiated power during the pulse-on period in the DAM scheme, versus the radiated power in a conventional antenna. The pulse compression gain generally increases when a longer charging time is used until the antenna resonator is fully charged, whereas the maximum pulse compression gain is reached. The maximum achievable pulse compression gain is related to the energy storage capacity of the antenna. For an antenna represented by the transmission line model in Fig. 2, the maximum pulse compression gain is derived to be [See Appendix I]:

$$G_{pulse,\max} = \frac{Z_0^2}{R_{on} R_r}. \tag{8}$$

The maximum pulse compression gain is higher than 1 when the following condition is satisfied:

$$R_{on} < \frac{Z_0^{\,2}}{R_r}, \tag{9}$$

which necessitates high-speed and low-resistance switches. The gain does not come from any active device, but from the energy compression into shorter time duration by the direct antenna modulation scheme. The pulse compression gain relationship denoted by (8) can be generalized in terms of the Q factors of the antenna resonator. The antenna operates alternatively between the storage phase and the radiation phase. In the storage phase, the switches are on and the field behaves in a half wavelength transmission line resonator mode, while in the radiation phase the switches are turned off and the field follows a quarter-wave transmission line resonator mode. By ignoring the edge susceptance, one can find that the Q factors of the transmission line resonators for the switch-on and off cases are given by:

$$\begin{cases} Q_{on} = \dfrac{\pi}{4}\dfrac{Z_0}{R_{on}} & \text{(switch on or pulse off)} \\ Q_{off} = \dfrac{\pi}{4}\dfrac{R_r}{Z_0} & \text{(switch off or pulse on)} \end{cases}. \tag{10}$$

In conjunction with (8), it leads to:

$$G_{pulse,\max} = \frac{Q_{on}}{Q_{off}}, \tag{11}$$

which is a general expression of the pulse compression gain independent of antenna structures. From (11), it is obvious that in order to achieve a high pulse compression gain, one needs to keep the highest possible Q in the storage mode and the lowest possible Q in the radiation mode. The former requires minimizing the dissipation of the antenna cavity associated with the metal loss, dielectric loss and the switch-on resistance, as well as the leakage from the non-radiation edges. The latter is determined by how easily the antenna can couple the energy into the free space, on which regular bandwidth enhancement techniques such as using lower dielectric constants, wider patches and thicker substrates can be applied.

V. RADIATION EFFICIENCY ANALYSIS

It is well known that the efficiency bandwidth product in a conventional resonant antenna is approximately given by the inverse of the Q-factor

of the antenna [21]. One of essential merits of a DAM system is its better efficiency and bandwidth tradeoff relationship in transmission than that of conventional antennas, at the price of requiring special radiation waveforms and modulation formats. To obtain an efficiency bandwidth product greater than the usual limit, the switched patch antenna shown in Fig. 1 must radiate pulses for integer number of RF cycles. The position and the repetition rate of the pulses can be coded with the information to be transmitted [22]. Differing from conventional antennas, the radiation efficiency of a DAM system is defined as the ratio of the total radiated energy during the radiation period of each pulse $T_{r,pulse}$, to the total injected energy into the patch antenna during each Pulse Repetition Period (PRP). For pulse width or pulse position modulations, the data rate *C* is related to *PRP* as follows:

$$C = \frac{2}{PRP} \quad (bits/s). \tag{12}$$

The radiation efficiency can be evaluated by analyzing the charging and discharging behavior, based on the equivalent circuit models of the antenna during switch-on and off states. The complete derivation of the radiation efficiency of the DAM system based on the switched patch antenna is included in Appendix II. It concludes that the radiation efficiency for a given data rate *C* is as follows:

$$Eff_r = \frac{1}{\frac{1}{\xi} + (\frac{2}{CT_{r,pulse}} - 1)\frac{2Q_{off}}{Q_{on}}}, \tag{13}$$

ξ is the radiation-to-loss ratio of the radiation slot, defined as the total radiated energy over the total energy lost from the antenna in each RF cycle, including both the effective RF radiation and the dissipation caused by the switching action itself. A less than unit ξ indicates the dissipation of energy stored in the parasitic reactance surrounding the radiation slot due to the switching action, in the form of either spiky current flowing through the switch devices or spurious radiation into the free space. Q_{on} and Q_{off} are the intrinsic quality factors of the patch antenna resonator in the charging and discharging modes. (13) indicates that the maximum radiation efficiency of the DAM system is limited by the radiation-to-loss ratio ξ of the radiation edge. As the parasitic reactance of the radiation edge is often capacitive, one could maximize ξ by switching at the zero voltage moment if the carrier and the switching control can be synchronized with a phase locked loop. The zero voltage switching principle is similar to that in a high efficiency Class-E power amplifier [24]. In general, however, it is hard to achieve a high ξ for the patch antenna due to the complex nature of the parasitic effect at the radiation edge. Beside the limitation of ξ, either higher ratio of Q_{on} to Q_{off} or higher data rate *C* helps to achieve higher radiation efficiency, in contrast to a conventional antenna system where smaller bandwidth results in better efficiency. This is because the efficiency degradation in a DAM system is mainly caused by the resistive dissipation of switch devices. The loss is more significant when a longer charging period or PRP is used.

VI. SIMULATION RESULTS

To predict the performance of a DAM system, one needs to observe the interactions of waves and devices in the time-domain. For this purpose, a 3-D full wave simulator that incorporates switch models and resistive voltage sources is developed based on the extension of conventional 3-D dimensional FDTD algorithms [25]. A perfectly matched layer boundary condition is chosen to truncate the FDTD lattices. The time-domain near-to-far-field transformation approach described in [25], is implemented to obtain the time-domain radiation waveforms in the far field. The patch antenna is with dimensions of L=40.64 mm, W=80.77 mm, H=1.524 mm and the dielectric constant of the substrate ε_r = 2.33. 20 RF switch devices are mounted in parallel with uniform spacing 2.322 mm on the radiation edge of the antenna. Each RF switch device is chosen to have 0.2 Ω switch-on resistance and 2 MΩ switch-off resistance; therefore, the total switch-on/off resistance of the edge is 0.01 Ω and 20 kΩ, respectively. The resonant frequency during the switch-on period is 2.414 GHz. Figure 4 shows the FDTD simulation setup of the switched patch antenna. The antenna structure is discretized into 20×21×1 cells along X, Y and Z directions with the unit cell size of $2.032 \times 2.322 \times 1.524$ mm^3. The corresponding time step is $\Delta t = 3.6 ps$, which satisfies the Curant's stability criterion. 10-layer

Uniaxial Perfect Matched Layer (UPML) boundary conditions are used to truncate the FDTD lattices, which are placed at 16 cells away from the six sides of the antenna structure. The switching behavior is simulated by assuming the resistance of the switch varies from the switch-on value to the switch-off value according to an exponential function or vice versa. The transition time is 0.054 ns, which is about $1/8^{th}$ of the RF carrier cycle. The voltage source supplies a RF voltage of +/-10V and the source impedance of 160 Ω is used. The source is placed at the position shown in Fig. 5 to provide critical coupling at the feeding point to the antenna cavity. This means a perfect impedance match is obtained between the source and the load, e.g., the on-resistance of the switches in the steady state. Both RF switches and resistive voltage sources are formulated according to the modified FDTD updating equations for lumped element circuits in [25].

Both the original patch antenna and its cavity equivalent version in Fig. 1 are simulated. However, the strong leakage in the non-radiating slots in the original antenna limits the amount of energy storage during the switch-on period. Very little pulse compression gain (~2 dB maximum) can be achieved. To demonstrate a strong pulse compression effect, PMC boundary is placed at a half cell away from the two non-radiation edges to block the leakage from the non-radiating slots. Therefore, it is the patch antenna cavity in Fig. 1 (b) that is discussed in the following paragraphs. In practice, one may suppress the leakage by loading ferrite strips or placing multiple identical patches close to each other, side by side, to take advantage of the anti-phase property of the slots on both sides. To test the transient behavior of the antenna, it was first switched into the cavity mode to accumulate the input energy for about 253.6 ns. It is then switched to the radiating mode to radiate a single cycle of RF pulse (monopulse) that lasts for 0.418 ns. The PRP is 254 ns, which corresponds to a data rate of around 8 Mbits/s. Figure 5 shows the voltage waveform at the radiation edge of the patch for three pulses. It can be seen that the voltage waveform at the radiation edge appears to be smoothly regulated monocycle pulses. In order to calculate the pulse compression gain, one needs to compute the total radiated power carried by the pulse P_{rad}. This is done by integrating the radiated power at the far field in all directions. In addition to radiation, the energy lost per switching is included in the total energy flowing out of the radiation aperture during the pulse-on period with the average power of P_{av_a}. The radiation-to-loss ratio ξ can thus be evaluated as the ratio between these two. For this particular example, P_{rad}=0.738 W and P_{av_a}=4.6 W are obtained from FDTD simulations, which gives ξ=16%. In contrast, the maximum radiated power of the traditional microstrip patch antenna fed with the same single tone RF source is 0.078 W. Therefore, the maximum pulse compression gain is 9.75 dB. An alternative way in estimating the pulse compression gain is to first estimate the values of components in the equivalent transmission line model in Fig. 2, from the antenna dimensions then use (8) to evaluate the maximum pulse compression gain. For this particular example, the estimated component values are $Z_0 = 7.174\Omega$, $R_r = 615\Omega$ and $R_{on} = 0.01\Omega$. Therefore, the maximum pulse compression gain estimated by (8) is 9.15 dB, which agrees well with FDTD simulation results.

Figure 6 shows the time domain waveform of the radiated electric field at the broadside of the microstrip antenna. The distance of the observation point is r=100λ_0, where λ_0 is the free space wavelength of the RF carrier. It can be seen that the pulses appear accordingly in the far field when the switches are turned off and on periodically.

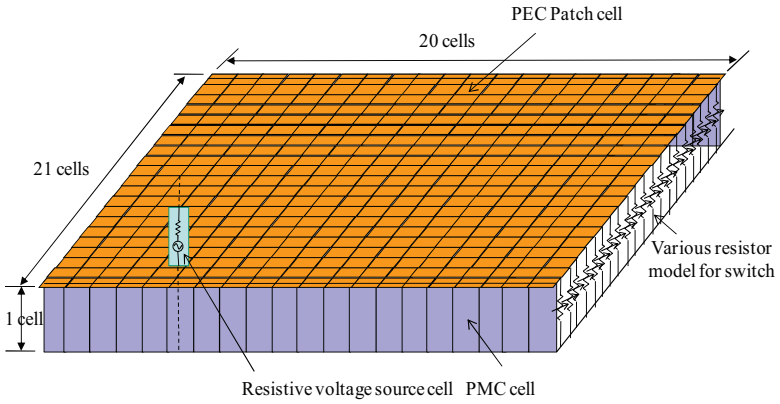

Fig. 4. FDTD simulation setup of the switched patch antenna.

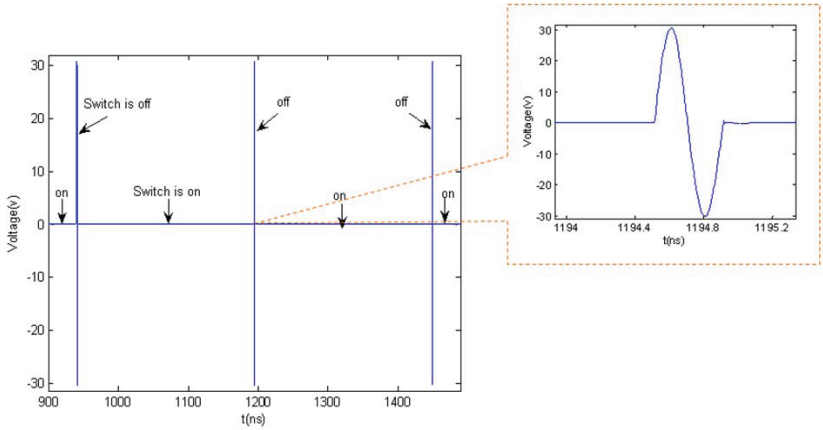

Fig. 5. Voltage waveform at the radiation edge of the switched patch antenna.

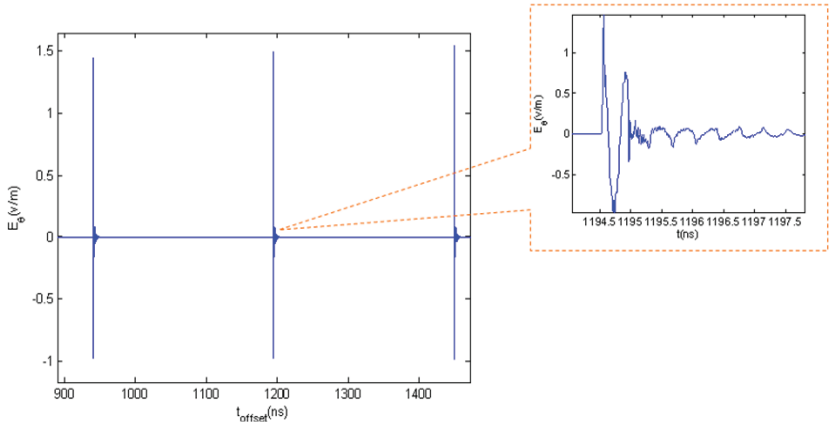

Fig. 6. Electric field waveform in far field at the broadside direction at the distance $r=100\lambda_0$.

As the waveform of a UWB signal radiated from an aperture antenna is dominated by the time derivative of the aperture field or magnetic current density in theory [26], the zoomed-in picture in Fig. 6 indeed shows a pulse waveform with discontinuities at the two edges, that is the time derivative of the monocylce aperture voltage. There is residue spurious radiation following the radiated pulse waveform even after the radiation is turned off. The spurious radiation is observed to be at much lower frequencies, which may be caused by releasing of the energy stored in the near field outside the antenna cavity after the switches short circuit the radiation slot. After

applying a time gate to remove the spurious noise, the frequency spectrum of the radiated electric field is shown in Fig. 7. The spectrum has a center frequency at around 2.77 GHz and a 3 dB bandwidth of 1.97 GHz, corresponding to a fractional bandwidth of 71%. It should be noted that the center frequency of 2.77 GHz in the radiation spectrum is shifted up from the original carrier frequency of 2.414 GHz. This is because the derivative effect in the radiated field adds an jw slope in the frequency response and emphasizes more in the higher frequency components. The center frequency returns to 2.414 GHz if the jw slope is de-embedded from Fig. 7. Given in Fig. 8 are the radiation patterns at the center frequency, the lower frequency and the upper frequency across the 3 dB bandwidth of the spectrum. Overall, the radiation patterns for the three examined frequencies are consistent in their shapes. The E-plane radiation patterns are almost identical for these three frequencies , though they are not perfectly symmetrical as only one radiation slot exists in the proposed microstrip patch antenna. This asymmetry causes the maximum radiation direction to shift away from the broadside to approximately the angle of $\theta = 20^{o}$. On the other hand, H-plane radiation patterns are perfectly symmetrical, while the patterns for higher frequencies show slightly narrower beamwidths due to the slightly higher antenna gains out of the same antenna aperture at higher frequencies.

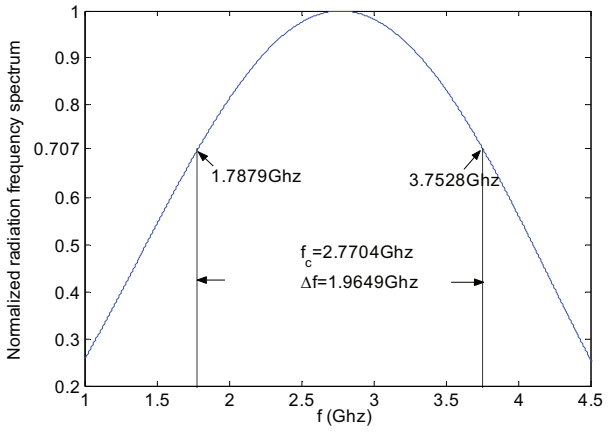

Fig. 7. Spectrum of the radiated monocycle pulse.

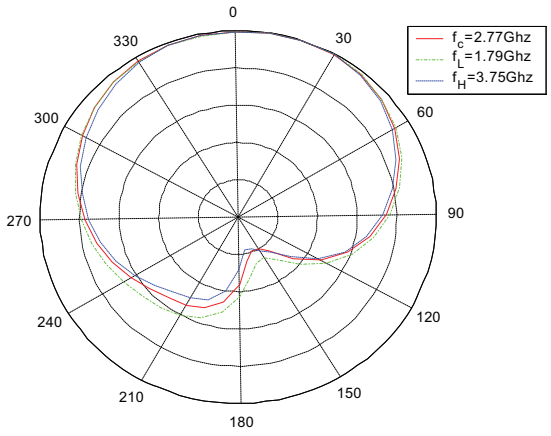

(a) E-plane

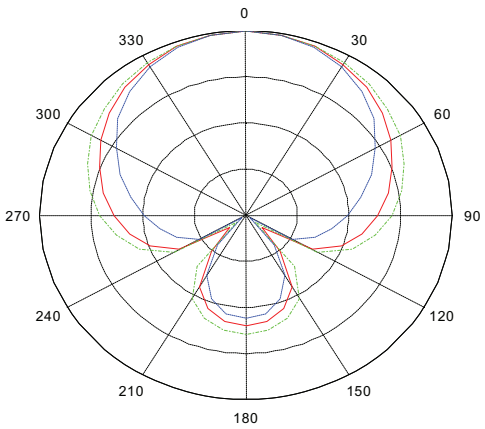

(b) H-plane

Fig. 8. Radiation patterns of 3 frequency components of the pulse in: (a) E-plane and (b) H-plane.

In DAM, one may operate the switched patch antenna toward higher radiation efficiency instead of higher pulse compression gain by using shorter charging time between the radiations. In order to examine the efficiency performance of the proposed scheme at different data rates, monopulses with different PRPs are used for communications that correspond to data rates up to 800 Mb/s. A comparison is carried out among three cases, as shown in Fig. 9. In the first case shown by the solid line, the radiation efficiency is strictly calculated from FDTD simulations by taking the ratio between the radiated energy and the injected energy. In the second case represented by the dotted line, the quality factors of the antenna resonator at both storage mode and

radiation mode and the radiation-to-loss ratio are obtained from the FDTD simulations. Those parameters are then substituted into (13) to predict the radiation efficiency. For the microstrip patch example shown in Fig. 1 (b), FDTD simulations show that $Q_{on} = 1256$, $Q_{off} = 167$ and $\xi = 16\%$. The FDTD prediction once again agrees well with the estimation given by (13). The third case is for a conventional microstrip patch antenna with the same physical dimensions as the DAM scheme, except the switches and the short-circuit is on the other radiating edge. A PMC boundary is also used to cover the non-radiating edges in this case. The efficiency is plotted in the dashed-dotted line. The radiation Q of the regular microstrip patch antenna obtained from FDTD simulations is around 200 at the resonant frequency of 2.4 GHz. For a conventional patch antenna, the radiation efficiency is almost 100% at the data rate of 12 Mb/s, as the modulation is within the antenna bandwidth. However, it is clear that the efficiency bandwidth product of this antenna is subject to the 1/Q limit, as the radiation efficiency drops quickly with the increase of the data rate. In contrast, the radiation efficiency of the proposed switched patch antenna scheme increases when the data rate increases and eventually saturates at the radiation-to-loss ratio of the radiation aperture $\xi = 16\%$. It is evident that the proposed switched patch antenna scheme can achieve 2-8 times higher radiation efficiency than the regular microstrip patch for data rates of 200 Mb/s and higher.

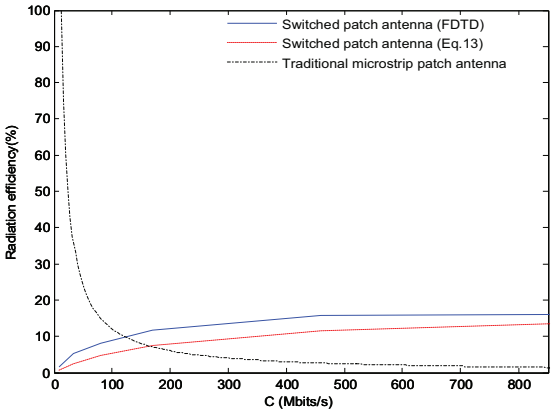

Fig. 9. Comparison of the radiation efficiency versus data rate between the DAM scheme and the conventional microstrip patch antenna.

VII. CONCLUSIONS

The theoretical performance of DAM technique is analyzed in this paper based on a switched patch antenna example. A thorough study on the time-varying behavior and nonlinear dynamics of this type of antennas has been carried out. The theoretical potential of the proposed antenna in terms of its radiation power and efficiency bandwidth relations have been derived by using both transmission line models and FDTD simulations. Both analyses and simulations demonstrated that the DAM scheme can obtain radiation efficiency bandwidth product over the conventional 1/Q limit, as long as pulses with integer number of RF cycles are transmitted as the information carrier and zero voltage switching is applied on the antenna.

Appendix I

For a resonator with a fixed intrinsic quality factor, one may prove that the electromagnetic energy stored in a resonator is maximized when the source impedance R_S is equal to the input impedance R_{in} of the resonator as follows. At the resonance, the intrinsic quality factor of the cavity according to the definition is given by:

$$Q = \omega_r \frac{2W_m}{P_{loss}} \quad \text{or} \quad Q = \omega_r \frac{2W_e}{P_{loss}}, \tag{A1}$$

where ω_r is the angular resonant frequency of the cavity, W_m, W_e are the average stored magnetic and electric energy which are equal to each other at resonance and P_{loss} is the dissipated power governed by:

$$P_{loss} = \frac{1}{2} V_S^2 \frac{R_{in}}{(R_S + R_{in})^2}. \tag{A2}$$

Substituting (A2) into (A1), the average stored magnetic/electric energy is given by:

$$W_m = W_e = \frac{Q}{4\omega_r} V_S^2 \frac{R_{in}}{(R_S + R_{in})^2}. \tag{A3}$$

To maximize the average stored magnetic/electric energy at resonance, the derivative of (A3) with respect to R_{in} must be zero, e.g.:

$$\frac{\partial W_m}{\partial R_{in}} = \frac{\partial W_e}{\partial R_{in}} = 0. \tag{A4}$$

By solving (A4), one yields:

$$R_{in} = R_S. \tag{A5}$$

The instantaneously radiated power from the antenna during the "pulse-on" period can be approximately obtained through the following transmission line analysis. To maximize the electromagnetic energy stored, the input impedance at the feeding position R_{in} should match to the source impedance R_S. Therefore, the feeding position L_1 needs to be adjusted to realize this matching. From the transmission line theory, the input admittance at the feeding point is given by:

$$G_{in} = Y_0 \frac{Y_{on} + jY_0 \tan(\beta L_1)}{Y_0 + jY_{on} \tan(\beta L_1)} + \frac{Y_0}{j \tan(\beta(L - L_1))}, \quad \text{(A6)}$$

where Y_{on} is the switch-on admittance and Y_0 is the transmission line characteristic admittance of the patch. Substituting the resonance condition $\beta L = \pi$ and the condition $Y_{on} >> Y_0$ into (A6), G_{in} is reduced approximately to:

$$G_{in} \approx \frac{1}{\sin^2(\beta L_1)} \frac{Y_0^2}{Y_{on}}. \quad \text{(A7)}$$

Substituting the matching condition $R_{in} = R_s$ yields:

$$\sin(\beta L_1) = \frac{\sqrt{R_s R_{on}}}{Z_0}, \quad \text{(A8)}$$

which determines the feeding position. When the switches are on, the voltage distribution along the equivalent transmission line of the patch follows a sinusoid function, which means that the voltage reaches maximum V_m in the middle of the line and is approximately zero at both ends. Therefore, the input voltage at the feeding point V_i is given by:

$$V_i = V_m \sin(\beta L_1). \quad \text{(A9)}$$

As any standing wave in resonators can be decomposed into two traveling waves that propagate toward opposite directions, the maximum voltage of the standing wave along the line should be equal to the summation of the amplitudes of both forward and backward propagating waves. This gives the amplitude of the traveling waves:

$$V_m^+ = V_m^- = \frac{1}{2} V_m = \frac{1}{2} \frac{V_i}{\sin(\beta L_1)}. \quad \text{(A10)}$$

The amplitude of incident wave V_{edge}^+ at the edge of the switches is equal to V_m^+ from the definition of traveling waves:

$$V_{edge}^+ = V_m^+ = \frac{1}{2} \frac{V_i}{\sin(\beta L_1)}. \quad \text{(A11)}$$

The reflected wave should be approximately equal to the incident wave in amplitude but with the opposite sign, so that the total edge voltage is approximately zero because of the low switch resistance condition at the edge. After the cavity is fully charged, the switches are turned off. The boundary condition at the switch edge suddenly changes from low impedance to high impedance. An enhanced aperture field should appear on this edge right after the switching moment. The voltage at the edge is thus given by:

$$V_{edge} = V_{edge}^+ + V_{edge}^- = V_{edge}^+ (1 + \Gamma), \quad \text{(A12)}$$

where Γ is the reflection coefficient at the edge, which is determined by the aperture radiation impedance. The reflection coefficient is given by:

$$\Gamma = \frac{\frac{1}{G_r + jB_r} - Z_0}{\frac{1}{G_r + jB_r} + Z_0}, \quad \text{(A13)}$$

thus,

$$V_{edge} = V_{edge}^+ \left[\frac{2}{1 + Z_0 (G_r + jB_r)} \right]. \quad \text{(A14)}$$

The radiation resistance $R_r = 1/G_r$ is usually much greater than the characteristic impedance Z_0 for practical microstrip antennas. Therefore, the instantaneous voltage at the edge is somehow "amplified." The instantaneous power radiated is given by:

$$P_{rad} = \frac{1}{2} |V_{edge}|^2 G_r. \quad \text{(A15)}$$

Substituting (A10) and (A14) into (A15) yields:

$$P_{rad} = \frac{1}{2} \frac{V_i^2}{R_s} \frac{Z_0^2 G_r}{R_{on}} \frac{1}{(1 + Z_0 G_r)^2 + (Z_0 B_r)^2}. \quad \text{(A16)}$$

As for an ideal regular patch antenna excited with a single-tone carrier supply in the same amplitude, the maximum radiated power is equal to the injected power $P_{rad} = \frac{1}{2} \frac{V_i^2}{R_s}$. Under the assumption of $G_r Z_0 << 1$ and $B_r << Y_0$, the maximum pulse compression gain is thus derived to be:

$$G_{pulse,\max} = \frac{Z_0^2}{R_{on} R_r}. \quad \text{(A17)}$$

Appendix II

The equivalent circuits of the antenna in both charging and discharging states are depicted in Fig. A1.

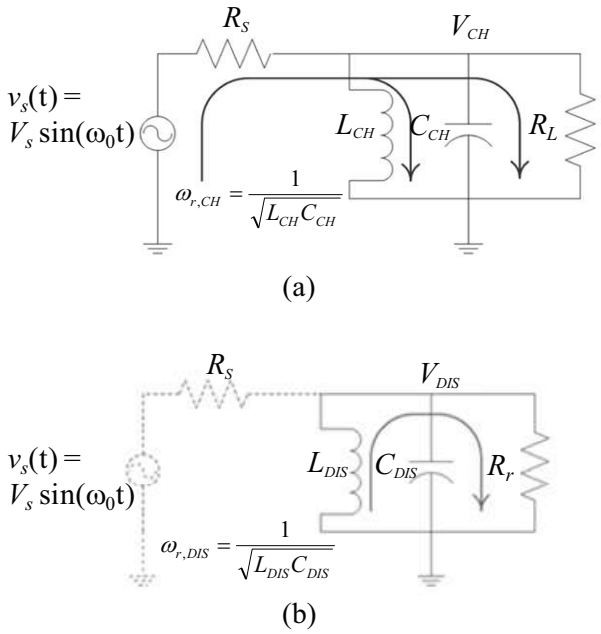

Fig. A1. (a) Charging and (b) discharging mode equivalent circuit models of the switched patch antenna.

Figure A1 (a) represents the charging behavior of the antenna, where R_S is the source resistance and R_L is the transformed load resistance from the switch-on resistance of the RF switches; L_{CH} and C_{CH} are the equivalent inductance and capacitance of the switched patch antenna resonator during the charging mode. The patch antenna resonator is charged according to the time constant $\tau_{CH} = (R_S // R_L)C_{CH}$. Once the switches are turned off, the source is removed and the antenna starts to discharge due to the radiation, as represented by Fig. A1 (b). Assuming that the switch-off resistance is much greater than the radiation resistance of the antenna, the discharging time constant is governed by $\tau_{DIS} = R_r C_{DIS}$, where R_r is the radiation resistance of the radiation slot and C_{DIS} is the equivalent capacitance of the switched patch antenna resonator in the discharging mode. If the switched patch antenna resonator is excited at the resonance during the charging mode, with the resonant frequency $\omega_0 = \omega_{r,CH}$, the voltage change during the charging time Δt_{CH} and the discharging time Δt_{DIS} can be written as the follows [20]:

$$\Delta V_{CH} = (V_{DIS}(t_1) - V_{CH,Steady})(-\Delta t_{CH} / 2\tau_{CH}), \quad \text{(A18 (a))}$$

$$\Delta V_{DIS} = (V_{CH}(t_0) - V_{DIS,Steady})(-\Delta t_{DIS} / 2\tau_{DIS}), \quad \text{(A18 (b))}$$

where $V_{CH,Steady}$ and $V_{DIS,Steady}$ stand for the steady state voltages of the antenna resonator after the infinite amount of charging and discharging time, in which $V_{CH,Steady} = V_S / (R_S / R_L + 1)$ and $V_{DIS,Steady} = 0$. $V_{DIS}(t_1)$ is the initial condition of the resonator at the switching moment when discharging ends and charging begins. $V_{CH}(t_0)$ is the initial condition of the resonator in the discharging mode, which is the voltage when charging ends and discharging starts. With the switching process repeating for a certain period of time, the voltage changes during the charging and discharging modes and must settle to be equal, due to the equilibrium,

$$\Delta V_{CH} = \Delta V_{DIS}. \quad \text{(A19)}$$

Under the assumption that the switching speed is much faster than the resonator bandwidth, the initial voltages of $V_{DIS}(t_1)$ and $V_{CH}(t_0)$ can be approximated by the settling voltage V_X:

$$V_X \approx V_{CH}(t_0) \approx V_{DIS}(t_1). \quad \text{(A-20)}$$

Substituting Eqs. (A18) and (A20) into Eq. (A19):

$$(V_{CH,Steady} - V_X)\frac{\Delta t_{CH}}{\tau_{CH}} = V_X \frac{\Delta t_{DIS}}{\tau_{DIS}}. \quad \text{(A21)}$$

Thus, the settling voltage ratio $\eta_{Settling}$, defined as the ratio between the settling voltage and the steady voltage $V_{CH,Steady}$ is given by:

$$\eta_{Settling} = \frac{V_X}{V_{CH,Steady}} = \frac{1}{1 + \frac{\Delta t_{DIS}}{\Delta t_{CH}} \frac{\tau_{CH}}{\tau_{DIS}}}. \quad \text{(A22)}$$

The charging and discharging time constants can also be expressed in terms of the intrinsic quality factors of the patch antenna resonator, respectively, in the charging and discharging modes Q_{on} and Q_{off}. The charging time constant is:

$$\tau_{CH} = Q_{on} / (R_L / R_S + 1)\omega_{r,CH}), \quad \text{(A23)}$$

where $\omega_{r,DIS} = \omega_{r,CH} / 2$ because of the change of the resonant frequency from the l/2 mode to the l/4 mode. The discharging time constant is then governed by:

$$\tau_{DIS} = Q_{off}\xi/(\omega_{r,DIS}), \quad \text{(A24)}$$

as the radiation-to-loss ratio ξ is defined as the ratio of the total radiated energy from the per RF cycle to the total energy loss per RF cycle, including both the radiation and the loss, due to the switching action itself. Substituting the relations $\Delta t_{DIS} = T_{r,pulse}$ and $\Delta t_{CH} = PRP - T_{r,pulse}$; Eqs. (A23) and (A24) into (A22) yields:

$$\eta_{Settling} = \frac{1}{1 + \frac{1}{PRP/T_{r,pulse} - 1}\frac{Q_{on}/(R_L/R_S + 1)}{2Q_{off}\xi}}, \quad \text{(A25)}$$

or,

$$\eta_{Settling} = \frac{1}{1 + \frac{1}{2/(CT_{r,pulse}) - 1}\frac{Q_{on}/(R_L/R_S + 1)}{2Q_{off}\xi}}, \quad \text{(A26)}$$

where C is the data rate of the system which is related to PRP by:

$$C = \frac{2}{PRP} \quad (bits/s). \quad \text{(A27)}$$

(A26) shows that a higher settling operating point results from a lower data rate or smaller duty cycle of the radiated pulses, for a given patch antenna design and matching condition. On the other hand, the voltage envelop across the resonant LC tank resulting from the initial charging process is:

$$V_{CH}(t) = V_S/(R_S/R_L + 1)(1 - e^{-t/2\tau_{CH}}). \quad \text{(A28)}$$

The voltage finally settling across the LC tank in the charging mode is thus:

$$V_{CH}(\eta_{Settling}) = V_S/(R_S/R_L + 1)\eta_{Settling}. \quad \text{(A29)}$$

From KCL circuit theory, the total settling current flowing into the LC tank in charging mode is given by:

$$I_{CH}(\eta_{Settling}) = V_S(1 - \frac{\eta_{Settling}}{R_S/R_L + 1})/R_S. \quad \text{(A30)}$$

The time-average input power into the LC tank in the charging mode is:

$$P_{CH}(\eta_{Settling}) = \frac{V_S^2}{2}\frac{\eta_{Settling}}{R_S/R_L + 1}(1 - \frac{\eta_{Settling}}{R_S/R_L + 1})/R_S. \quad \text{(A31)}$$

The time-average dissipated power on the equivalent resistance R_L is:

$$P_d(\eta_{Settling}) = \frac{V_S^2}{2}(\frac{\eta_{Settling}}{R_S/R_L + 1})^2/R_L. \quad \text{(A32)}$$

When the resonator is settling at the highest point ($\eta_{Settling} = 1$),

$$P_{CH}(\eta_{Settling}=1) = P_d(\eta_{Settling}=1) = \frac{V_S^2}{2}(\frac{1}{R_S/R_L + 1})^2/R_L, \quad \text{(A33)}$$

the input power is completely dissipated on the switches, while the stored energy in the LC tank reaches its maximum. This is the condition for the maximum pulse compression gain. However, to achieve higher radiation efficiency requires $\eta_{Settling} < 1$, whereas the pulse compression gain drops accordingly,

$$G_{pulse}(\eta_{Settling}) = \eta_{Settling}^2 G_{pulse,\max}. \quad \text{(A34)}$$

Based on the definition of the pulse compression gain, the average radiated power from the radiation pulse is given by:

$$P_{r,pulse}(\eta_{Settling}) = G_{pulse}(\eta_{Settling})P_{r,patch}. \quad \text{(A35)}$$

A conventional resonant patch antenna has the same equivalent circuit model as that in Fig. A1 (a), where R_L is the transformation of the radiation impedance of the antenna if other types of loss are ignored. With the same resistive voltage source as the switched patch antenna, the maximum radiated power of the traditional patch antenna $P_{r,patch}$ will be equal to the maximum dissipated power on the switches of the antenna resonator during the switch-on period, e.g.:

$$P_{r,patch} = P_d(\eta_{Settling} = 1). \quad \text{(A36)}$$

Substituting Eqs. (A34) and (A36) into (A35), the time-average radiated power for the pulse is obtained,

$$P_{r,pulse}(\eta_{Settling}) = P_d(\eta_{Settling} = 1)G_{pulse,\max}\eta_{Settling}^2. \quad \text{(A37)}$$

Thus, the total radiated energy is:

$$E_{r,pulse}(\eta_{Settling}) = P_{r,pulse}(\eta_{Settling})\Delta t_{DIS}. \quad \text{(A38)}$$

It is assumed that the radiation takes a small portion of the total stored energy away from the antenna resonator, due to the short radiation period. Due to energy conservation, the total input energy into the antenna resonator during the recharging period is to recuperate the amount of stored energy that was lost in the previous discharging state, which is denoted by E_{rc} and to compensate the dissipated energy on the switches E_d during the recharging period at the same time. By recalling the definition of the radiation efficiency of the switched patch antenna, we have:

$$Eff_r(\eta_{Settling}) = \frac{E_{r,pulse}(\eta_{Settling})}{E_{rc}(\eta_{Settling}) + E_d(\eta_{Settling})}. \quad \text{(A39)}$$

The recuperated energy E_{rc} is equal to the total stored energy loss during the radiation period $T_{r,pulse}$, caused by both the radiation from the radiation edge and the switching action itself. Therefore,

$$E_{rc}(\eta_{Settling}) = E_{r,pulse}(\eta_{Settling})/\xi . \quad \text{(A40)}$$

The dissipated energy on the switches during the recharging period is given by:

$$E_d(\eta_{Settling}) = P_d(\eta_{Settling}=1)\eta_{Settling}^2 \Delta t_{CH} , \quad \text{(A41)}$$

where,

$$\Delta t_{CH} = \frac{E_{rc}(\eta_{settling})}{P_{CH}(\eta_{settling}) - P_d(\eta_{settling})} . \quad \text{(A42)}$$

After substituting Eqs. (A38), (A40), (A26) and (A39) into (13) and some additional mathematical manipulations, the radiation efficiency of the pulse transmission scheme based on the switched resonant patch antenna in Fig. 1 is finally obtained,

$$Eff_r = \frac{\xi}{1+(\frac{2}{CT_{r,pulse}}-1)\frac{2Q_{off}\xi}{Q_{on}}} . \quad \text{(A43)}$$

REFERENCES

[1] H. G. Schantz, "Introduction to ultra-wideband antenna," *IEEE UWBST 2003 Conference Proceedings*, pp. 1-9, November 2003.

[2] H. G. Schantz, "A brief history of ultra-wideband antennas," *IEEE UWBST 2003 Conference Proceedings*, pp. 209-213, November 2003.

[3] K. Y. Yazdandoost and R. Kohno, "Ultra-wideband antenna," *IEEE Communications Magazine*, vol. 42, pp. 29-32, June 2004.

[4] J. T. Merenda, "Synthesizer radiating systems and methods," *U.S. Patent No. 5,402,133*, March 28, 1995.

[5] V. F. Fusco and Q. Chen, "Direct-signal modulation using a silicon microstrip patch antenna," *IEEE Trans. on Antenna and Propagation*, vol. 47, pp. 1025-1028, June 1999.

[6] W. Yao and Y. Wang, "Radiating beyond the bandwidth using direct antenna modulation," *Antennas and Propagation Society International Symposium, IEEE*, vol. 1, pp. 20-25, June 2004.

[7] W. Yao and Y. Wang, "Direct antenna modulation-a promise for ultra-wideband (UWB) transmitting," *Microwave Symposium Digest, IEEE MTT-S International*, vol. 2, pp. 1273-1276, June 2004.

[8] S. D. Keller, W. D. Palmer, and W. T. Joines, "Direct antenna modulation: analysis, design, and experiment," *IEEE Antennas and Propagation Society International Symposium 2006*, pp. 909-912, July 9-14, 2006.

[9] S. D. Keller, W. D. Palmer, and W. T. Joines, "Digitally driven antenna for HF transmission," *IEEE Trans.* on *Microwave Theory and Techniques*, vol. 58, no. 9, pp. 2362-2367, September 2010.

[10] H. G. Schantzchantz, "Nanoantennas: a concept for efficient electrically small UWB devices," *2005 IEEE International Conference on Ultra-Wideband*, pp. 264-268, September 5-8, 2005.

[11] J. Wang, "Characteristics of a new class of diode-switched integrated antenna phase shifter," *IEEE Trans. Antennas and Propagation*, vol. 31, pp. 156-159, January 1983.

[12] F. Yang and Y. Rahmat-Samii, "A reconfigurable patch antenna using switchable slots for circular polarization diversity," *IEEE Microwave and Wireless Components Letters*, vol. 12, no. 3, pp. 96-98, March 2002.

[13] G. H. Huff, J. Feng, S. Zhang, and J. T. Bernhard, "A novel radiation pattern and frequency reconfigurable single turn square spiral microstrip antenna," *IEEE Microwave and Wireless Components Letters*, vol. 13, pp. 57-59, February 2003.

[14] A. E. Fathy, A. Rosen, H. S. Owen, F. McGinty, D. J. McGee, G. C. Taylor, R. Amantea, P. K. Swain, S. M. Perlow, and M. ElSherbiny, "Silicon-based reconfigurable antennas-concepts, analysis, implementation, and feasibility," *IEEE Trans. Microwave Theory and Techniques*, vol. 51, pp. 1650-1661, June 2003.

[15] J. T. Aberle, S. H. Oh, D. T. Auckland, and S. D. Rogers, "Reconfigurable antennas for wireless devices," *IEEE Trans. Antennas and Propagation Magazine*, vol. 45, pp. 148-154, December 2003.

[16] V. P. Prokhorenko, V. E. Ivashchuk, and S. V. Korsun, "Electromagnetic impulse radiator," *Ultrawideband and Ultrashort Impulse Signals*, Sevastopol, Ukraine, pp. 243-245, September 19-22, 2004.

[17] V. P. Prokhorenko, V. E. Ivashchuk, and S. V. Korsun, "On radiation efficiency and radiating capability of impulse antennas," *Ultrawideband and Ultrashort Impulse Signals*, Sevastopol, Ukraine, pp. 251-253, September 19-22, 2004.

[18] V. P. Prokhorenko, V. E. Ivashchuk, and S. V. Korsun, "Improvement of electromagnetic pulse radiation efficiency," *Subsurface Sensing Technologies and Applications*, vol. 6, pp. 107-123, April 2005.

[19] X. Xu, H. C. Jing, and Y. E. Wang, "High speed pulse radiation from switched electrically small antenna," 2006 IEEE *AP-S International Symposium and USNC/URSI National Radio*

Science Meeting, Albuquerque, New Mexico, July 2006.

[20] R. Harrington, "Effects of antenna size on gain, bandwidth, and efficiency," *Journal of Research of National Bureau of Standards*, v 64-D, pp. 1-12, 1960.

[21] S. Kim and Y. E. Wang, "Theory of switched RF resonators," *IEEE Trans. Circuits and Systems*, vol. 53, pp. 2521-2527, December 2006.

[22] H. Liu, "Error performance of a pulse amplitude and position modulated ultra-wideband system over lognormal fading channels," *IEEE Comm. Letters*, vol. 7, no. 11, pp. 531-533, November 2003.

[23] C. A. Balanis, "Antenna theory: analysis and design," Third Edition, *John Wiley & Sons, Inc*, 2005.

[24] F. Raab, "Idealized operation of the class e tuned power amplifier," Circuits and Systems, *IEEE Trans. Circuits and Systems*, vol. 24, no. 12, pp. 725-735, December 1977.

[25] A. Taflove and S. C. Hagness, "Computational electrodynamics: the finite-difference time-domain method," Second Edition, *Artech House*, 2000.

[26] C. E. Baum, "Radiation of impulse-like transient fields," *Sensor and Simulation Notes 321 USAF Phillips Lab*, Albuquerque, NM, November 1989.

A Reconfigurable Square Slot Antenna with Switchable Single Band, UWB and UWB with Band Notch Function Performances

B. Badamchi [1], A. Valizade [2], P. Rezaei [1] and Z. Badamchi [3]

[1] Department of Electrical Engineering
Semnan University, Semnan, Iran
b.badamchi@urmia.ac.ir, prezaei@semnan.ac.ir

[2] Young Researchers Club
Islamic Azad University, Qaemshahr Branch, Qaemshahr, Iran
a.valizade@sun.semnan.ac.ir

[3] Department of Electrical Engineering
Islamic Azad University, Sciences and Researches Branch, Urmia, Iran
zahra.badamchi@yahoo.com

Abstract ─ In this paper a novel method for designing a square slot antenna with switchable single band, multi-resonance (Ultra-Wideband (UWB)) and UWB with band-notch function performances has been presented. By inserting a pair of symmetrical notches on the feed-line and a pair of gamma-shaped slots on the radiating stub, additional resonances are excited and hence much wider impedance bandwidth is produced; especially at the higher band. In order to generate a reconfigurable band-notch function, a PIN diode is utilized across the microstrip stub between the two gamma-shaped slots. Also, through implementation of two H-shaped slots on the ground plane, not only the coupling at lower and middle frequencies is adjusted, but also by embedding a PIN diode between these two H-shaped slots, an additional reconfigurable functionality is added to the antenna performances; which can switch between a single band and multi-resonance (UWB) characteristics. The designed antenna has a small size of 20×20 mm^2 while simulated and experimental results obtained for this antenna reveal that it exhibits good radiation behavior for its various switchable operation frequencies.

Index Terms ─ Band-notch function, microstrip-fed slot antenna, reconfigurable structure, ultra-wideband applications and single band performance.

I. INTRODUCTION

In UWB communication systems, which due to FCC's frequency band allocation spread from 3.1 GHz to 10.6 GHz, one of key issues is the design of compact antennas which provide wideband characteristic over the entire operating band [1]. Consequently, a number of printed microstrip slot and monopole antennas with different geometries have been experimentally characterized and automatic design methods have been developed to achieve the optimum planar shape [1]-[4].

On the other hand, the wide frequency range for UWB systems will cause interference to the existing wireless communication systems, such as the Wireless Local Area Network (WLAN) for IEEE 802.11a operating in 5.15-5.35 GHz and 5.725-5.825 GHz bands; therefore, the UWB antenna with a band-stop performance is required [2]. To overcome this problem, several novel planar antennas with band-notch characteristic have been presented recently. The most common and easiest technique is embedding a narrow slot into the radiating patch of the antenna and change the current flow directions on its metallic parts, as demonstrated in [2], [5]-[7]. All the techniques in

Submitted On: February 28, 2013
Accepted On: April 24, 2014

these references are used for rejecting a fixed band of frequencies. Another method to avoid this frequency band interference is the use of a reconfigurable structure. In order to effectively and fully utilize the UWB spectrum and to improve the performance of the UWB system, it is desirable to design the UWB antenna with reconfigurable band-notch [8]-[10]. It will help to minimize the interference between the systems and whenever there is no coexistence system and the structure of the antenna can be transformed in a way that leads to a whole coverage of UWB spectrum. In [8] and [9] in order to have selectivity on the rejection of a specific band which is between 5 GHz to 6 GHz, diodes are utilized while in [10], RF MEMS are used for the same reason.

Furthermore, future radio systems such as software defined radio and cognitive radio concepts, give rise to significant challenges for antenna design with switchable or adjustable frequency response [11]. Recently, a number of antennas with reconfigurable structures have been presented, in which wideband and narrowband functionalities are combined [12]-[13]. A Vivaldi antenna with switchable performances between a wideband mode and three narrowband modes has been presented in [12]. In [13], two reconfigurable monopole antennas by utilizing PIN diode or varactor diode have been presented, which are capable of combining wideband and narrowband functionalities.

A new compact reconfigurable microstrip-fed slot antenna with switchable single band, multi-resonance (UWB) and UWB with band-notch performances is presented and discussed in this paper. In the proposed structure, multi-resonance function is provided by etching two back to back gamma-shaped slots on the radiating stub, a pair of notches on the feed-line and a switchable band-notch characteristic is obtained by implementing a PIN diode on the microstrip line, which is placed between these two gamma-shaped slots. Also, by adding two H-shaped slots on the ground plane and embedding another PIN diode between these two H-shaped slots, electability between single band and multi-resonance performances is provided. Good return loss and radiation pattern characteristics are obtained in the frequency band of interest. Simulated and experimental results show that the proposed slot antenna could be a good candidate for UWB applications.

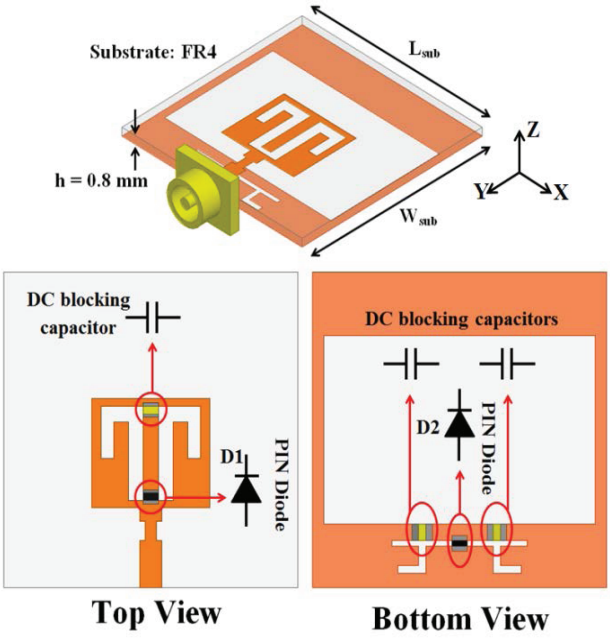

Fig. 1. Geometry of the proposed slot antenna.

II. ANTENNA DESIGN

The presented small reconfigurable slot antenna fed by a 50 Ω microstrip line is shown in Fig. 1, which is printed on a FR4 substrate of thickness of 0.8 mm, permittivity of 4.4 and loss tangent of 0.018. The basic slot antenna structure consists of a square radiating stub, a feed-line and a ground plane. The square stub is connected to a 50 Ω microstrip feed-line. On the other side of the substrate, a conducting ground plane is placed. The proposed antenna is connected to a 50 Ω SMA connector for signal transmission.

In this study, to design a novel antenna, two gamma-shaped slots with a PIN diode between their bottom sections and also two H-shaped slots with a PIN diode between them, have been added to the radiating stub and the ground plane, respectively. Moreover, two notches with variable dimensions have been also etched on the feed-line. Based on electromagnet coupling theory, these notches on the feed-line can adjust the electromagnetic coupling effects between the patch and the ground plane and improves the impedance matching in the antenna design without any cost of size or expenses, which play an important role in wideband characteristic of the antenna by adding an additional resonance to the frequency response [8].

As illustrated in Fig. 1, the gamma-shaped slots are symmetrically placed on the radiating stub, with respect to the longitudinal direction. These slots provide additional surface current paths which lead to an additional resonance and consequently wider impedance bandwidth can be produced, and as a result, the antenna frequency response covers the whole UWB bandwidth [2]. Moreover, in order to achieve a switchable band-notch function, a PIN diode is embedded on the radiating stub which role is changing the configuration of the slots on this stub. When the PIN diode (D1 in Fig. 1) is biased reversely or turned off, the gamma-shaped slots combine together and transform to a unique V-shaped like slot. The V-shaped like slot perturbs the resonant response of the antenna and acts as a half-wave resonant structure [13]. At the notched frequency, the current flows are more dominant around the V-shaped like slot and they are oppositely directed between the slot edges [8]. As a result, the desired high attenuation near the notched frequency can be produced.

The two H-shaped slots on the ground plane are modified in a way to improve the frequency response of the antenna by affecting the coupling at different switchable performances of the designed antenna. On the other hand, another reconfigurable functionality is added to the antenna performance by embedding a PIN diode between these two H-shaped slots. When the PIN diode is not biased forwardly, these two H-shaped slots unite and form a unique π-shaped slot. This transformation affects the entire characteristic of the antenna and changes it from a multi-resonance UWB antenna to a single band (narrow band) antenna, which can cover the WLAN frequency band (4-5 GHZ).

For avoiding DC short circuit in the PIN diodes biasing circuits, three 100 pF DC blocking capacitors were utilized, as shown in Fig. 1. The effect of the PIN diodes on the frequency response of the antenna has been considered at simulation studies, through simulating them as corresponding low capacitor and low resistance at their reverse and forward bias statuses, respectively. The antenna design parameters are shown in Fig. 2 and their final values are presented in Table 1.

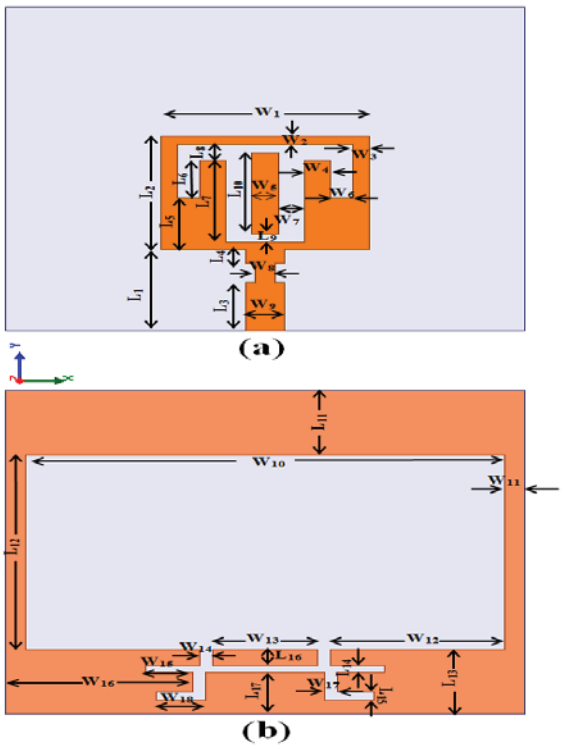

Fig. 2. The proposed antenna design parameters: (a) top view and (b) bottom view.

Table 1: The final dimensions of the designed antenna

Param.	mm	Param.	mm	Param.	mm
W_{sub}	20	W_{11}	0.75	L_6	2.3
L_{sub}	20	W_{12}	6.75	L_7	5
h	0.8	W_{13}	4	L_8	1
W_1	8	W_{14}	0.5	L_9	0.5
W_2	0.5	W_{15}	1.8	L_{10}	5
W_3	0.6	W_{16}	7.2	L_{11}	4
W_4	1	W_{17}	0.5	L_{12}	12
W_5	1	W_{18}	1.9	L_{13}	4
W_6	0.9	L_1	5	L_{14}	0.4
W_7	1	L_2	7	L_{15}	0.5
W_8	0.8	L_3	3	L_{16}	1
W_9	1.5	L_4	0.8	L_{17}	2.6
W_{10}	18.5	L_5	3.2		

III. RESULTS AND DISCUSSIONS

In this section, the proposed slot antenna with various design parameters was constructed and

the numerical and experimental results of the input impedance and the radiation characteristics are presented and discussed. The simulated results are obained using the Ansoft simulation software High Frequency Structure Simulator (HFSS) [14].

The configurations of various antenna structures which are compared to the proposed antenna structure in the simulation study, are shown in Fig. 3. Return loss characteristics for ordinary slot antenna (Fig. 3 (a)), slot antenna with gamma-shaped slots inside the radiating stub (Fig. 3 (b)) and the proposed slot antenna structure (Fig. 1) with different states of PIN diodes biasing, are compared in Fig. 4.

As shown in Fig. 4, it is observed that the upper frequency bandwidth is firstly affected by the presence of the gamma-shaped slots in the radiating stub and then it is affected by cutting two notches on the feed-line. It is found that by inserting the gamma-shaped slots in the radiating stub, the antenna can create an additional resonance at 9.25 GHz and also it is found that by inserting two notches with modified dimensions on the feed-line, the antenna is capable of exhibiting another additional resonance at frequency of 10.2 GHz. This is mainly due to the fact that the surface current path on the feed-line and the radiating stub is changed and determined by the notches on the feed-line and the gamma-shaped slots, respectively [8]. Moreover, as illustrated in Fig. 4, the gamma-shaped slots with a PIN diode (D1) between their bottom sections are used in order to electrically switch between the frequency band-notch performance and the new excitation function.

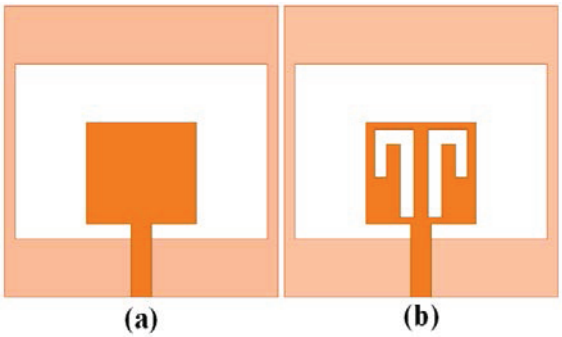

Fig. 3. (a) Basic structure (ordinary slot antenna) and (b) antenna with gamma-shaped slots on the radiating stub.

Another important result which is obtained from the simulation study, is that the notched frequency bandwidth is sensitive to the dimensions of the gamma-shaped slots [2]. To give a better insight about the band-notch behavior of the designed antenna, a smith chart demonstration of its input impedance at the band-notch performance is presented in Fig. 5.

Furthermore, it is shown in Fig. 4, that when the PIN diode between the H-shaped slots on the ground plane is off or biased reversely, the frequency response of the antenna has a fundamental change and the proposed structure turns from a wideband antenna into a single band antenna [13].

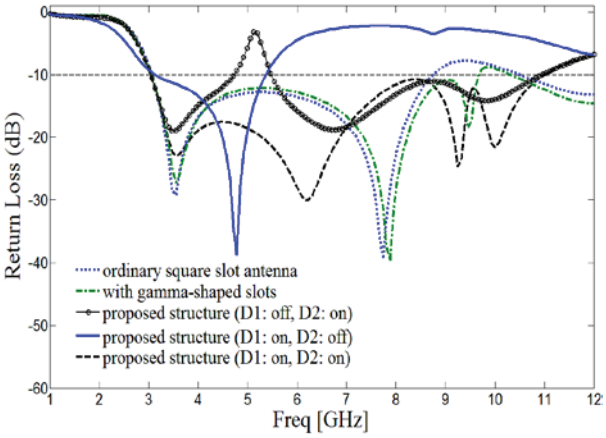

Fig. 4. Simulated return loss characteristics for antennas shown in Fig. 2 and the proposed antenna structure with various PIN diodes biasing statuses (Fig. 1).

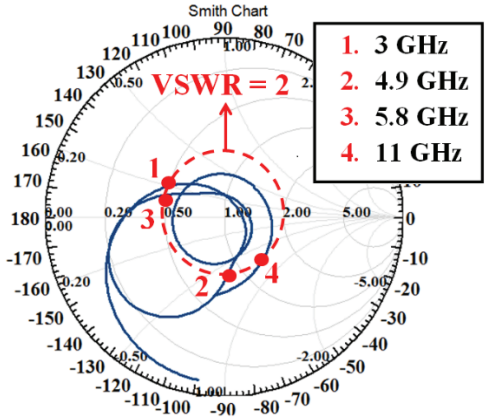

Fig. 5. Smith chart demonstration of band-notch performance of the proposed antenna.

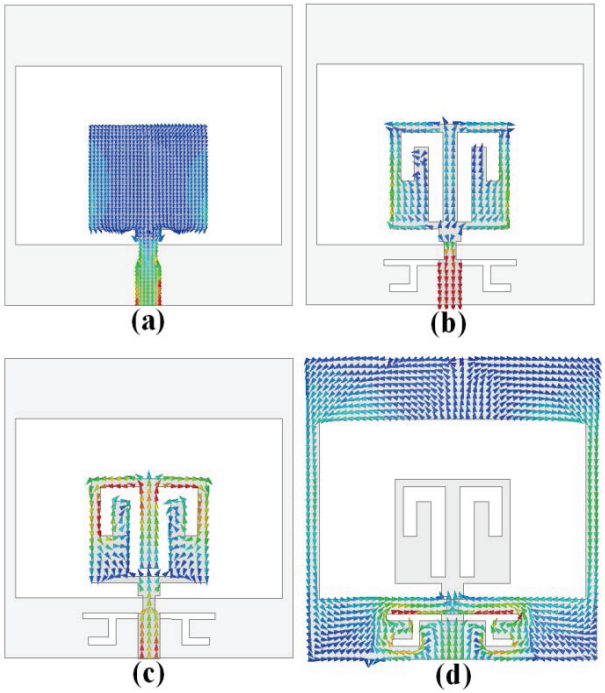

Fig. 6. Simulated surface current distributions: (a) on the radiating stub for ordinary square slot antenna with notches on the feed-line at additional resonance frequency (10.2 GHz), (b) on the radiating stub for the proposed antenna at additional resonance frequency (9.45 GHz), (c) on the radiating stub for the proposed antenna at central notched frequency (5.5 GHz) and (d) on the ground plane for the proposed antenna at single band performance central frequency (4.8 GHz).

The simulated current distribution on the ordinary square slot antenna with notches on the feed-line is shown in Fig. 6 (a). As it can be seen in this figure, the current distribution at 10.2 GHz (additional resonance frequency) is concentrated around the notches on the feed-line and therefore, the antenna impedance changes at this frequency due to the dimensions of the notches and leads to an additional resonance. Also, in order to understand the phenomenon behind switching electronically between multi-resonance (UWB), UWB with band-notch function and single band performances of the proposed antenna, the simulated surface current distributions on the radiating stub and the ground plane of the proposed antenna for on and off statuses of pin diodes, are presented in Figs. 6 (b), (c) and (d), respectively.

It can be observed in Fig. 6 (b) that when both PIN diodes are biased forwardly, at 9.45 GHz the current is concentrated near the interior and exterior edges of the gamma-shaped slots on the radiating stub. It is found that by using this structure, an additional resonance is generated at 9.45 GHz [2]. Figure 6 (c) presents the simulated current distributions on the radiating stub at the notched frequency (5.5 GHz) when the PIN diode on the radiating stub is off (D1: off) and the PIN diode on the ground plane is on (D2: on). As it can be observed in this figure, at the notched frequency the current flows are more dominant around the interior and exterior edges of the V-shaped like slot on the radiating stub and they are oppositely directed, and as a result, the desired high attenuation near the notched frequency can be produced [2].

Finally, the current distribution on the ground plane for the single band performance of the antenna at 4.8 GHz is shown in Fig. 6 (d). It is found that when the PIN Diode on the radiating stub is on (D1: on) and the PIN diode on the ground plane is off (D2: off), the current flows are concentrated and dominant around the π-shaped slot on the ground plane and this slot acts as a half wavelength resonator [8].

In order to obtain modified and final values for different design parameters of the presented antenna, a parametric study was also performed in which one parameter was changed at a time, while others were kept fixed. Figure 7 shows the effect of notches with various dimensions in the ground plane on return loss characteristic of the proposed antenna for the cases, which are listed in Table 2. As it can be seen in Fig. 7, the notches on the feed-line have an important role in wideband characteristic of the antenna.

Table 2: Three cases of proposed antenna with different values of notches on the feed-line

Case	L_3	L_4	W_8
1	3	0.8	0.8
2	2	0.8	0.4
3	1	2.25	0.8

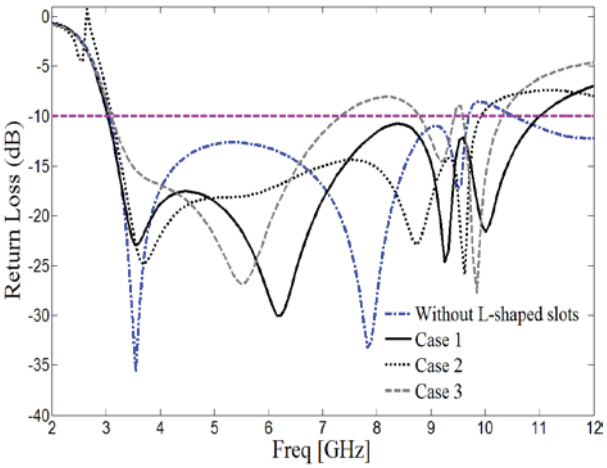

Fig. 7. The effect of a pair of notches in the feed-line on return loss for cases in Table 1.

The proposed antenna with final design parameters was built and tested. External DC wires were used in order to bias the PIN diodes. Figure 8 shows the fabricated antenna and its measured and simulated return loss characteristics are presented in Fig. 9. The measured results reveal that the fabricated antenna can satisfy the requirements for ultra-wide band performance and covers the frequency band of 2.7 GHz to over 10.65 GHz, with a band-notch function around 4.8-5.83 GHz, as it was predicted from the simulation studies. However, as shown in Fig. 9, there exists a discrepancy between the measured results and the simulated data. This discrepancy is mostly due to a number of parameters, such as the fabricated antenna dimensions accuracy as well as the thickness and dielectric constant of the substrate on which the antenna is fabricated, the wide range of simulation frequencies and also the effect of PIN diodes and their biasing circuits. In order to confirm the accuracy of return loss characteristics for the designed antenna, it is recommended that the manufacturing and measurement processes need to be performed more carefully; besides, SMA and other components solder accuracy and FR4 substrate quality needs to be taken into consideration.

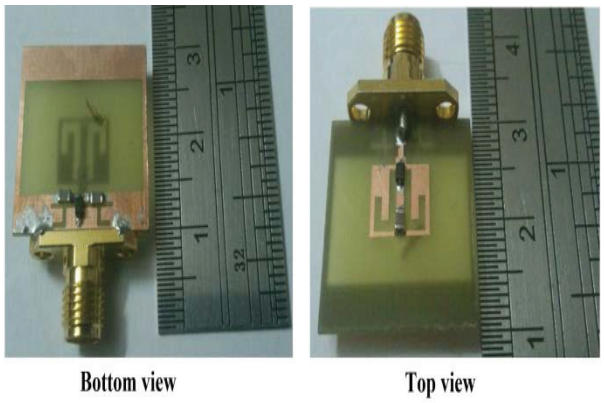

Fig. 8. The fabricated antenna.

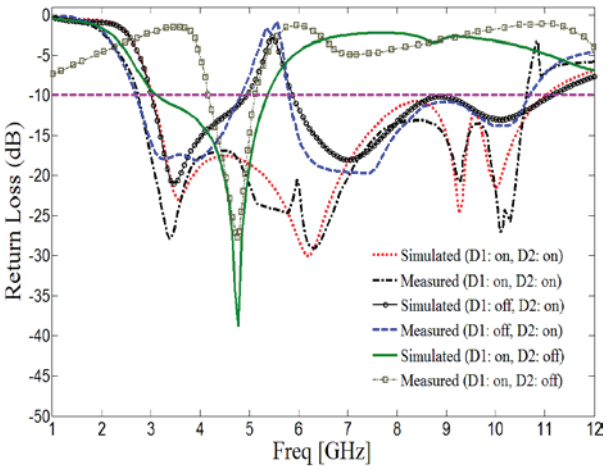

Fig. 9. Simulated and measured return loss characteristics for different performances of the proposed antenna.

The measured radiation patterns, including the co-polarization and cross-polarization in the E-plane (*y-z* plane) and H-plane (*x-z* plane) for different performances of the fabricated antenna, are shown in Fig. 10. The main purpose of presenting the radiation patterns is to demonstrate that the antenna actually radiates over a wide frequency band. It can be seen that the radiation patterns in *x-z* plane are nearly omnidirectional for different performances of the antenna at various operating frequencies.

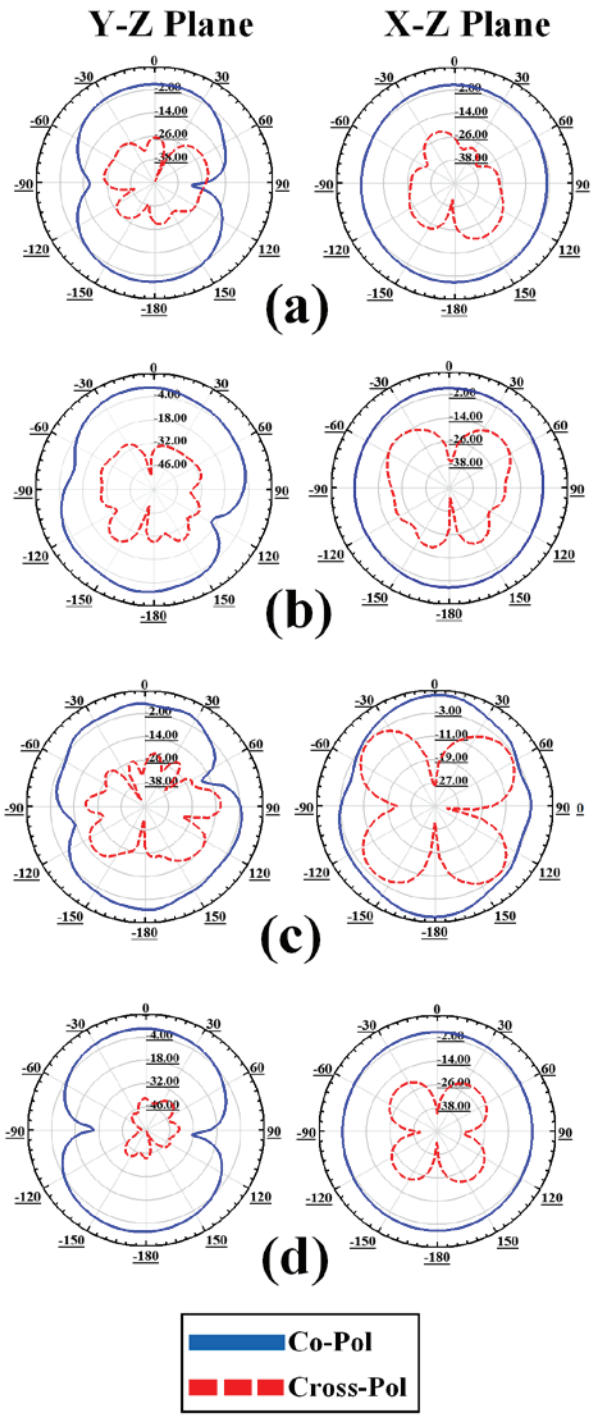

Fig. 10. Measured radiation patterns of the proposed antenna: (a) 5 GHz (D1: on, D2: off), (b) 5.5 GHz (D1: on, D2: on), (c) 10 GHz (D1: on, D2: on) and (d) 6 GHz (D1: off, D2: on).

V. CONCLUSION

In this letter, a novel compact reconfigurable printed slot antenna with switchable UWB (multi-resonance), UWB with band-notch function and single band performances has been proposed for UWB applications. By inserting a pair of notches in the feed-line of the ordinary slot antenna, wider impedance bandwidth can be obtained; especially at the higher band. Another additional resonance excitation at higher band is added to the antenna performance by etching two gamma-shaped slots on the radiating stub and a switchable single band-notch function is provided by embedding a PIN diode between these slots. By cutting two H-shaped slots on the ground plane and embedding a PIN diode across these slots, the antenna is capable of another switchable function between UWB and single band performances. By changing the biasing statuses of the PIN diodes, the antenna exhibits different desired functionalities. The fabricated antenna satisfies the return loss < 10 dB requirement from 2.7 GHz to 10.65 GHz, with a band rejection performance in the frequency band of 4.8 GHz to 5.83 GHz. The proposed antenna has a simple configuration and is easy to fabricate.

REFERENCES

[1] H. Schantz, The art and science of ultra wideband antennas, Artech House 2005.

[2] A. Valizade, Ch. Ghobadi, J. Nourinia, N. Ojaroudi, and M. Ojaroudi "Band-Notch Slot Antenna with Enhanced Bandwidth by Using Ω-Shaped Strips Protruded inside Rectangular Slots for UWB Applications," Applied Computational Electromagnetics Society (ACES) Journal, vol. 27, no. 10, pp. 816 – 822, October 2012.

[3] D. S. Javan, O. H. Ghouchani, "Cross Slot Antenna with U-Shaped Tuning Stub for Ultra Wideband Applications," Applied Computational Electromagnetics Society (ACES) Journal, vol. 24, no. 4, pp. 427 – 432, August 2009.

[4] R. Azim, M. T. Islam, and N. Misran, "Design of a Planar UWB Antenna with New Band Enhancement Technique," Applied Computational Electromagnetics Society (ACES) Journal, vol. 26, no. 10, pp. 856 – 862, October 2011.

[5] J. William, R. Nakkeeran, "A New UWB Slot Antenna with Rejection of WiMax and WLAN Bands," Applied Computational Electromagnetics Society (ACES) Journal, vol. 25, no. 9, pp. 787 – 793, September 2010.

[6] W. J. Lui, C. H. Cheng, Y. Cheng, et al., "Frequency notched ultra wideband microstrip slot antenna with a fractal tuning stub", *Electronic Lett.* 41, pp. 294–296, 2005.

[7] S.-W. Su, K.-L. Wong, and F.-S. Chang, "Compact printed ultra wideband slot antenna with a band notched operation," Microwave and Optical Tech. Letters, vol. 45, pp. 128–130, 2005.

[8] A. Valizade, Ch. Ghobadi, J. Nourinia, and M. Ojaroudi "A Novel Design of Reconfigurable Slot Antenna with Switchable Band Notch and Multi-Resonance Functions for UWB Applications," IEEE Antenna and Wireless Propagation Lett., vol. 11, pp. 1166-1169, October 2012.

[9] J.William and R.Nakkeeran, "CPW-Fed UWB slot antenna with reconfigurable rejection bands," *Proc. Of Int. Conf. on C ontrol, Communication and Power Engineering*, 2010.

[10] S. Nikolaou, N. D. Kingsley, G. E. Ponchak, J. Papapolymerou, and M. M. Tentzeris, "UWB elliptical monopoles with a reconfigurable band notch using MEMS switches actuated without bias lines," *IEEE Trans. Antenna and Propag.*, vol. 57, NO. 8, pp. 2242-2251, August 2009.

[11] P. S. Hall, P. Gardner, J. Kelly, E. Ebrahimi, M. R. Hamid, F. Ghanem, F. J. Martinez, and D. Vargas, "Reconfigurable antenna challenges for future radio systems," *Antennas and Propag., EuCAP 2009,* pp. 949-955.

[12] M. R. Hamid, P. Gardner, P. S. Hall, and F. Ghanem, "Switched-band Vivaldi antenna," IEEE Trans. Antennas Propagat., vol. 59, no. 5, pp. 1472–1480, May 2011.

[13] A. Tariq and H. Ghafouri-Shiraz, "Frequency-reconfigurable monopole antennas," *IEEE Trans. Antennas and P ropag.*, vol. 60, no. 1, pp. 44–50, Jan 2012.

[14] Ansoft High Frequency Structure Simulation (HFSS), Ver. 13, Ansoft Corporation, 2010.

Bahareh Badamchi was born in Urmia, Iran 1987. She received her B.Sc. in Electrical Engineering-Telecommunication from Urmia University, Iran, in 2011 and is currently a M.Sc. student in electrical engineering-telecommunication at the same university. Her research interests are in microstrip antennas, reconfigurable structures and cognitive radio.

Arash Valizade was born in Tehran, Iran 1986. He received his B.Sc. in electrical engineering-electronics from Azad University of Sabzevar, Iran, in 2008 and M.Sc. degrees in electrical engineering-telecommunication from Urmia University, Urmia, Iran, in 2012, and he is currently Ph.D. student at Semnan University, Semnan, Iran. His primary research interests are in numerical methods in electromagnetics, microstrip antenna design, microwave circuits, active integrated antenna and reconfigurable structures.

Pejman Rezaei was born in Tehran, Iran, in 1977. He received the B.S. degree in Electrical-Communication Engineering from Communication Faculty, Tehran, Iran, in 2000, and the M.S. and Ph.D. degrees from Tarbiat Modarres University, Tehran, Iran, in 2002 and 2007, respectively. Currently, he is assistant professor in the Semnan University, Semnan, Iran. His current research interests are Electromagnetics theory, theory and design of antenna, metamaterial structure, and satellite communication.

Zahra badamchi was born in Urmia, Iran, in 1989. She received her B.Sc. in electrical engineering-electronics from Urmia University, Iran, in 2013 and is currently a M.Sc. student in electrical engineering telecommunication at the Science and Research branch, Islamic Azad university, Urmia, Iran. Her research interests are in microstrip antennas, reconfigurable structures and cognitive radio.

Application of SVM and BCG-FFT Method for the Parameter Reconstruction of Composite Conducting-Dielectric Cylinder

Q. H. Zhang and H. T. Chen

Department of Electronics and Information
Three Gorges University, Yichang, Hubei 443002, China
zhangqh020901@163.com, hbcht@126.com

Abstract ─ In this paper, Support Vector Machine (SVM) technique is used to reconstruct the geometric and dielectric characteristics of composite conducting-dielectric cylinder. To this aim, the scattered electric fields at a number of observation points by composite conducting-dielectric object under the different object parameters are calculated by stabilized Biconjugate Gradient Fast Fourier Transform method (BCG-FFT) and provide to SVM as input training samples, while the output of the SVM are the characteristics of the objects. In numerical results, the proposed technique is applied successfully to the reconstruction of the geometric and dielectric parameters of composite conducting-dielectric cylinder. The effectiveness of the SVM method is evaluated and also in comparison with the Neural Network (NN) based approaches.

Index Terms ─ Biconjugate Gradient Fast Fourier Transform (BCG-FFT), composite conducting-dielectric cylinder, parameter reconstruction and Support Vector Machine (SVM).

I. INTRODUCTION

The research on the characteristics of electromagnetic scattering has particular significance in aspects of Electromagnetic Compatibility (EMC), target properties, classification and identification, radar sense, etc. of electromagnetism. In recent years, the research on characteristics of scattering of objective metallic and dielectric composite structure (such as lossy medium covers conductor objective, micro-strip, micro-strip antenna, antenna-antenna housing system and so on) has been paid great attention to because of its wide application. So it is obvious that the research on its aspects of inverse scattering appears to be quite imperative and important.

As for the calculation of unitary problems in electromagnetic inverse scattering of composite conducting-dielectric objects, we can adopt several comparatively mature algorithms, such as the Method of Moment (MoM), the Finite Element Method (FEM), the Finite Difference Time Domain (FDTD), etc. In MoM, a typical computational method for this problem is based on the Surface Integral Equation formulation (SIE) [1] or the hybrid Volume-Surface Integral Equation (VSIE) formulation [2-4]. In comparison to the SIE approach, the VSIE approach has several unique advantages. First, the VSIE approach can conveniently handle composite objects with arbitrarily inhomogeneous dielectric materials due to the use of VSIE, while the SIE can only consider piecewise homogeneous dielectric materials. Besides, for composite conducting-dielectric targets, the SIE approach requires special treatments on the conducting-dielectric junctions to obtain accurate results [5]. On the other hand, the VSIE approach retains the same simple form, regardless of the complexity of the objects. Hence, the implementation is relatively convenient and simpler, as compared to the SIE approach. Also, no special treatments are required for problems with junctions. In this paper, we chose the VSIE to model the composite conducting-dielectric objects.

At present, there are so few documents and reports about the aspects of electromagnetic inverse scattering of metallic and dielectric composite structure object. As for traditional

Submitted On: September 23, 2012
Accepted On: January 19, 2014

optimization iteration method, on one hand, its calculation on unitary algorithm is more complex than the calculation on comparatively pure conductor or dielectric objective, because of the complexity of objective structure; on the other hand, the complexity of objective structure causes the more powerful nolinear of the aspects of inversing scattering. At the same time, we also need to pay more attention to the slowdown or convergence of iteration caused by the increasing number of object functions and optimization variables, it is time-consuming and certainly it will go against synchronous inversion towards objective.

In the last years, it's seen that the application research on the aspect of Artificial Neural Networks (ANN) in electromagnetic inverse scattering has already been started up; such as the free space on the basis of frequency domain or time domain information, the problem of electromagnetism inversing scattering of half-space buried-objects [6-10], etc. However, in spite of their success, NN-based approaches suffer from typical problems of neural networks (e.g., the overfitting, local minima, etc), which make the method accuracy highly training dependent.

In recent years, a new artificial intelligent technique-Support Vector Machine (SVM) has been proposed to solve electromagnetic inverse scattering problems. In [11] and [12], the SVM is used to the detection of buried object by frequency-domain data of scattered electric fields, combined with the Finite Element Method (FEM) and the Finite Difference Time Domain (FDTD) method, respectively. In particular, as in the case of the using of neural networks, SVM are used to estimate the unknown function that relates the scattering field to the target's properties. After a proper learning phase, the SVM can obtain reconstruction in real-time. Moreover, in SVM, the original problem is recasted into a Constrained Quadratic Programming (CQP) problem and it avoids typical drawbacks as overfitting or local minima occurrence [13].

This paper deals with the SVM-based reconstruction of composite conducting-dielectric objects starting from frequency-domain electromagnetic scattering data. To this aim, the stabilized Biconjugate Gradient Fast Fourier Transform method (BCG-FFT) is applied to solve the hybrid VSIE for composite conducting-dielectric cylinder, and the electromagnetic data exploitable for inversion are the amplitude of scattered fields collected at some receiving points.

II. THE MATHEMATICAL FORMULATION OF VSIE

Let's consider a mixed conducting and dielectric scattering target illuminated by an incident field $\boldsymbol{E}^i$. It is assumed that the dielectric materials are nonmagnetic, namely, $\mu=\mu_0$ for all regions and in the following formulation the time factor is $e^{j\omega t}$ and is suppressed. Using the equivalence principle, the conducting bodies are replaced by equivalent surface currents $\boldsymbol{J}_S$ and the dielectric materials are replaced by equivalent volume currents $\boldsymbol{J}_V$. All the currents radiate in free space, and hence the free-space Green's function is used in the formulation. The scattered field $\boldsymbol{E}^s$ is the total contribution of the surface current $\boldsymbol{J}_S$ and volume current $\boldsymbol{J}_V$, which can be calculated by [4]:

$$\boldsymbol{E}^s(\boldsymbol{r}) = -\mathrm{j}\omega \boldsymbol{A}_S(\boldsymbol{r}) - \nabla\Phi_S(\boldsymbol{r}) - \mathrm{j}\omega \boldsymbol{A}_V(\boldsymbol{r}) - \nabla\Phi_V(\boldsymbol{r}), \quad (1)$$

where $\boldsymbol{A}_S, \boldsymbol{A}_V, \Phi_S, \Phi_V$ are the vector and scalar potentials produced by the surface current $\boldsymbol{J}_S$ and volume current $\boldsymbol{J}_V$, respectively; and given by:

$$\boldsymbol{A}_u(\boldsymbol{r}) = \frac{\mu_0}{4\pi}\int_u \boldsymbol{J}_u(\boldsymbol{r}')\frac{e^{-jk_0|\boldsymbol{r}-\boldsymbol{r}'|}}{|\boldsymbol{r}-\boldsymbol{r}'|}\mathrm{d}u' \quad u = S, V, \quad (2)$$

$$\Phi_u(\boldsymbol{r}) = -\frac{1}{\mathrm{j}\omega 4\pi\varepsilon_0}\int_u \nabla\cdot\boldsymbol{J}_u(\boldsymbol{r}')\frac{e^{-jk_0|\boldsymbol{r}-\boldsymbol{r}'|}}{|\boldsymbol{r}-\boldsymbol{r}'|}\mathrm{d}u' \quad u = S, V. \quad (3)$$

On all conductor surfaces S, the boundary condition requires that the total tangential electric field is zero; i.e.:

$$\left[\boldsymbol{E}^i(\boldsymbol{r}) + \boldsymbol{E}^s(\boldsymbol{r})\right]_{\tan} = 0 \quad \boldsymbol{r}\in S. \quad (4)$$

This is the surface electric field integral equation. In the dielectric region, the total electric field is equal to the sum of the incident field and the scattered field; i.e.:

$$\boldsymbol{E}^{\mathrm{total}}(\boldsymbol{r}) = \boldsymbol{E}^{\mathrm{i}}(\boldsymbol{r}) + \boldsymbol{E}^{\mathrm{s}}(\boldsymbol{r}) \quad \boldsymbol{r}\in V, \quad (5)$$

the volume current $\boldsymbol{J}_V$ is related to the total electric field $\boldsymbol{E}^{\mathrm{total}}(\boldsymbol{r})$ by:

$$\boldsymbol{J}_V(\boldsymbol{r}) = \mathrm{j}\omega(\varepsilon(\boldsymbol{r}) - \varepsilon_0)\boldsymbol{E}^{\mathrm{total}}(\boldsymbol{r}) \quad \boldsymbol{r}\in V, \quad (6)$$

where $\varepsilon(\boldsymbol{r})$ is the permittivity of the dielectric material.

Put equation (5) into equation (6), the volume integral equation is given by:

$$\frac{\boldsymbol{J}_V(\boldsymbol{r})}{\mathrm{j}\omega(\varepsilon(\boldsymbol{r})-\varepsilon_0)}=\boldsymbol{E}^{\mathrm{i}}(\boldsymbol{r})+\boldsymbol{E}^{s}(\boldsymbol{r}) \quad \boldsymbol{r}\in V. \tag{7}$$

Equations (4) and (7), together with (1)-(3), constitute a hybrid volume-surface integral equation in terms of the surface current $\boldsymbol{J}_S$ on the conducting surface and the volume current $\boldsymbol{J}_V$ in the dielectric region.

To solve the hybrid volume-surface integral equation, the conducting surface S is discretized into small quadrangle patches, while the dielectric region V is divided into hexahedron elements. However, the quadrangle-hexahedron mesh is not the only choice. Other types of meshes, such as triangular for surface and tetrahedral for volume can also be used. The unknown surface current $\boldsymbol{J}_S$ and volume current $\boldsymbol{J}_V$ can be represented by the pulse basis functions and be substituted into (4) and (7), testing a linear system consisting of independent equations is obtained and can be written as a sub-matrix form in the following:

$$\begin{bmatrix} Z_{SS} & Z_{SV} \\ Z_{VS} & Z_{VV} \end{bmatrix}\begin{bmatrix} I_{sn} \\ I_{vn} \end{bmatrix}=\begin{bmatrix} E^i_{sn} \\ E^i_{vn} \end{bmatrix}, \tag{8}$$

where $Z_{tu}\,(u=S,V,t=S,V)$ is the impedance matrix, I_{sn}, I_{vn} are the expansion coefficient matrix of surface current and volume current, respectively and E^i_{sn}, E^i_{vn} are the electric voltage matrix of metal surface and dielectric internal, respectively. Once we get the surface current $\boldsymbol{J}_S$ and volume current $\boldsymbol{J}_V$ by matrix equation (8), we can get the scattering field of arbitrary point in space, as long as we put them into equation (1). Specifically, the numerical integration involved in the sub-matrix Z_{SS} and Z_{VV}, $a_t=\int_t G(\boldsymbol{r},\boldsymbol{r}')d\boldsymbol{t}'$ ($t=S,V$), will show singularity when $\boldsymbol{r}=\boldsymbol{r}'$; i.e., the field point coincides with source point. To avoid this singularity, an approximate numerical method should be taken to yield accurate result. As for the surface integral, it can be solved approximately by solving the integral within the corresponding circular whose area is equal to rectangle in polar coordinate. In terms of volume integral, we use the integration of the sphere, which has the equal volume of the cube to obtain the numerical solution:

$$I_1=j\omega\mu_0[\frac{1}{k_0^2}(e^{-jk_0r_0}-1)-\frac{1}{jk_0}r_0e^{-jk_0r_0}], \tag{9}$$

where $r_0=\sqrt[3]{\frac{3\Delta V}{4\pi}}$ is the radius of the sphere whose volume is equal to the ΔV of the cube volume.

Along with the development of computer technology, as for the solving of matrix equation (8), there have been brought forward numerous fast algorithms towards the matrix equation solving. Fast algorithms which are frequently used, includes Fast Multipole Method (FMM) [14] and its extension, the Multilevel Fast Multipole Algorithm (MLFMA) [15], Conjugate Gradient Gast Fourier Transform method (CG-FFT) [16], the Adaptive Integral Method (AIM) [17], etc.; which are all being obtained with widely application. This paper adopts stable BCG-FFT method [18], which provides the solving of the aspects of electromagnetic inverse scattering with high-performance unitary algorithm, along with the effective reduction of memory requirements and computation time of computer.

III. SVM-BASED INVERSE SCATTERING PROCEDURE

Generally speaking, a regression problem is the process through when an unknown function f is approximated by means of a function $\overline{f}$ on the basis of some sample $\{(\underline{v_n},e_n)\}_{n=1,\ldots,N}$, being $\underline{v_n}$ an input pattern and e_n the corresponding target ($e_n=f\{\underline{v_n}\}$). As far as parameters reconstruction of composite conducting-dielectric object are concerned, the dimension (r) and the complex permittivity (ε_r,σ) of the scatter must be retrieved and each unknown parameters is dealt with separately. Consequently, $\underline{v_n}=(\underline{E^s})_n$ and $e_n=(\chi_i)_n$.

SVM is a new paradigm that have been recently proposed for the solution of pattern recognition and function approximation tasks. Briefly (the reader can refer to [19] for more details), the SVM-based procedure aim at finding a smooth function $\overline{f}$ that approximates f while

keeping at most, a deviation ε from the targets e_n for all samples. Thus, f is approximated in a linear way:

$$\overline{f}(\underline{v}) = w \cdot \Phi(\underline{v}_n) + c, \tag{10}$$

where w represents the vector of weights of the linear function, $\Phi(\cdot)$ is the mapping that projects the samples from the original into the higher dimensional feature space and c is the bias.

The optimal linear function in the transformed space is selected by minimizing the structural risk, which is the combination of the training error (empirical risk) and the model complexity (confidence term). The first term is calculated according to a $\varepsilon-$ insensitive loss function and can be expressed by means of nonnegative slack variables ξ and ξ^*, which measure the distance (in the target space) of the training samples lying outside the $\varepsilon-$ insensitive tube from the tube itself. The second term of the cost function is expressed through the Euclidean norm of the weight vector w, which can be inversely related to the geometrical margin of the corresponding solution and thus, to the complexity of the model. The cost function to minimize becomes:

$$\Psi(w,\xi) = C\sum_{n=1}^{N}(\xi+\xi^*) + \frac{1}{2}\|w\|^2, \tag{11}$$

subjected to the following constraints:

$$\begin{cases} e_n - [w\cdot\Phi(\underline{v}_n)+c] \le \varepsilon + \xi_n, \\ [w\cdot\Phi(\underline{v}_n)+c] - e_n \le \varepsilon + \xi_n^*, \quad n=1,2,...,N, \\ \xi_n, \xi_n^* \ge 0, \end{cases} \tag{12}$$

C is a regularization parameter that allows one to tune the tradeoff between the complexity (or flatness) of the function $\overline{f}$ and the tolerance to empirical errors.

The constrained optimization problem in (11) can be reformulated through a Lagrange function, which leads in the dual formulation to a Convex Quadratic Problem (CQP) and thus, to a unique solution (the global minimum of the cost function). The final prediction function in terms of the samples in the original input domain, becomes:

$$\overline{f}(\underline{v}) = \sum_{n\in N}(\alpha_n - \alpha_n^*)k(\underline{v}_n, \underline{v}) + c, \tag{13}$$

where α_n and α_n^* represent the Lagrange multipliers of the CQP and $k(.,.)$ is a kernel function, which allows one to evaluate the similarity between a pair of sample in the transformed feature space as a function of the samples in the input space. The commonly adopted kernels are polynomial and Gaussian Radial Basis Function (RBF) kernels. In SVM, the samples associated with a nonzero Lagrange multiplier are called support vectors, the other samples have no weight in the definition of the result since they fall within the $\varepsilon-$ tube. The CQP problem can be solved using standard optimization techniques. In this work, a very effective procedure, Sequential Minimal Optimization (SMO) [20] is adopted. The parameter c can be computed by means of the Karush-Kuhn-Tucker conditions of the CQP at optimality [19].

Some attractive features of the SVM result from the analytical formulation presented earlier and are as follows [21]:

1) Good intrinsic generalization ability, owing to the use of the $\varepsilon-$ insensitive cost function and the optimization of both empirical error and model complexity to drive learning process;
2) Limited complexity and high stability of the learning process, due to the convexity of the optimization problem and the use of the kernel trick;
3) Ease of use, since relativity few free parameters (or hyperparameters; i.e., the regularization coefficient C, the width of the insensitive tube ε and the kernel types and parameters) have to be tuned.

IV. NUMERICAL RESULTS

A. The electromagnetic scattering of composite conducting-dielectric objects

In order to prove the correctness, two valuable objects of two-dimension metal/dielectric composite structure are considered by BCG-FFT method and making comparison with the FDTD method.

1) Inhomogeneous medium covering conducting cylinder.

A unit TM plane wave reflects upon the indefinite medium covering conductor cylinder along X-axis (suppose the cylinder axis is Z-axis), the radius of conductor is 0.2λ and the thickness of medium is 0.1λ; two kinds constitute the medium and the relative dielectric constants are $\varepsilon_{r1} = 4.0$, $\varepsilon_{r2} = 20.0$, respectively. Medium 1

locates under X-axis, which medium 2 is above X-axis. Figure 1 provides with the bistatic Radar Cross Section (RCS) σ of the object (using normalization of wavelength). The result obtained by FDTD also shown in the figure, which indicates good correspondence with the result of the approach above. It is worth noting that some deviation are shown in the range of $200^0 - 300^0$. This can be explained in the following two aspects: first, the relative simple substitute of rectangle to cube, which may cause deviation and the another may result from the process of central point matching.

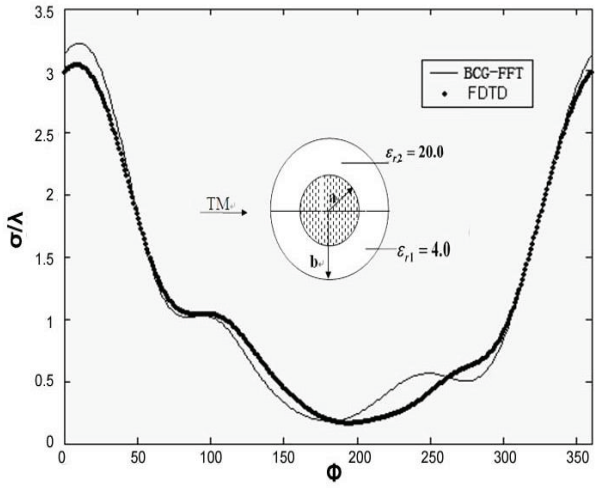

Fig. 1. Bistatic RCS of a conducting cylinder ($ka = 1.256$) with a inhomogeneous coating ($kb = 1.884$, $\varepsilon_r = 4.0$ and 20.0).

2) Metal-medium constituting the compound square column.

A unit TM plane wave reflects into the object of metal/medium composite square column, the angle of arrival is $\varphi = 270^0$, half the object is a conductor (left), while half the object is a medium (right); both of the cross sections of the metal and the medium are squares with the length of a side 0.2λ and the relative permittivity is 4.0. Figure 2 puts up the σ of the object. It's obtained result matches with the result of the document [22] and Fig. 2 also provides with the computing result of FDTD.

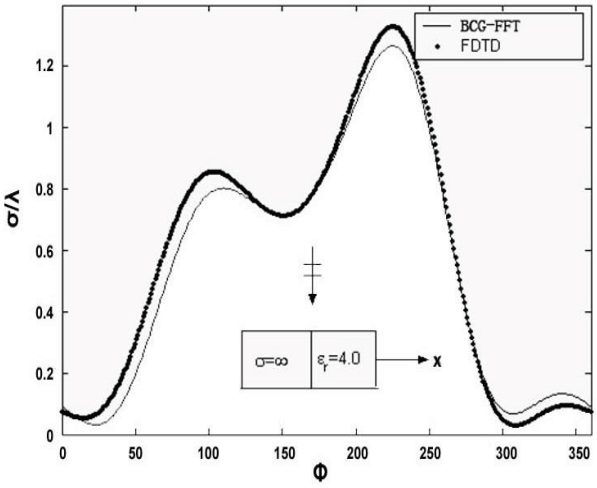

Fig. 2. Bistatic RCS of a composite conducting dielectric square column with the length of side 0.2λ and relative permittivity 4.0.

B. The reconstruction of composite conducting-dielectric cylinder

1) The reconstitution of the relative permittivity ε_r and the medium covering thickness b.

A unit TM plane wave ($f = 1GHz$) vertically reflects into the lossless medium covering conductor cylinder (Fig. 3) with its inside radius and outer radius are a and b, respectively; $a = \lambda/6$, suppose the values range of b is at [7, 23] cm, while the values range of ε_r is at [1.5, 5.0]. In the "learning phase", a data set of 135 examples:

$\varepsilon_r = 1.5 + 0.25n$, $n = 0,1,...,14$, $b = 7.0 + 2n(cm)$, $n = 0,1,...,8$, is considered and defined a suitable set to train SVM for the reconstruction problems. Because SVM has been developed to solve one-output learning problems [19], two different SVMs, one for the reconstitution of the relative permittivity ε_r and the other for the reconstitution of the medium covering thickness b are trained by using the SMO algorithm. Gaussian RBF kernel (with kernel width γ^2) are considered as kernel functions, due to their capability to work as universal approximator [11]. In order to obtain the scattering electric field of objective truly and perfectly, we place 12 observation points of scattered filed, which evenly distribute at the

distance from the circular arc with the center radius of λ and the length of $3\pi\lambda/2$, just as Fig. 3 shows. The sample information are all the amplitude of scattered field of observation point, which can directly get by the analytic method. After proper trained, the values of the hyperparameters of the SVM are given in Table 1.

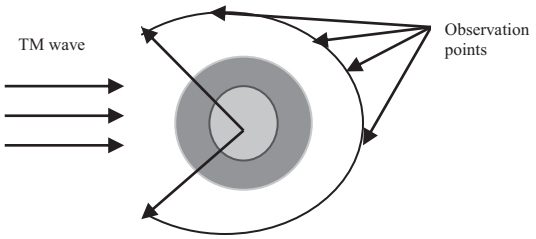

Fig. 3. Conductor cylinder coated with dielectric material illuminated by a plane wave.

Table 1: The values of the SVM hyperparameters

	ε	C	γ^2
ε_r	0.001	999.8545	0.2460
b	0.001	1004.6867	0.2441

In order to compare SVM and NN performances under the same "conditions", the same training set has been considered during the NN training phase. In this studies, the network structure having 12 input ports, 12 nodes in the hidden layer and 2 output ports (means 12-12-2 network) is considered. In training phase, a Backpropagation algorithm is used to train the NN (BPNN) in this work.

The performances of the BPNN and SVM-based procedure are illustrated and compared by considering a test set made up of 96 examples ($\varepsilon_r = 1.55, 1.80, 2.05, 2.30, 2.55, 2.76, 3.05, 3.30, 3.80, 4.50, 4.55, 4.90$; $b = 8.0 + 2n(cm)$, $n = 0,1,...,7$). The relative permittivity ε_r and radius b are different from those of the training set. Figures 4 and 5 show the estimated versus the actual scatterer properties when the SVM-based and BPNN-based approaches are taken into account, respectively.

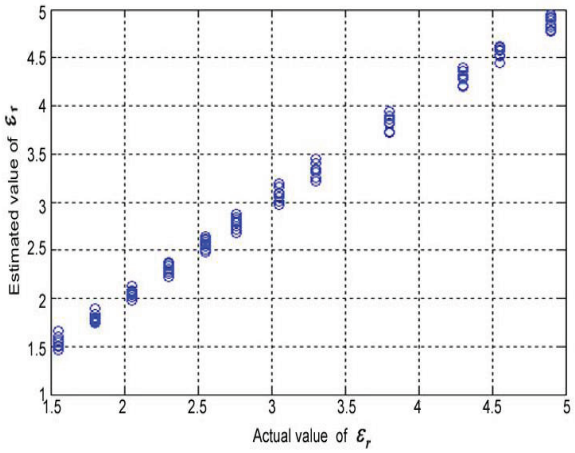

(a)

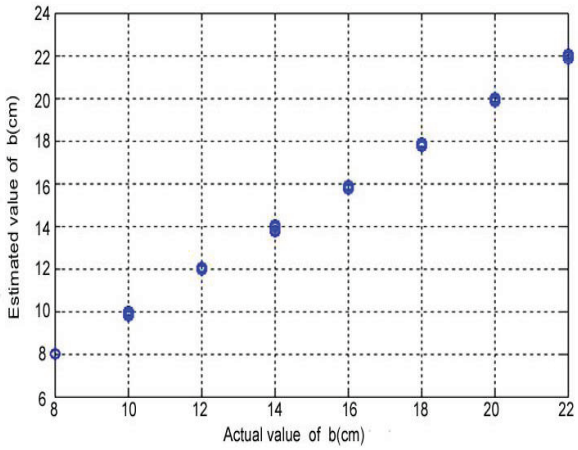

(b)

Fig. 4. SVM-based approach. Estimated versus real scatterer properties: (a) ε_r and (b) b.

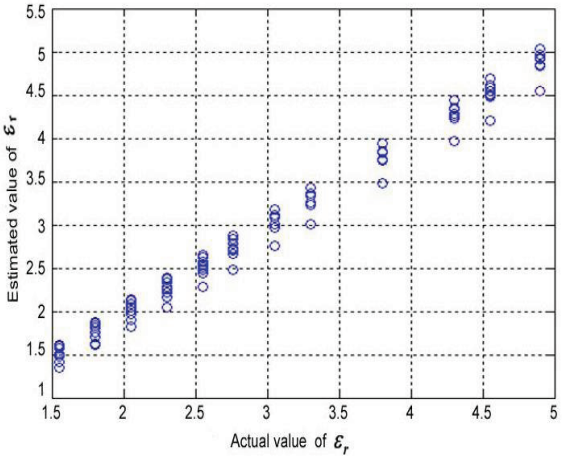

(a)

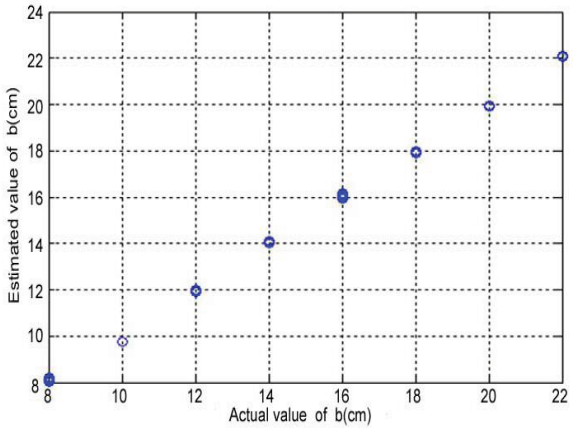

(b)

Fig. 5. BPNN-based approach (12-12-2). Estimated versus real scatterer properties: (a) ε_r and (b) b.

Results of the reconstruction errors are summarized in Table 2, where the Maximum Absolute Error (MAE), Average Absolute Error (AAE), Maximum Relative Error (MRE) and Average Relative Error (ARE) achieved in the reconstruction are listed. As can be seen, reconstruction results are very good, since both the relative permittivity and the medium covering thickness are reconstructed with an average relative error less than 2%. Comparison of the performance of the 12-12-2 network is carried out by examining the results summarized in Table 3. As expected, SVM enhances the performances achieved with the BPNN approach, due to the solution of the CQP problems.

Table 2: Errors in the reconstruction of ε_r and b achieved by using the SVM

	MAE	AAE	MRE	ARE
ε_r	0.1518	0.0532	7.20%	1.88%
b	0.2992	0.0835	2.31%	0.57%

Table 3: Errors in the reconstruction of ε_r and b achieved by using the BPNN (12-12-2)

	MAE	AAE	MRE	ARE
ε_r	0.3494	0.0900	12.87%	3.27%
b	0.2601	0.0972	2.74%	0.83%

2) The reconstitution of the relative permittivity ε_r, the medium covering thickness b and the conductivity σ.

In this example, the installation of incident wave, objects and observation points shares the same as the last example. The total number of training samples is 800 and the training set's variation rules are: $\varepsilon_r = 1.5 + 0.4n, n = 0,1,...,9$, $b = 8.0 + 2.0n\,(cm)$, $n = 0,1,...,7$ and $\sigma = 10^{-3+0.1n}\,(S/m), n = 0,1,...,9$, respectively. After training phase, the values of the hyperparameters are given in Table 4.

Table 4: The values of the SVM hyperparameters

	ε	C	γ^2
ε_r	0.001	1001.8193	0.1665
b	0.01	1000.1480	0.1667
σ	0.00001	10000	0.2512

Results refer to the processing of a test set made up of 216 examples that do not belong to the training set: $b = 9.0 + 2n\,(cm), n = 0,1,...,5$; $\varepsilon_r = 1.65, 2.05, 2.5, 3.3, 4.0, 4.9$; $\sigma = 10^{-t}\,(S/m)$, $t = 2.95, 2.81, 2.75, 2.55, 2.35, 2.15$. The sample information is the amplitude of scattering field of observation points, we can get it with BCG-FFT method. Figure 6 shows the estimated versus the actual scatterer properties. Table 5 shows the results of the reconstruction errors. Under the same conditions, similar results have been obtained also when the BPNN (12-12-3) approach is adopted for reconstruction problems and are given in Table 6.

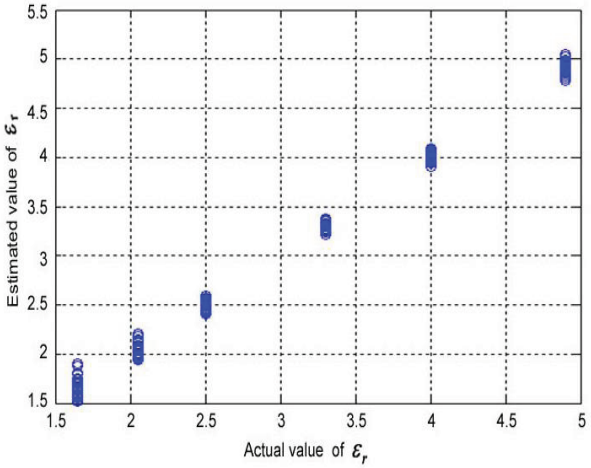

(a)

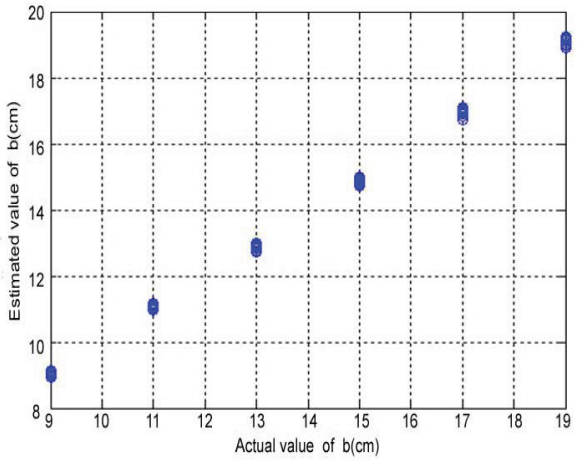

(b)

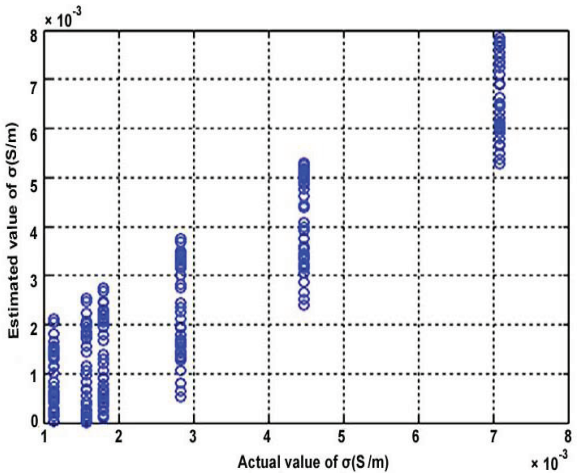

(c)

Fig. 6. SVM-based approach. Estimated versus real scatterer properties: (a) ε_r, (b) b and (c) σ.

Table 5: Errors in the reconstruction of ε_r 、 b and σ achieved by using the SVM

	MAE	AAE	MRE	ARE
ε_r	0.2032	0.0533	12.32%	1.92%
b	0.2004	0.0727	1.82%	0.56%
σ	0.0020	5.3987e-4	181.48%	25.81%

Table 6: Errors in the reconstruction of ε_r 、 b and σ achieved by using the BPNN (12-12-3)

	MAE	AAE	MRE	ARE
ε_r	0.2550	0.0531	15.45%	2.15%
b	0.2900	0.1001	2.23%	0.74%
σ	0.0023	7.8362e-4	99.61%	34.46%

Figure 6 shows the estimated versus the actual scatterer properties when the SVM-based approach is taken into account. As for the reconstruction of relative permittivity ε_r and the medium covering thickness b, from Tables 5 and 6, both of those two methods result sound; what's more, SVM method has an advantage over BPNN method. However, both of those methods also result in big relative errors during the reconstruction of the conductivity σ. It is possible that the big error just corresponds to the small actual value according to theoretical analysis.

V. CONCLUSION

In this letter, an innovative inverse scattering methodology, based on the implementation of a support vector machine has been presented and applied to the reconstruction of composite conducting-dielectric objects. The samples data fed to the SVM are the amplitude of scattered fields from composite conducting-dielectric objects collected at some receiving points and obtained by using the BCG-FFT method. The training of SVM requires the solution of a constrained quadratic optimization problem. This is a key point of the proposed approach, which can overcome the typical drawbacks as over-fitting or local minima occurrence (with respect to NN). The efficiency of the proposed technique was illustrated in the case of the reconstruction of geometric and dielectric properties of composite conducting-dielectric objects. Some numerical results validate the accuracy and efficiency of the method by comparing with the BPNN method.

ACKNOWLEDGMENT

This work was supported by the National Natural Science Foundation of China (No. 61179025) and the Natural Science Foundation of Hubei Provincial Department of Education (No. D20111201).

REFERENCES

[1] S. M. Rao, C. C. Cha, R. L. Cravey, and D. L. Wilkes, "Electromagnetic scattering from arbitrary shaped conducting bodies coated with lossy materials of arbitrary thickness," *IEEE Trans. Antennas Propag.*, vol. 39, no. 5, pp. 627-631, 1991.

[2] T. K. Sarkar and E. Arvas, "An integral equation approach to the analysis of finite microstrip

antennas: volume/surface formulation," *IEEE Trans. Antennas Propag.*, vol. 38, no. 3, pp. 305-313, 1990.

[3] C. C. Lu and W. C. Chew, "A coupled surface-volume integral equation approach for the calculation of electromagnetic scattering from composite metallic and material targets," *IEEE Trans. Antennas Propag.*, vol. 48, no. 12, pp. 1866-1868, 2000.

[4] X. C. Nie, N. Yuan, L. W. Li, Y. B. Gan, and T. S. Yeo, "A fast volume-surface integral equation solver for scattering from composite conducting-dielectric objects," *IEEE Trans. Antennas Propag.*, vol. 53, no. 2, pp. 818-823, 2005.

[5] M. A. Carr, E. Topsakal, J. L. Volakis, and D. C. Ross, "Adaptive integral method applied to multilayer penetrable scatterers with junctions," *In IEEE Antennas Propag. Soc. Int. Sypm.*, pp. 856-861, 2001

[6] R. Mydur and K. A. Michalski, "A neural network approach to the electromagnetic imaging of elliptic conducting cylinders," *Microwave Opt. Technol. Lett.*, vol. 28, no. 5, pp. 303-306, 2001.

[7] I. T. Rekanos, "On-line inverse scattering of conducting cylinders using radial basis-function neural networks," *Microwave Opt. Technol. Lett.*, vol. 28, no. 6, pp. 378-380, 2001.

[8] E. Bermani, S. Caorsi, and M. Raffetto, "An inverse scattering approach based on a neural network technique for the detection of dielectric cylinders buried in a lossy half-space," *PIER*, vol. 26, pp. 67-87, 2000.

[9] E. Bermani, S. Caorsi, and M. Raffetto, "Microwave detection and dielectric characterization of cylindrical objects from amplitude-only data by means of neural networks," *IEEE Trans. Antennas Propag.*, vol. 50, no. 9, pp. 1309-1314, 2002.

[10] E. Bermani, S. Caorsi, and M. Raffetto, "Geometric and dielectric characterization of buried cylinders by using simple time-domain electromagnetic data and neural networks," *Microwave Opt. Technol. Lett.*, vol. 24, no. 1, pp. 24-31, 2000.

[11] E. Bermani, A. Boni, S. Caorsi, and A. Massa, "An innovation real-time technique for buried object detection," *IEEE Trans. Geosci. Remote Sens.*, vol. 41, no. 4, pp. 927-931, 2003.

[12] Q. H. Zhang, B. X. Xiao, and G. Q. Zhu, "Inverse scattering by dielectric cylinder using support vector machine approach," *Microwave Opt. Technol. Lett.*, vol. 49, no. 2, pp. 372-375, 2007.

[13] V. Vapnik, "Statistical learning theory," *New York: Wiley*, 1998.

[14] R. Coifman, V. Rokhlin, and S. Wandzura, "The fast multipole method for the wave equation: a pedestrian prescription," *IEEE Antennas Propag.*, vol. 35, pp. 7-12, 1993.

[15] J. M. Song, C. C. Lu, and W. C. Chew, "Multilevel fast-multipole algorithm for electromagnetic scattering by large complex objects," *IEEE Trans. Antennas Propag.*, vol. 45, no. 10, pp. 1488-1493, 1997.

[16] T. K. Sarkar, E. Arvas, and S. M. Rao, "Application of FFT and conjugate gradient method for the solution of electromagnetic radiation from electrically large and small conducting bodies," *IEEE Trans. Antennas and Propagate.*, vol. 34, no. 5, pp. 635-640, 1986.

[17] E. Bleszynski, M. Bleszynski, and T. Jaroszewicz, "AIM: adaptive integral method for solving large scale electromagnetic scattering and radiate on problems," *Radio Sci.*, vol. 31, pp. 1225-1251, 1996.

[18] X. M. Xu, Q. H. Liu, and Z. Q. Zhang, "The stabilized biconjugate fradient fast fourier transform method for electromagnetic scattering," *J. Appl. Computat. Electromagn.*, vol. 17, no. 1, pp. 97-103, 2002.

[19] N. Cristianini and J. S. Taylor, "An introduction to support vector machine," *Cambridge Univ. Press*, Cambridge, U.K., 2000.

[20] J. Platt, "Fast training of support vector machine using sequential minimal optimization," *In: B. Scolkopf, C. Burges, and A. Smola (Eds.)*, "Advances in kernel methods-support vector learning," *MIT Press*, Cambridge, MA, 1999.

[21] L. Pasolli, C. Notarnicola, and L. Bruzzone, "Estimating soil moisture with the support vector regression technique," *IEEE Geoscience and Remote Sensing Letters*, vol. 8, no. 6, pp. 1080-1084, 2011.

[22] A. Z. Elsherbeni and A. A. Kishk, "Modeling of cylindrical objects by circular dielectric and conducting cylinders," *IEEE Trans. Antennas and Propag.*, vol. 40, no. 1, pp. 96-99, 1992.

Zhang Qing-he (S' 92-M' 07) received his B.S. degree from the Central China Normal University, Wuhan, China, and his Ph.D. degrees from the Wuhan University, Wuhan, China, in 1992 and 2007, respectively; both in Radio Physics. Since 2007 he has been with the School of Science of the China Three Gorges University as an Associate Professor. His research interests include microwave remote sensing of the sea and land surface, computational electromagnetics and application of neural networks and fuzzy systems in inversion problems.

A Miniaturized Omni-directional Negative Permittivity Zeroth-Order Resonance Antenna

Ming-Chun Tang [1], Tianwei Deng [2], Han Xiong [1], Shaowei Qing [3], and Hao Zeng [1]

[1] College of Communication Engineering
Chongqing University, Chongqing 400044, China
tangmingchunuestc@126.com, xiong1226han@126.com, haoz@cqu.edu.cn

[2] Department of Electrical & Computer Engineering
National University of Singapore (NUS), 119077, Singapore
tsldt@nus.edu.sg

[3] Power Engineering Institute
Chongqing University, Chongqing 400044, China
qshaowei@gmail.com

Abstract — An Evolved Negative permittivity (ENG) Zeroth-Order Resonance (ZOR) antenna with miniaturized size and ultra-low profile is presented in this paper. By adding parasitic patch and loading meander line in steps, the antenna ZOR operational frequency is decreased from 5.084 GHz to 177.8685 MHz, while keeping the overall dimensions unchanged; which is equivalent to about twenty-eight times electrical size reduction based on the equivalent circuit models. Moreover, the proposed miniaturized antenna with omni-directional radiation performance is promising for the specific low-power radio applications, such as short range remote control system and household security system.

Index Terms — Evolved negative permittivity, low-profile, miniaturization, zeroth-order resonance antenna.

I. INTRODUCTION

With the ever increasing demand for compact wireless communication system, which includes mobile and Wireless Local Area Network (WLAN) systems, miniature antenna has gained significantly more attentions in recent years. In order to achieve antenna miniaturization, lots of effective techniques have been proposed since the fundamental limitations of miniature antennas were theoretically explored since 1940's [1-2]. Hitherto, examples of antenna miniaturization techniques include using Genetic Algorithms (GA) method [3-4]; resorting to meander or Peano line [5-6], reactive/slot loading [7-12], negative permittivity (ENG)/negative permeability (MNG) Metamaterial (MTM) shells [13-16] and left-handed Transmission Lines (TL) loadings [17]. Employing high dielectric constant [18], magneto-dielectric [19], Artificial Magnetic Conductor (AMC) [20] and MNG metamaterial [21] substrates; utilizing Split-Ring Resonator (SRR) structures [22-23] and applying the MTM TL approach. For particular interest, miniature antennas based on MTM TL approach have drawn much attention and were extensively reported for their unique performance resulting from the rich dispersion of MTM TL materials. Generally, these MTM TL based antennas could be classified into the following three categories: Composite Right/Left Handed (CRLH) antennas [24-26], MNG Zeroth-Order Resonance (ZOR) antennas [27] and ENG ZOR antennas [28-32]. All of these MTM TL antennas could function in ZOR mode, which is independent on its physical length. However, as is known, the overall configurations of the metamaterial unit are quite crucial for their performance, while satisfying the

Submitted On: October 30, 2013
Accepted On: June 28, 2014

demands in specific applications, such as radiation gain, bandwidth and miniaturization level. On one hand, in order to improve the radiation gain, a special MTM TL metamaterial with equilateral slots on ground plane, which makes the resonator store less electromagnetic energy in the zeroth-order mode, was reported in [25]. On the other hand, the bandwidth of the MTM TL antennas has been distinctly broadened with the aid of mushroom structure [29]. However, up to now, there was little literature to comprehensively discuss how to achieve the further electrical reduction of MTM TL based antenna.

In this paper, according to the equivalent circuit models, a miniature ENG ZOR antenna with the overall dimensions $0.00954\lambda_0 \times 0.00954\lambda_0 \times 0.000475\lambda_0$ (where λ_0 is the wavelength corresponding to the operational frequency f_0 in free space) is successfully designed and manufactured, via an evolution of a traditional ENG ZOR antenna by following two effective steps: (1) additional capacitance was created by resorting to the virtual ground and (2) by etching meander-line, additional inductance and capacitance were obtained.

II. AN ENG ZOR ANTENNA DESIGN

According to the literatures [28-32], a compact one-unit-cell ENG ZOR antenna was constructed and the topology is shown in Fig. 1. In this design, a substrate with the thickness of 0.8 mm, relative dielectric constant ε_r=3.38 and loss tangent tanδ=0.0007 is selected. Considering the input resistance for these types of antennas is inherently much higher than the characteristic impedance of feed line [28-29], a feeding gap is employed so that the high input resistance could be reduced to match the 50 Ω characteristic impedance. The configuration was numerically simulated using Ansoft HFSS (a commercial electromagnetic solver based on finite element method) [33]. The results in Fig. 2 demonstrate that the proposed ENG antenna operates in the center of 5.084 GHz, which is corresponding to the overall dimensions of $0.273\lambda_0 \times 0.273\lambda_0 \times 0.0136\lambda_0$. As has been proven in [28], for such ENG antenna, the ZOR mode resonance frequency serves as the lowest operational frequency.

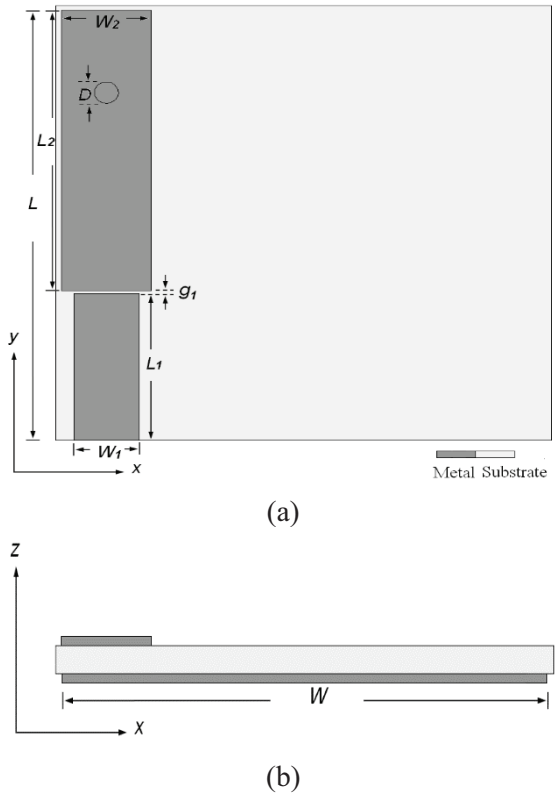

Fig. 1. Proposed ENG ZOR antenna: (a) front view and (b) side view. The dimensions in mm are: L=16.08, W=16.08, L_1=5.49, W_1=2.18, g_1=0.11, L_2=10.48 and W_2=3.

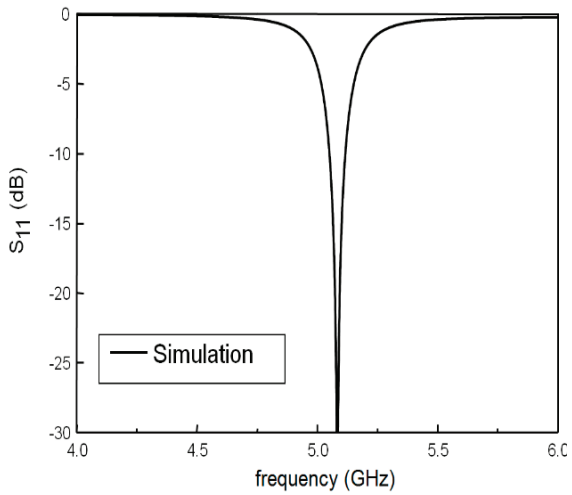

Fig. 2. Simulated reflection coefficients of ENG ZOR antenna.

Figure 3 gives the topology of equivalent circuit model for the proposed ENG ZOR antenna

based on [28-32]. In the model, C_0 is the couplingcapacitance between patch and feed line. The part in the dot region of the model indicates one unit cell of ENG MTM TL. L_R and C_R are the inherent distributed inductance and capacitance for the traditional Right Handed (RH) TL, L_{Lv} is the shunt inductance provided by the grounded via and G is the conductance. The equivalent circuit parameters which are extracted from the simulation data for the unit cell (in Fig. 2) are: C_0=0.0124pF, L_R=78.75nH, G=1/(1.64×10^6)S, L_{Lv}=0.92nH, C_R=1.06pF and Z_{in}=50Ω, respectively. The zeroth-order resonance frequency of $f_0=1/(2\pi\sqrt{L_L C_R})$ is related to the size of rectangular patch and the length of via, which determine the values of C_R and L_L [28], respectively. Moreover, according to our simulation, it was found that the ground size has significant impact on the antenna radiation characteristics; especially the gain performance.

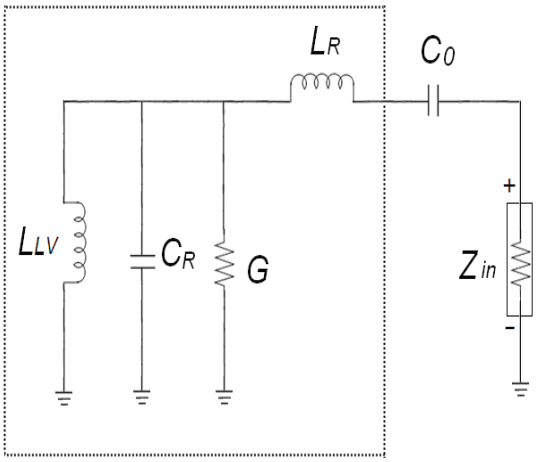

Fig. 3. Topology of the equivalent circuit for the traditional ENG ZOR antenna.

III. EVOLVED ENG ZOR ANTENNA DESIGN

A. Parasitic patch loading technology

As the first step for the evolution of traditional ENG ZOR antenna, we resort to loading a parasitic patch near the radiating one. Figure 4 illustrates the design of ENG ZOR antenna. The other parameters keep the same as the traditional ENG ZOR antenna (shown in Fig. 1). In the design, the meander line and parasitic patch are, respectively, added to accomplish shunt inductance and virtual ground capacitance [34].

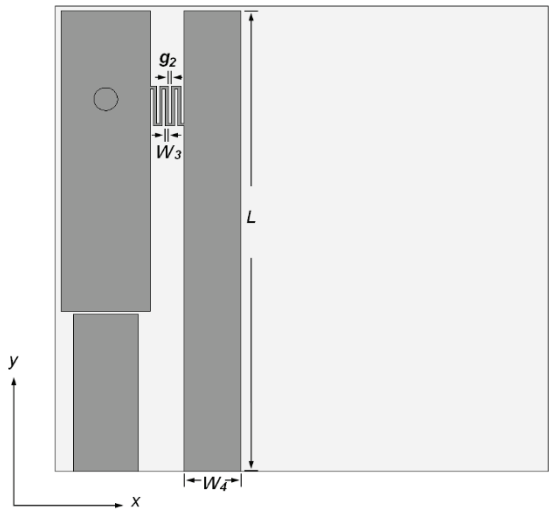

(a)

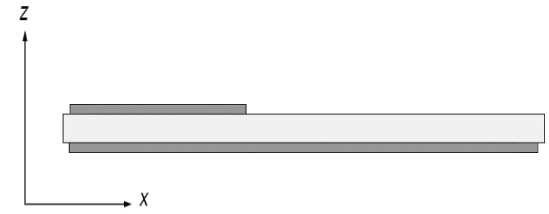

(b)

Fig. 4. ENG ZOR antenna loaded with virtual ground: (a) front view and (b) side view. The dimensions in mm are: L=16.08, g_2=0.1, W_3=0.1 and W_4=0.2.

Here, the influence of the parasitic patch on the ZOR frequency has been numerically investigated, shown in Fig. 5. By changing the width of parasitic patch (W_4), the operational frequency bandwidth, the resonance frequency position, the resonance strength of ENG ZOR antenna changed accordingly. Obviously, when the width goes larger, the ZOR operational frequency would shift lower. The reason is that the virtual ground capacitance is directly influenced by the position and dimension of parasitic patch [34]. Based on this principle, when the width alters from 2 mm to the maximum 12.06 mm, the virtual ground capacitance goes larger, further leading ZOR operational frequency

to decrease from 1.9090 GHz to 0.9807 GHz. Meanwhile, its radiation impedance also varies with W_4, making the antenna not match well with the characteristic impedance 50 Ω (especially when W_4=12.06 mm), since the antenna is fed using capacitively coupling technology. Therefore, adjusting the gap width (i.e., coupling capacitance C_0) between radiation patch and feed line, (g_1) is implemented for accommodation.

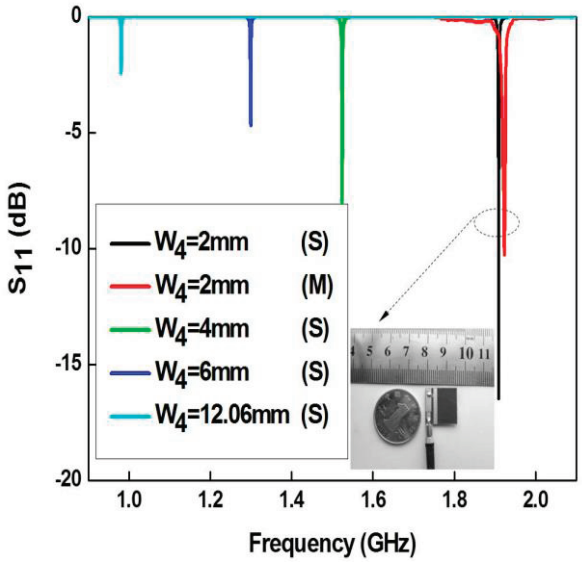

Fig. 5. Simulated and measured reflection coefficients of ENG ZOR antennas with virtual ground (notation "S" and "M" indicate the simulated and measured results, respectively.)

And then, in order to validate the simulation results, the measurement (when W_4=2 mm) is also carried out using AV3618 Vector Network Analyzer (VNA). As illustrated in Fig. 5, the measured results are generally in agreement with the simulation with an acceptable operational frequency drift (only 0.73% higher shifting). Meanwhile, the simulated and measured peak realized gains witness 0.91 dB difference, shown in Table 1. Also, it could be concluded from simulation results summarized in Table 1 that when the ZOR operational frequency decreases, the Q increases accordingly, which would result in a certain decrease of the antenna peak realized gain.

Table 1: Influence of width of parasitic patch on ZOR operating frequency and peak gain

Width of Parasitic Patch W_4 (mm)	ZOR Operating Frequency (GHz)	The Corresponding Electric Length ($\lambda_0\times\lambda_0\times\lambda_0$)	Peak Gain (dBi)
2	1.9090 (S) 1.92 (M)	0.1028×0.1028×0.00509 (S) 0.1036×0.1036×0.00513 (M)	-7.32 (S) -8.23 (M)
4	1.5324	0.0825×0.0825×0.00409	-9.4358
6	1.2989	0.0699×0.0699×0.00346	-10.90
12.06	0.9807	0.0528×0.0528×0.00262	

B. Meander line loading technology

Usually, meander-line designs were applied to produce both capacitance and inductance for wire antennas, which enable the antennas with much smaller electrical size [35-37]. At this step, the technique of etching periodic slots to design meander line on the ground is carried out to accomplish the ENG ZOR antenna further miniaturization. Figure 6 shows the evolved antenna design. As was already demonstrated in Table 1, the maximum width of parasitic patch (W_4=12.06 mm) is selected to reach the lowest frequency, ensured by virtual ground capacitance. Here, the periodic thin meander line is constructed vertically below the parasitic patch in order to obtain the additional inductance and capacitance, hoping for further miniaturization.

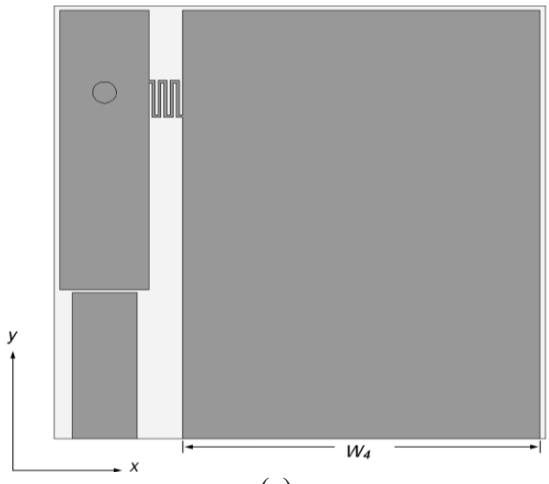

(a)

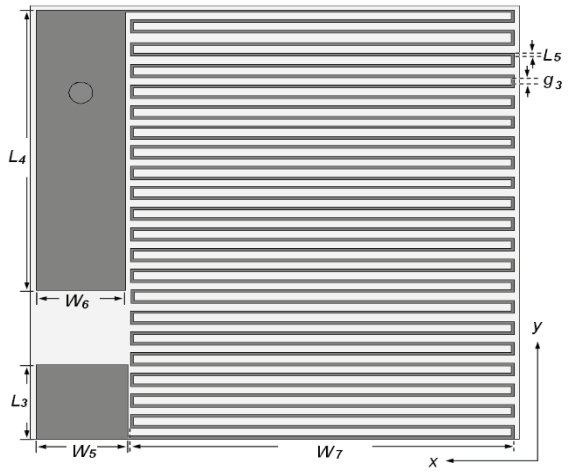

(b)

Fig. 6. The ENG ZOR antenna etched with meander line: (a) front view with the dimensions: W_4=12.06 mm and (b) back view with the dimensions in mm: L_3=2.8, W_5=3.09, L_4=10.05, W_6=3, L_5= 0.1, g_3=0.28 and W_7=12.94.

The simulation results from HFSS are described in Fig. 7. From this result, it is obvious that the operational frequency of proposed ENG ZOR antenna is successfully lowered from 980.7200 MHz to 177.8685 MHz with good impedance matching (S_{11}=-26.55 dB). Meanwhile, the peak realized gain drops (with the maximum -29.97 dBi at the operational frequency center). It is reasonable that the ZOR operational frequency is lowered dramatically at the expense of narrow bandwidth and low gain [37].

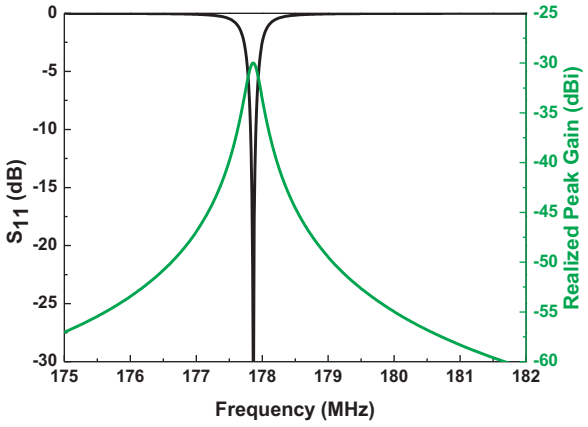

Fig. 7. Simulated reflection coefficients and peak gain of ENG ZOR antennas with meander line.

In order to further investigate the radiation performance, the HFSS simulated gain patterns in the far field are shown in Fig. 8. Generally, the pattern resembles that of a monopole; nearly omni-directional in the *Z-X* plane and bi-directional in the *Z -Y* plane.

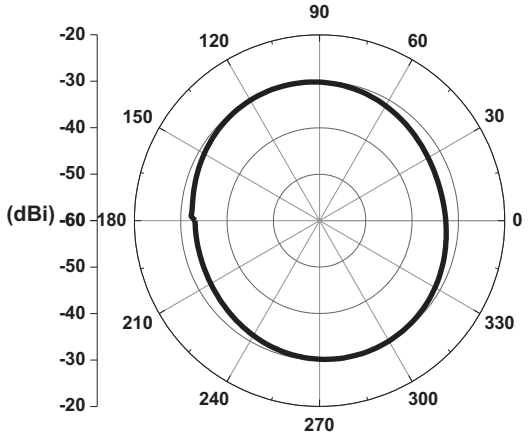

(a)

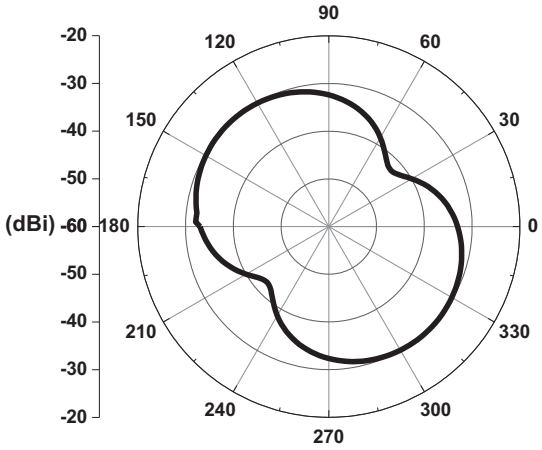

(b)

Fig. 8. Simulated gain pattern of ENG ZOR antennas with meander line at lowest operational frequency center 177.8685 MHz: (a) in *Z-X* plane and (b) in *Z-Y* plane.

Furthermore, the effect of meander line (at the bottom of the substrate) has been analyzed in Fig. 9. When the antenna operates at ZOR frequency, the majority of current concentrates on the meander line, indicating its significant contribution on radiation performances. In details, two amplified current distribution images

(I) and (II) were presented to explain the physical mechanism of Figs. 7 and 8. From the middle part in image (I), the transverse currents polarized along the *x*-direction on the meander line. On the whole, as their effect on the far-field radiation pattern can be counteracted, due to the opposite-phase polarizations of the nearby sections, it would give little contribution to the far-field radiation power [36, 37]. Meanwhile, at the edge of meander line in image (II), the currents on the sections, which are in parallel with *y*-direction, exhibit the almost in-phase polarizations of nearby sections along the *y*-direction [37]. Likewise, the sum of all of the sections (in the *y*-direction) act as a continuous line source located along *y*-direction, which thus, contribute bi-directionally in the *Z-Y* plane and nearly omni-directional radiation pattern in the *Z-X* plane. Above analysis of the phenomenon presents the reason for the simulation results in Fig. 8.

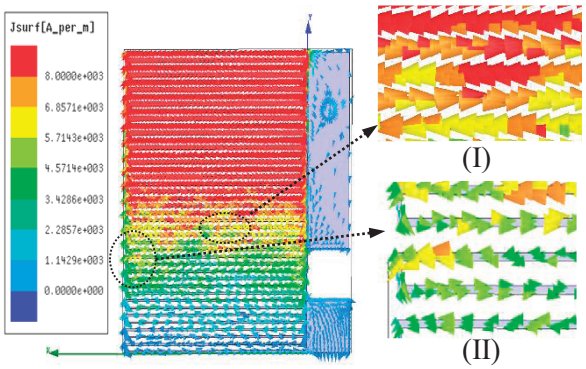

Fig. 9. Current distributions on the meander line of the evolved ENG ZOR antennas.

In the same way as Fig. 3, a topology of equivalent circuit model for the evolved ENG ZOR is shown in Fig. 10. In the similar behavior, C_0' indicates the coupling capacitance between patch and feed line in the model, the part in the dot region of the model presents one unit cell of evolved ENG MTL transmission line; L_R' and C_R' are the distributed inductance (including meander-line inductance) and capacitance (including meander-line capacitance and the capacitance between meander-line and parasitic patch) for the traditional Right Handed (RH) TL, L_{LV}' is the shunt inductance provided by the grounded via and G' is the radiation conductance. Moreover, L_{Lg} and C_g represent the shunt inductance provided by the meander line in the middle of two patches and the capacitance provided by virtual ground, respectively. Finally, the equivalent circuit parameters extracted from the simulation data of the unit cell (in Fig. 6) are: C_0'=0.0124pF, L_R'=64591.4nH, L_{LV}'=373.31nH, C_R'=63.56pF, L_{Lg}=39.7176nH, C_g=34.377pF, G'=1/(6.62×10^8)S and z_{in}=50Ω, respectively.

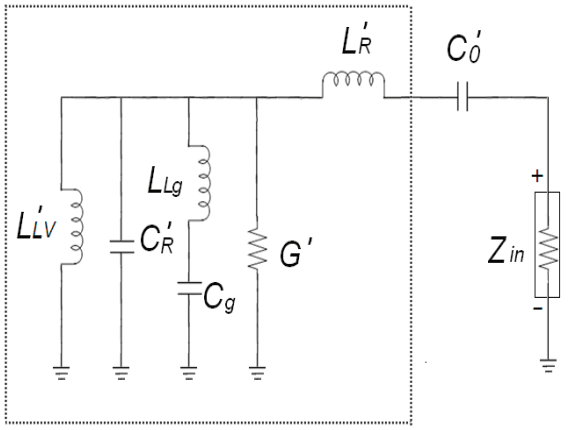

Fig. 10. The equivalent circuit model for the evolved ENG ZOR antenna.

Based on literatures [28, 34], the corresponding ZOR frequency of our proposed antenna is determined by the following equation:

$$f_0' = \frac{1}{2\pi}\sqrt{\left[\left(\frac{L_{Lv}L_{Lg}}{L_{Lv}+L_{Lg}}\right)C_R\right]^{-1}+\left[\left(\frac{L_{Lv}L_{Lg}}{L_{Lv}+L_{Lg}}\right)C_g\right]^{-1}} \quad (1)$$

From equation (1) and above analysis for each component parameters, it can be concluded that f_0' is related to the sizes of radiating and parasitic patches, the dimensions of meander lines and the length of via. In other words, while the overall dimensions of the antenna remain the same, the position of f_0' could be easily adjusted in a very large frequency region (from 177.8685 MHz to 5.084 GHz) by changing certain components in suitable dimensions.

IV. MEASUREMENT

Furthermore, the miniaturized antenna has been constructed and fabricated and the

measurement has been implemented to validate the simulation and equivalent circuit results, as shown in Fig. 11. Figure 12 shows the measured reflection coefficient of evolved ENG ZOR antenna. Obviously, the measured ZOR antenna operates at 179.48 MHz that is a little higher (~ 2 MHz shift) than that of simulation and also shows a good impedance match (S_{11}=-14.75 dB). It deserves to mention that these considerable discrepancies for such miniature antenna could be tolerable as well [12]. In addition, we note that since the peak gain of this type antenna is quite low (~-30 dBi), the Signal to Noise Ratio (SNR) in the measurement carried out in our current anechoic chamber should be very low, which the measurement setup could not reflect its radiation performance characteristics accurately. Thus, the measured radiation performances of proposed antenna were not reported here.

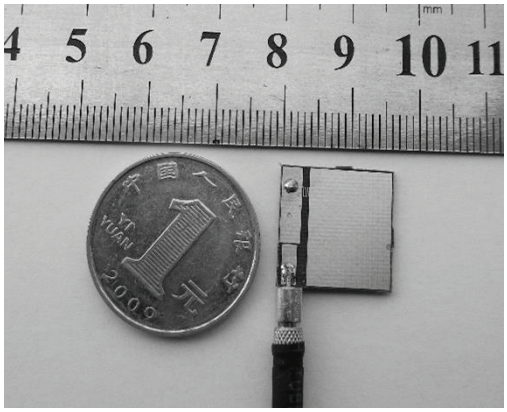

(a)

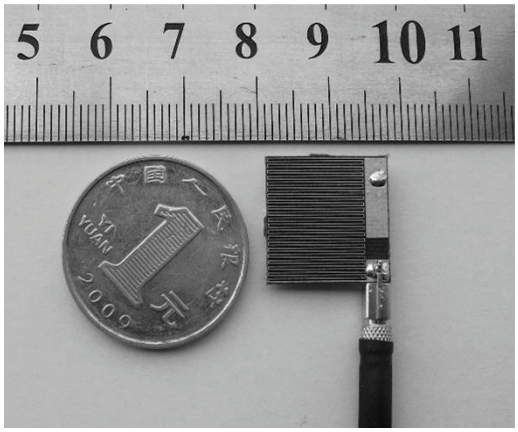

(b)

Fig. 11. Photograph of the fabricated evolved ENG ZOR antenna: (a) front view and (b) back view.

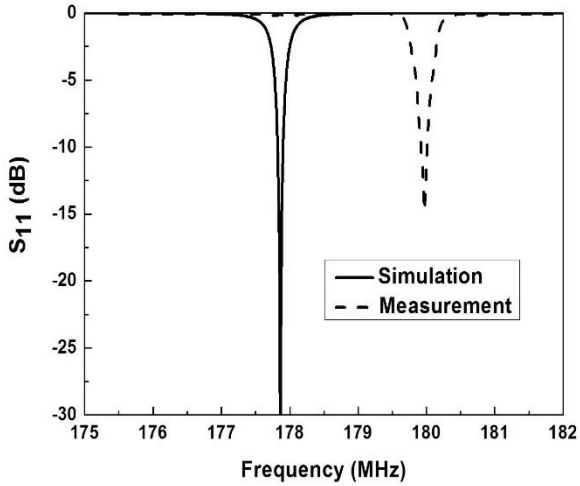

Fig. 12. Measured and simulated reflection coefficients of evolved ENG ZOR antenna.

V. CONCLUSION

An evolved ENG ZOR patch antenna with miniaturized size and ultra-low profile is proposed in this paper. With the aid of equivalent circuit models, the ZOR operational frequency could drop from 5.084 GHz to 177.8685 MHz by modifying an ordinary ENG ZOR by steps. The radiation performance with miniaturized size enables it applicable for the specified low-power radio applications, such as short range remote control system, household security system and so on. As a future work, benefiting from so wide tunable frequency range for such miniature antenna design, DC-bias diode is planned to be implemented into such antenna design to obtain wideband frequency-agile function [38] and the possibility is now under consideration.

ACKNOWLEDGMENT

This work was supported by the Fundamental Research Foundation for the Central Universities (Grant No. CDJZR12165501) and by Natural Science Foundation of Chongqing, China (Grant No. CSTC2013JJB40005).

REFERENCES

[1] H. A. Wheeler, "Fundamental limitations of small antennas," *Proc. IRE*, vol. 35, pp. 1479-1484, 1947.

[2] L. J. Chu, "Physical limitation on omni-directional antennas," *J. Appl. Phys.*, vol. 19, pp. 1163-1175, 1948.

[3] E. E. Altshuler, "Electrically small self-resonant wire antennas optimized using a genetic algorithm," *IEEE Trans. Antennas Propag*., vol. 50, pp. 297-300, 2002.

[4] H. Choo and H. Ling, "Design of electrically small planar antennas using inductively coupled feed," *Electron. Lett.*, vol. 39, pp. 1563-1565, 2003.

[5] S. Kashihara and F. Kuroki, "Bilaterally-etched cross meander-line as an electrically-small antenna at VHF band," *In Proc. China-Japan Joint Micro. Conf.*, Shanghai, China, pp. 144-146, September 2008.

[6] T. Terada, K. Ide, K. Iwata, and T. Fukusako, "Design of a small, low-profile print antenna using a Peano line," *Microw. Opt. Technol. Lett.*, vol. 51, pp. 1833-1838, 2009.

[7] R. Azadegan and K. Sarabandi, "A novel approach for miniaturization of slot antennas," *IEEE Trans. Antennas Propag.*, vol. 51, pp. 421-429, 2003.

[8] K. Sarabandi and R. Azadegan, "Design of an efficient miniaturized UHF planar antenna," *IEEE Trans. Antennas Propag.*, vol. 51, pp. 1270-1276, 2003.

[9] N. Behdad and K. Sarabandi, "Bandwidth enhancement and further size reduction of a class of miniaturized slot antennas," *IEEE Trans. Antennas Propag.*, vol. 52, pp. 1928-1935, 2004.

[10] Y. Tikhov, Y. Kim, and Y. H. Min, "Planar radiator with refined slot pattern for electrically small antennas," *IEEE Proc. Microw. Antennas Propag.*, vol. 153, pp. 19-24, 2006.

[11] K. V. Caekenberghe, N. Behdad, K. M. Brakora, and K. Sarabandi, "A 2.45-GHz electrically small slot antenna," *IEEE Antennas Wireless Propag. Lett.*, vol. 7, pp. 346-348, 2008.

[12] W. Hong and K. Sarabandi, "Low profile miniaturized planar antenna with omnidirectional vertically polarized radiation," *IEEE Trans. Antennas Propag.*, vol. 56, pp. 1533-1540, 2008.

[13] H. R. Stuart and A. Pidwerbetsky, "Electrically small antenna elements using negative permittivity resonators," *IEEE Trans. Antennas Propag.*, vol. 54, pp. 1644-1653, 2006.

[14] R. W. Ziolkowski and A. Erentok "Metamaterial-based efficient electrically small antennas," *IEEE Trans. Antennas Propag.*, vol. 54, pp. 2113-2130, 2006.

[15] S. Ghadarghadr, A. Ahmadi, and H. Mosallaei, "Negative permeability-based electrically small antennas," *IEEE Antennas Wireless Propag. Lett.*, vol. 7, pp. 13-17, 2008.

[16] C. C. Lin, R. W. Ziolkowski, J. A. Nielsen, M. H. Tanielian, and C. L. Holloway, "An efficient, low profile, electrically small, three-dimensional, very high frequency magnetic EZ antenna," *Appl. Phys. Lett*., vol. 96, pp. 104102 (1-3), March 2010.

[17] K. Z. Rajab, R. Mittra, and M. T. Lanagan, "Size reduction of microstrip patch antennas with left-handed transmission line loading," *IET Microw. Antennas Propag.*, vol. 1, pp. 39-44, 2007.

[18] K. Y. Hui and K. M. Luk, "A miniature dielectric resonator loaded patch antenna," *IEEE Trans. Antennas Propag.*, vol. 53, pp. 2118-2122, 2005.

[19] K. D. Jang, J. H. Kim, D. H. Lee, G. H. Kim, W. M. Seong, and W. S. Park, "A small CRLH-TL metamaterial antenna with a magneto-dielectric material," *IEEE AP-S Int. Antennas Propag. Symp. Dig.*, San Diego, USA, pp. 1-4, 2008.

[20] M. E. Emutlu, C. R. Simovski, M. K. Kärkkäinen, P. Ikonen, S. A. Tretyakov, and A. A. Sochava, "Miniaturization of patch antennas with new artificial magnetic layers," *Antenna Technology: Small Antennas and Novel Metamaterials, 2005. IWAT 2005. IEEE International Workshop*, pp. 87-90, March 2005.

[21] P. Y. Chen and A. Alù, "Sub-wavelength elliptical patch antenna loaded with μ-negative metamaterials," *IEEE Trans. Antennas Propag.*, vol. 58, pp. 2909-2919, 2010.

[22] M. Li, X. Q. Lin, J. Y. Chin, R. Liu, and T. J. Cui, "A novel miniaturized printed planar antenna using split-ring resonator," *IEEE Antennas Wireless Propag. Lett.*, vol. 7, pp. 629-631, 2008.

[23] Y. Kim, J. Kim, J. Kim, H. Kim, and H. Lee, "Negative permeability metamaterial structure based electrically small loop antenna," *Advanced Communication Technology, 2008. ICACT 2008. 10th International Conference*, Phoenix Park, Korea, pp. 769-773, 2008.

[24] A. Lai, K. M. K. H. Leong, and T. Itoh, "Infinite wavelength resonant antennas with monopolar radiation pattern based on periodic structures," *IEEE Trans. Antennas Propag.*, vol. 55, pp. 868-876, 2007.

[25] S. Pyo, S.-M. Han, J. W. Baik, and Y. S. Kim, "A slot-loaded composite right/left-handed transmission line for a zeroth-order resonant antenna with improved efficiency," *IEEE Trans. Microw. Theory Tech.*, vol. 57, pp. 2775-2782, 2009.

[26] Y. Dong and T. Itoh, "Miniaturized substrate integrated waveguide slot antennas based on negative order resonance," *IEEE Trans. Antennas Propag.*, vol. 58, pp. 3856-3864, 2010.

[27] S. W. Lee and J. H. Lee, "Electrically small MNG ZOR antenna with multilayered conductor," *IEEE Antennas Wireless Propag. Lett.*, vol. 9, pp. 724-727, 2010.

[28] J. H. Park, Y. H. Ryu, J. G. Lee, and J. H. Lee,

"Epsilon negative zeroth-order resonator antenna," *IEEE Trans. Antennas Propag.*, vol. 55, pp. 3710-3712, 2007.

[29] W. C. Chang and B. Lee, "Wideband one-unit-cell ENG zeroth-order resonant antenna," *Electron. Lett.*, vol. 45, pp. 1289-1291, 2009.

[30] S. Jang and B. Lee, "Meta-structured one-unit-cell epsilon negative antenna," *Microw. Opt. Technol. Lett.*, vol. 51, pp. 2991-2994, 2009.

[31] J. Kim, G. Kim, W. Seong, and J. Choi, "A tunable internal antenna with an epsilon negative zeroth order resonator for DVB-H service," *IEEE Trans. Antennas Propag.*, vol. 57, pp. 4014-4017, 2009.

[32] J. Q. Huang and Q. X. Chu, "Small ZOR antenna with high efficiency based on epsilon negative transmission line," *2010 IEEE Microwave and Millimeter Wave Technology (ICMMT), 2010 International Conference*, Chengdu, China, pp. 1905-1907, 2010.

[33] "Ansoft high frequency structure simulation (HFSS)," ver. 10, *Ansoft Corp*., 2005.

[34] A. Sanada, M. Kimura, I. Awai, C. Caloz, and T. Itoh, "A planar zeroth-order resonator antenna using a left-handed transmission line," *In Proc. Eur. Microwave Conf.*, pp. 1341-1344, 2004.

[35] J. Rashed and C. T. Tai, "A new class of resonant antennas," *IEEE Trans. Antennas Propag.*, vol. 39, pp. 1428-1430, 1991.

[36] T. J. Warnagiris and T. J. Minardo, "Performance of a meandered line as electrically small transmitting antenna," *IEEE Trans. Antennas Propag.*, vol. 46, pp. 1797-1876, 1998.

[37] G. Marrocco, "Gain-optimized self-resonant meander line antennas for RFID applications," *IEEE Antennas Wireless Propag. Lett.*, vol. 2, pp. 302-305, 2003.

[38] M. C. Tang and R. W. Ziolkowski, "A frequency agile, ultralow-profile, complementary split ring resonator-based electrically small antenna," *Microw. Opt. Technol. Lett.*, vol. 55, pp. 2425-2428, 2013.

Microstrip Low-Pass Filter with Sharp Roll-Off Using Transformed Radial Stubs

Mohsen Hayati, Hossein Shahbazitabar, and Gelareh Hajian

Electrical Engineering Department
Islamic Azad University, Faculty of Engineering, Kermanshah Branch, Kermanshah, Iran
mohsen_hayati@yahoo.com

Abstract ─ A novel microstrip low-pass filter with good characteristics, such as sharp roll-off, wide stop-band, low insertion loss and good return loss is presented. The proposed filter with a 3 dB cut off frequency at 1.19 GHz, roll-off rate equal to 218 dB/GHz and a relative stop-band bandwidth of 163.5% (referred to a suppression level of -20 dB) is designed, fabricated and measured, achieving a highest figure of meritequal to 77228. There is good agreement between the simulation and measurement results.

Index Terms - Figure of merit, insertion loss, microstrip low-pass filter, return loss and roll-off rate.

I. INTRODUCTION

High performance and compact size low-pass filters are in high demand for many wireless applications, to eliminate spurious signals. Printed circuit board filters are most popular because of their easy realization, low cost and simple integration with other microwave circuits. Conventional low-pass filters using shunt stubs or high-low impedance transmission lines [1], have been widely used in microwave systems for their excellent characteristics. However, compact size and good performance are hard to achieve simultaneously. Thus, many techniques to achieve both size reduction and the other performance enhancements have been studied [2-12]. A microstrip low-pass filter symmetrically loaded with triangular and high-low impedance [2] and a low-pass filter, based on the main transmission line with radial patches [3] have been achieved to have sharp roll-off and a wide stop-band, but the size is large. In [4], both radial-shape patches and interdigital construction have been used to obtain compact size and wide stop-band, but the skirt characteristic was not sharp enough. Transformed radial stub cells have enhanced the compactness and enabled controllable transmission zeros in [5], but its frequency response has gradual transition band. In [6], a sharp rejection band using a Slit-Loaded Tapered Compact Microstrip Resonator Cell (SLTCMRC) has been presented. Disadvantages of the mentioned resonator are large size and low return loss. A microstrip low-pass filter using resonant patches and a meander transmission line has been presented in [7]; which results in a good pass-band performance, but the stop-band performance is not good. A microstrip low-pass filter with wide stop-band using an embedded band-stop structure has been presented in [8], but this filter suffers from a gradual transition band. A compact microstrip low-pass filter with compact size and simple structure based on the coupled-line hairpin unit has been designed in [9], but it doesn't have a sharp roll off. In [10] and [11] the Defected Ground Structure (DGS) has been designed, which results in a wide stop-band. In [12], a compact microstrip low-pass filter with wide stop-band using Open Stubs-Loaded Spiral Compact Microstrip Resonant Cell (OSLSCMRC) has been presented, but it has gradual response.

In this paper, a novel microstrip low-pass filter with good features such as compact size, sharp roll-off and wide stop-band is proposed as follows: design of a resonator using transformed radial stubs to obtain a sharp roll-off, design of a suppressing cell consisting of semicircles and open stubs to obtain a wide stop-band and the suppressing cell is added to the proposed resonator to have both wide stop-band and sharp roll-off.

Submitted On: May 5, 2013
Accepted On: April 20, 2014

The proposed filter is designed, fabricated and measured. The results indicate the 3 dB cut off frequency at 1.19 GHz, the 20 dB stop-band bandwidth equal to 11.8 GHz (from 1.325 GHz to 13.125 GHz), low insertion loss and good return loss.

II. PROPOSED RESONATOR AND ITS CHARACTERISTICS

Figure 1 shows the proposed resonator, which consists of 8 transformed radial stubs and high impedance strip lines as a connector between the transformed radial stubs. The dimensions of the proposed resonator are: W_i=0.6, W_1=0.1, d_1=4, d_2=1.36, d_3=1.2, d_4=1.5, d_5=2.5, d_6=5.2, d_7=5.5, d_8=5.8 and d_9=11.3; all in mm and θ=70 in degree.

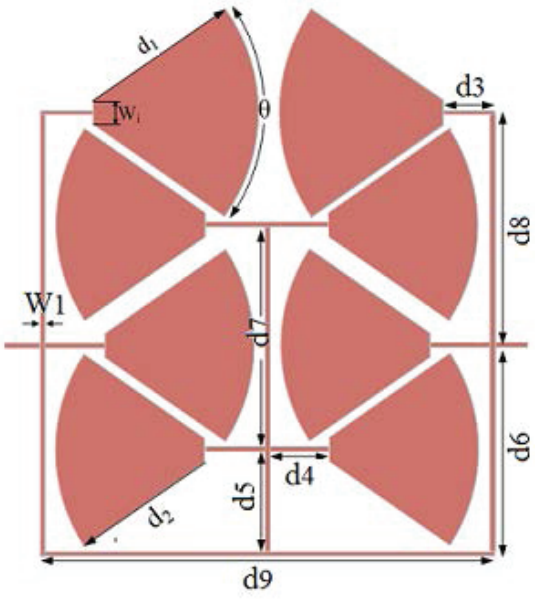

Fig. 1. The proposed resonator.

The simulated result of the proposed resonator is illustrated in Fig. 2. The obtained 3 dB cut off frequency is 1.19 GHz, the transition band from 3 to 20 dB is 0.15 GHz and the insertion loss from DC to 1.12 GHz is less than 1 dB. Transmission zeros are located at 1.39, 2.07, 2.98, 3.75 and 5.4 GHz with the attenuation level of -40.3, -49.32, -49.45, -59.56 and -60.43 dB, respectively. It is obvious that the sharp roll-off (equal to187.71%) is achieved, but the stop-band characteristics are not good.

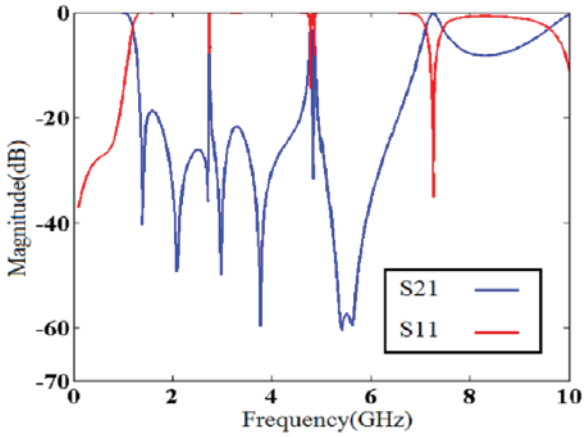

Fig. 2. The simulated S-parameters of the proposed resonator.

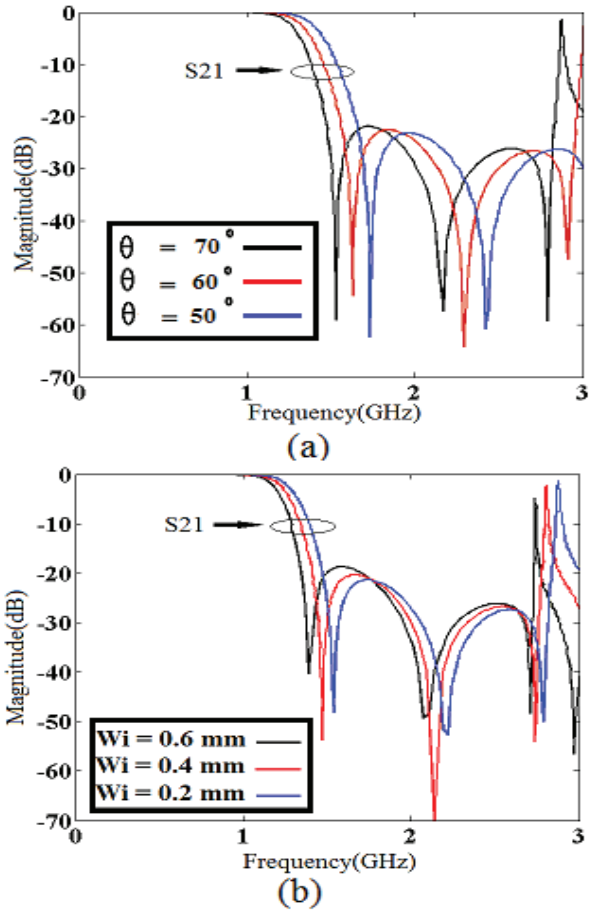

Fig. 3. (a) Simulated S-parameter of the proposed resonator as a function of θ and (b) simulated S-parameter of the proposed resonator as a function of W_i.

The simulated S-parameters of the proposed resonator as functions of θ and W_i are shown in Figs. 3 (a) and (b), respectively. Figure 3 (a) shows when θ increases from 50° to 70°, transmission zeros move to lower frequencies. Similarly, in Fig. 3 (b), by decreasing W_i from 0.6 mm to 0.2 mm, the transmission zeros move away from lower frequencies. Hence, the location of the transmission zeros can be controlled by these parameters.

III. SUPPRESSING CELL

To obtain both wide stop-band and sharp roll-off, a semicircular structure is added to the proposed resonator. Also, to achieve better suppression, an open stub is added to the semicircular structure that creates an attenuation pole at 0.9 GHz. Figure 4 shows the proposed suppressing cell consists of the semicircular structure and the open stub. Dimensions of the proposed suppressing cell are: W_2=0.4, d_{10}=2, R=3.4, d_{11}=8.4, d_{12}=9 and W_3=0.75; all in mm.

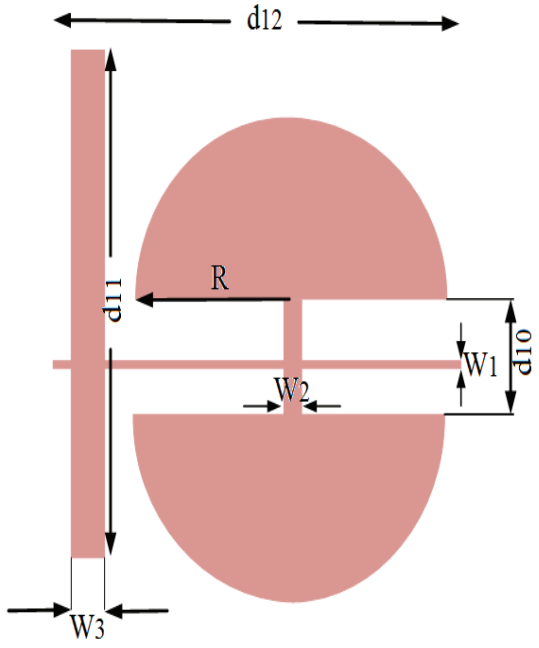

Fig. 4. The proposed suppressing cell.

Figure 5 shows the simulated S-parameters of the proposed suppressing cell. As can be seen, the suppressing cell has a cut off frequency at 1.9 GHz and a wide stop-band from 5.35 GHz to 21.5 GHz.

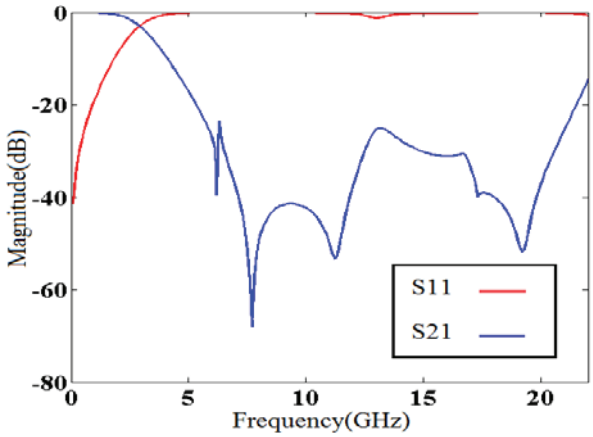

Fig. 5. Simulated S-parameters of the suppressing cell.

IV. FILTER DESIGN AND DISCUSSION

To obtain a filter with sharp rejection band and wide stop-band, the suppressing cell is added to the proposed resonator. The layout of the proposed filter is shown in Fig. 6. The width and length of the feeding line for 50Ω matching are W=1.16 mm and L=2 mm, respectively. The proposed filter has been fabricated on the RT/Duroid 5880 substrate with dielectric constant of ε_r=2.2, thickness of 15 mil and a loss tangent of 0.0009. Simulation is accomplished using an EM-simulator ADS and measurement is carried out using a HP8757A vector network analyzer.

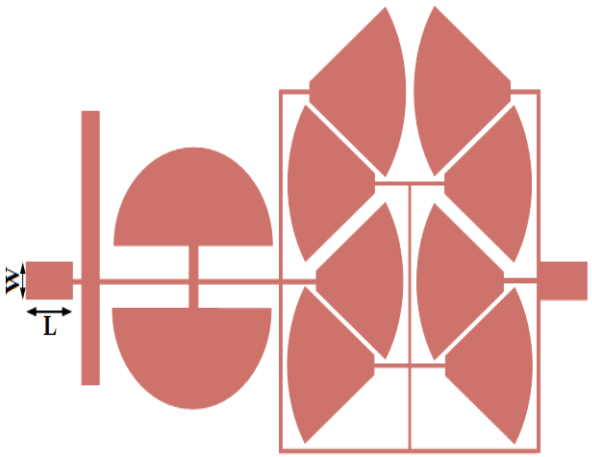

Fig. 6. The proposed filter.

Figure 7 illustrates the simulated and measured S-parameters, which are in good

agreement. The measured specifications of the proposed filter are sharp roll-off, low insertion loss, good return loss, compact size and wide stop-band up to 10.8 *fc*, with size of about 20.3×13.2 mm^2 (0.118λg×0.078λg, where λg is the guided wavelength at 3 dB cut off frequency).

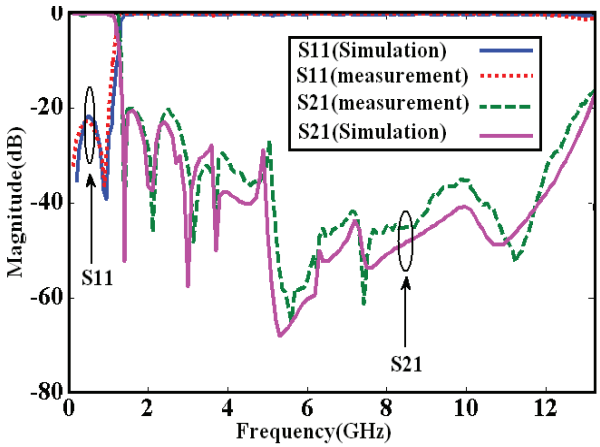

Fig. 7. The simulated and measured S-parameters of the proposed LPF.

The photograph of the fabricated filter is shown in Fig. 8.

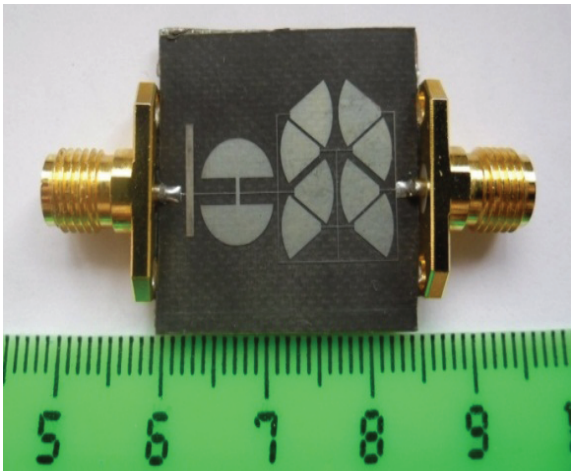

Fig. 8. Photograph of the fabricated filter.

A comparison with other LPFs is given in Table 1, which shows that the proposed filter has good characteristics with compact size.

Table 1: Comparisons between the proposed filter and other works

Reference	f_c	RSB	SF	NCS	AF	ζ	FOM
[2]	1.5	1.57	1.5	0.108×0.145	1	257	38747
[3]	2.4	1.36	3	0.351×0.106	1	93	10106
[4]	1.18	1.32	1.5	0.079×0.079	1	36	11543
[5]	3.2	1.66	2	0.12×0.063	1	10	4391
[6]	1.78	1.41	1	0.25×0.19	1	168	4985
[7]	1.3	1.52	1.7	0.12×0.071	1	37	11221
[10]	2.95	1.46	2	0.43×0.27	2	25	315
[11]	3.4	1.4	2	0.25×0.16	2	37	350
This work	1.19	1.63	2	0.118×0.078	1	218	77228

In Table 1, the roll-off rate ζ is given by:

$$\zeta = \frac{\alpha max - \alpha min}{f_s - f_c}(dB / GHz), \quad (1)$$

where $\alpha_{\max}$ is the 40 dB attenuation point, $\alpha_{\min}$ is the 3 dB attenuation point, f_s is the 40 dB stop-band frequency and f_c is the 3 dB cut off frequency.

The Relative Stop-Band Bandwidth (RSB) is defined as:

$$RSB = \frac{Stopband\ \ bandwidth\ (-20\ dB)}{Stopband\ \ center\ \ frequency}. \quad (2)$$

The Suppression Factor (SF) is based on the stop-band suppression. A higher suppression leads to a greater SF.

$$SF = \frac{Attenuation\ \ level}{10}. \quad (3)$$

The Normalized Circuit Size (NCS) is given

by:

$$NCS = \frac{Physical\ \ size\,(length \times width)}{\frac{2}{\lambda g}}, \qquad (4)$$

where λ_g is the guided wavelength at 3 dB cut off frequency.

The Architecture Factor (AF) can be recognised as the circuit complexity factor, which is defined as 1 and 2 when the design is 2D or 3D, respectively.

Finally, the Figure-of-Merit (FOM), which is the overall index of a proposed filter, is defined as:

$$FOM = \frac{\zeta \times RSB \times SF}{NCS \times AF}. \qquad (5)$$

It can be seen from Table 1 that the proposed filter exhibits the highest figure of merit equal to 77228, among the quoted filters.

V. CONCLUSION

A novel microstrip low-pass filter consisting of the transformed radial stubs, semicircular units and open stubs has been presented. The proposed filter has 3 dB cut off frequency at 1.19 GHz and roll-off rate equal to 218 dB/GHz. The insertion loss from DC to 1.15 GHz is less than 0.3 dB, the relative stop-band bandwidth with 20 dB attenuation level is 1.63 GHz (from 1.32 GHz to 13.12 GHz) and the return loss in the stop-band region is close to 0 dB, indicating negligible radiation loss.

ACKNOWLEDGMENT

The authors would like to thank the Islamic Azad University, Kermanshah Branch, for the financial support of this research project.

REFERENCES

[1] D. M. Pozar, "Microwave engineering," *Wiley*, New York, 2005.

[2] J. P. Wang, L. Ge, Y. X. Guo and W. Wu, "Miniaturised microstrip low-pass filter with broad stop-band and sharp roll-off," *Electronic Letters*, vol. 46, no. 8, pp. 573-575, 2010.

[3] J. L. Li, S. W. Qu, and Q. Xue, "Compact microstrip low-pass filter with sharp roll-off and wide stop-band," *Electronic Letters*, vol. 45, no. 2, pp. 110-111, 2009.

[4] J. Wang, L. J. Xu, S. Zhao, Y. X. Guo, and W. Wu, "Compact quasi-elliptic microstrip low-pass filter with wide stop-band," *Electronic Letters*, vol. 46, no. 20, pp. 1384-1385, 2010.

[5] K. Ma, K. S. Yeo, and W. M. Lim, "Ultra-wide rejection band low-pass cell," *Electronic Letters*, vol. 48, no. 2, pp. 99-100, 2012.

[6] M. Hayati and A. Lotfi, "Elliptic-function low-pass filter with sharp cutoff frequency using slit-loaded tapered compact microstrip resonator cell," *Electronic Letters*, vol. 46, no. 2, pp. 143-144, 2010.

[7] L. Ge, J. P. Wang, and Y. X. Guo, "Compact microstrip low-pass filter with ultra-wide stop-band," *Electronic Letters*, vol. 46, no. 10, pp. 689-691, 2010.

[8] Q. He and C. Liu, "A novel low-pass filter with an embedded band-stop structure for improved stop-band characteristic," *IEEE Microwave Wireless Component Letters*, vol. 19, no. 10, pp. 629-631, 2009.

[9] F. Wei, L. Chen, and X. W. Shi, "Compact low-pass filter based on coupled-line hairpin unit," *Electronic Letters*, vol. 48, no. 7, pp. 3799-3811, 2012.

[10] M. Challa, A. Boutejdar, M. Dehmas, A. Azrar, and A. S. Omar, "Compact microstrip low-pass filter design with ultra-wide reject band using a novel quarter-circle DGS shape," *Applied Computational Electromagnetics Society Journal*, vol. 27, no. 10, pp. 808-815, 2012.

[11] A. Faraghi, M. N. Azarmanesh, and M. Ojaroudi, "Small microstrip low-pass filter by using novel defected ground structure for UWB applications," *Applied Computational Electromagnetics Society Journal*, vol. 28, no. 4, pp. 341-347, 2013.

[12] A. Adinehvand and A. Lotfi, "Compact low-pass filter with wide stop-band using open stubs-loaded spiral microstrip resonant cell," *Applied Computational Electromagnetics Society Journal*, vol. 28, no. 1, pp. 27-34, 2013.

Mohsen Hayati received his B.E. degree in Electronics and Communication Engineering from Nagarjuna University, India in 1985 and the M.E. and Ph.D. degrees in Electronics Engineering from Delhi University, Delhi, India in 1987 and 1992, respectively. He joined the Electrical Engineering Department at Razi University, Kermanshah, Iran as an Assistant Professor in 1993. At present, he is an Associate Professor with the Electrical Engineering Department at Razi University. He has published more than 135 papers in international and domestic journals and conferences.

His current research interests include microwave and millimeter wave devices and circuits, application of computational intelligence, artificial neural networks, fuzzy systems, neuro-fuzzy systems, electronic circuit synthesis and modeling and simulations.

Hossein Shahbazitabar received his B.E. degree at Azad University, Tuyserkan, Iran in 2008 and his M.E. degree in Electrical Engineering in 2012 at Azad University, Tehran, Iran. His research interests include the low-power and low-size integrated circuit design and microwave and millimeter wave devices and circuits.

Gelareh Hajian received her B.E. and M.E. degrees in Electronics Engineering from Razi University, Kermanshah, Iran in 2007 and 2012, respectively. Her research interests include microwave and millimeter wave devices and solar technology and solar cells.

A Novel Compact Microstrip Low-pass Filter with a Wide Rejection-Band and Sharp Roll-Off using Star-Shaped Resonator

Mohsen Hayati, Zahra Faramarzi, and Mozhgan Amiri

Electrical Engineering Department
Islamic Azad University, Faculty of Engineering, Kermanshah Branch, Kermanshah, Iran
mohsen_hayati@yahoo.com

Abstract ─ In this paper, a novel compact microstrip Low-Pass Filter (LPF) with a wide rejection-band and sharp roll-off using a star-shaped resonator is presented. The proposed LPF provides some significant features, such as simple structure, low insertion-loss less than 0.1 dB from DC to 2.391 GHz in the pass-band and expanded stop-band with an attenuation level better than -20 dB from 2.842 GHz up to 20.65 GHz. The transition band is 0.27 GHz from 2.57 GHz to 2.84 GHz, with corresponding attenuation levels of -3 dB and -20 dB, respectively. The filter with a -3 dB cutoff frequency of 2.57 GHz has been designed, fabricated and tested, where the measurement results are in good agreement with the simulation results. The overall size of the proposed LPF is only 11.4 mm × 13.6 mm.

Index Terms – Low-pass filter, microstrip, sharp roll-off and wide rejection band.

I. INTRODUCTION

Low-Pass Filters (LPFs) are widely used in the microwave and wireless communication systems. Recently, the design of filters in the microwave applications is based on the microstrip transmission lines incorporating with the Defected Ground Structures (DGSs), or Photonic Band Gap tructures (PBG) [1]. A DGS unit is realized by etching off a simple shape defect from the ground plane that modifies the transmission line characteristics (capacitance and inductance), achieves slow-wave effect and band-stop property and causes size reduction [2-3]. PBG is done by etching a set of periodic defects in the ground plane of a microstrip structure. These PBG structures have the character of producing band gaps or stop-bands that shape the filter response. In addition, they have the property of slowing down the propagating electromagnetic waves [4]. The PBG structures require many parameters to design of the desirable filter characteristics and it is difficult to derive an equivalent circuit model, whereas DGS needs a less parameter to design and is easy to obtain and evaluate its equivalent circuit and model [1]. However, by considering the fact that the ground plane is etched, this structure does not provide the mechanical robustness against strains [5]. Also, DGS causes the electromagnetic radiations that lead to scattering power dissipations [6]. To meet the size requirement of the modern microwave circuits, several techniques have been proposed [7]. The Invasive Weed Optimization (IWO) approach has been applied to miniaturize the Step Impedance Transmission Lines (SITL) in [8], but it doesn't have sharp roll-off response and wide stop-band. To obtain ultra-wide rejection-band, triangular and polygonal patch resonators with the meander transmission line, are implemented in [9-11], but these LPFs aren't compact enough. The Stepped Impedance Low-Pass Filter (SI-LPF) using back-to-back C-shaped and triple C-shaped units in [12] is introduced. Despite having a small physical size, it suffers from a gradual transition-band. In [13], a stepped impedance LPF using hairpin resonator with radial stubs, with intrinsic wide stop-band characteristics was employed. However, its roll-off rate is unsuitable.

In this paper, by combining the star-shaped resonator with the C-shaped stubs to suppress spurious harmonics, the designed LPF not only has a compact circuit size and sharp transition-band, but also has a wide stop-band with the attenuation level better than -20 dB. In addition, it has low insertion-loss less than 0.1 dB in the pass-band. To

Submitted On: June 15, 2013
Accepted On: April 20, 2014

reduce the circuit size of the filter, the meander transmission lines are adopted in the design of the low-pass filter.

II. FILTER DESIGN

A. Resonator design

In order to obtain a sharper roll-off, it is desirable to use a resonator structure with an elliptic function response, shown in Fig. 1. The microstrip realization of the lumped L-C element is to be approximated by use of short lengths of high and low impedance lines, illustrated in Fig. 2 [14].

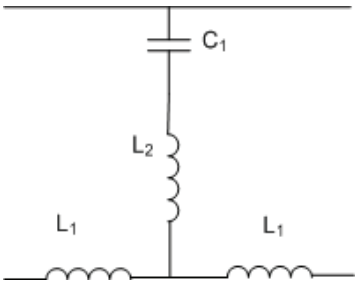

Fig. 1. A lumped element prototype low-pass resonator with an elliptic-function.

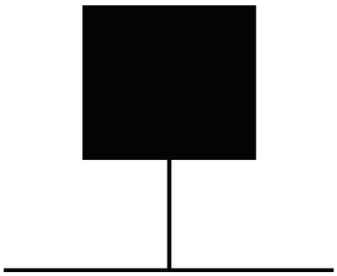

Fig. 2. Microstrip realization of the elliptic function prototype low-pass resonator.

The values of the parameters of the low and high impedance lines can be extracted using methods presented in [14]:

$$L_i = \frac{1}{2\pi f_c} Z_{oL} \sin\left(\frac{2\pi}{\lambda_{gL_i}} l_{Li}\right), \qquad (1)$$

$$C_i = \frac{1}{2\pi f_c Z_{oC}} \sin\left(\frac{2\pi}{\lambda_{gC_i}} l_{Ci}\right), \qquad (2)$$

where f_c is the cutoff frequency, λ_{gL} and λ_{gC} are the guided wavelength of high and low impedance lines at the cutoff frequency and Z_{0L} and Z_{0C} represent the characteristic impedance of high and low impedance lines, respectively. This resonator has a sharp transition band, but the return-loss and insertion loss in the pass-band are not suitable enough. To improve the performance of the structure, a star shaped resonator is proposed, as shown in Fig. 3. The simulation result of S-parameters of the star-shaped resonator is shown in Fig. 4.

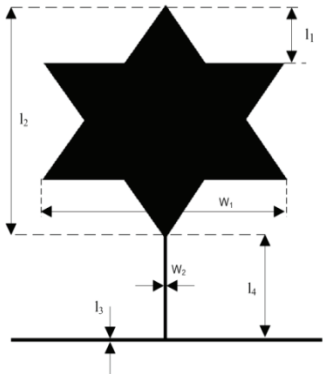

Fig. 3. Layout of the proposed star-shaped resonator.

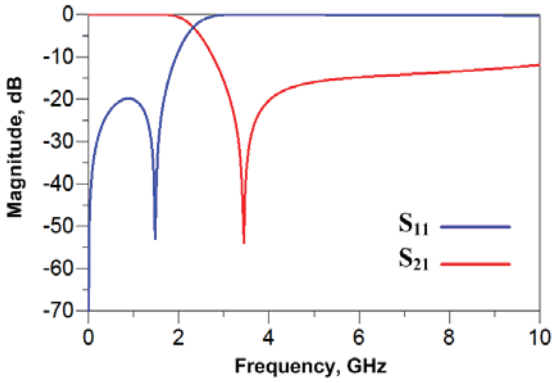

Fig. 4. S-parameters simulation of the proposed star-shaped resonator.

The accomplished comparison between frequency response of the proposed resonator and the prototype resonator shown in Fig. 5, indicates that the proposed resonator has a better pass-band response than the prototype resonator. As illustrated in Fig. 5, the star-shaped resonator has a return-loss better than -17.5 dB and an insertion-

loss better than 0.1 dB, whereas the prototype resonator has a return-loss better than -12 dB and an insertion loss better than 0.3 dB.

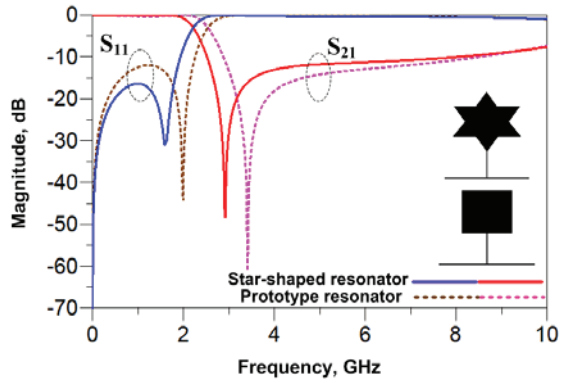

Fig. 5. Comparison between S-Parameters simulation of the prototype and proposed resonators.

As demonstrated in Fig. 6, the star-shaped resonator has a return-loss better than -17 dB in the pass-band, whereas the triangular has a return-loss better than -12 dB in the pass-band; therefore, this significant specification implies the superiority of the proposed resonator by comparison with the triangular resonator.

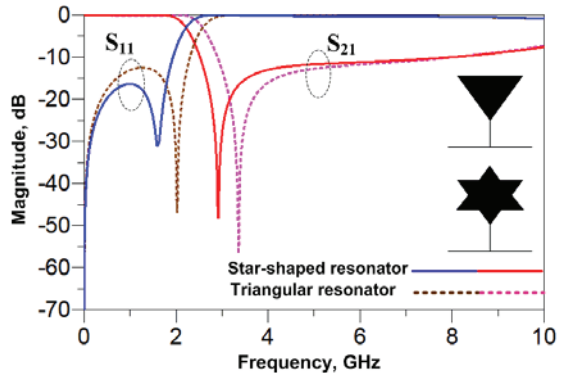

Fig. 6. Comparison between S-Parameters simulation of the triangular and proposed resonators.

Figures 7 and 8 exhibits the star-shaped resonator as a function of l_2 and l_4, respectively. In Fig. 7, by increasing l_2 from 6.1 mm to 7.1 mm, the return-loss in the pass-band becomes better from -17 dB to -21.5 dB. By decreasing l_2 from 6.1 mm to 5.1 mm, the attenuation level of the return-loss in the pass-band becomes worse from -17 dB to -13.9 dB. As illustrated in Fig. 8, due to reducing the physical size of the resonator by decreasing l_4 from 2.7 mm to 1.7 mm, the transmission zero near the pass-band changes from 2.92 GHz to 3.476 GHz, which leads to a gradual transition-band. While by increasing l_4 from 2.7 mm to 3.7 mm, the mentioned transmission zero changes from 2.92 GHz to 2.559 GHz, which results in a sharper transition-band. Therefore, these parameters are significant to optimize some attributes of the resonator.

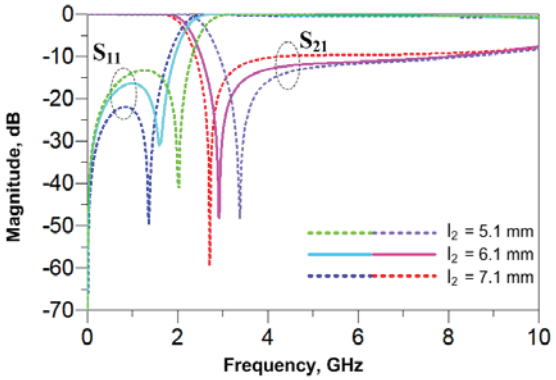

Fig. 7. S-parameters simulation of the proposed resonator as a function of l_2.

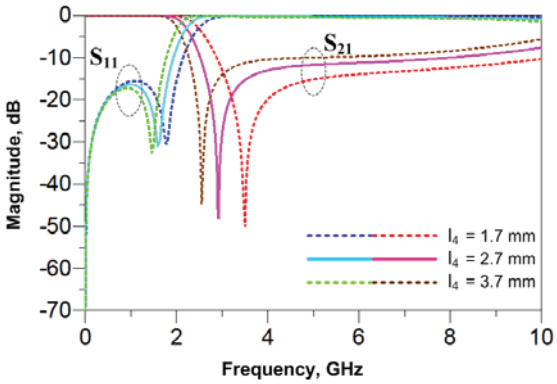

Fig. 8. S-parameters simulation of the proposed resonator as a function of l_4.

B. Filter design

To eliminate the high frequency harmonics and obtain a wider stop-band region, it is needed to add a suppressing cell to the proposed resonator. Figure 9 exhibits the layout and frequency response of two C-shaped suppressor

cells. As shown in Fig. 9, these stubs result in extra finite transmission zero within the stop-band that suppress the harmonics and also extends the stop-band. As indicated in Fig. 10, the asymmetrical C-shaped stubs have the better pass-band response due to its -50 dB return-loss, in comparison with symmetrical C-shaped stubs, which has -21 dB return-loss. Therefore, using these asymmetrical C-shaped stubs, the return-loss for the final structure of the LPF will be better.

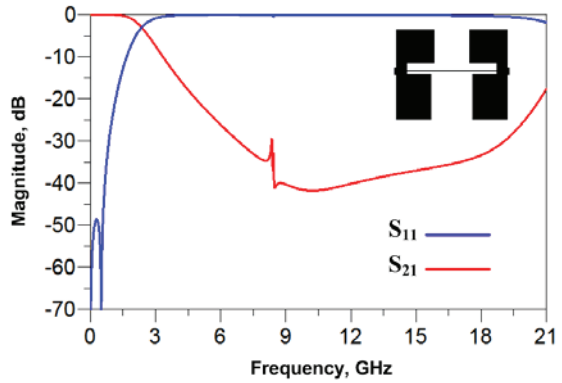

Fig. 9. Layout and S-parameter simulation of C-shaped stubs.

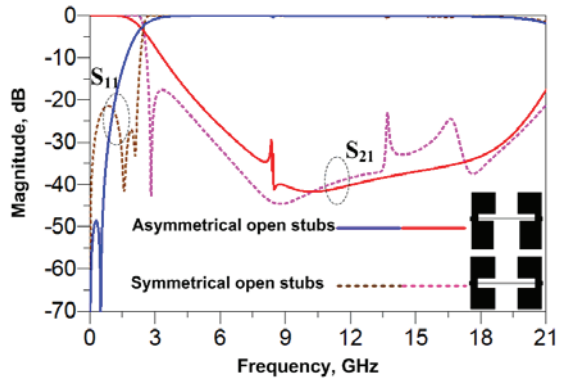

Fig. 10. Comparison between S-Parameters of the symmetrical open stubs and the C-shaped stubs.

The layout of the proposed LPF is shown in Fig. 11, in which the meander transmission lines are used to reduce the physical size of the proposed LPF. The input/output ports are matched to 50 Ω, using two stubs with dimensions of L_f=2.3 mm and W_f=1.5 mm. The dimensions of the proposed LPF are as specified in Table 1.

Table 1: Dimensions of proposed LPF (mm)

l_1=1.5	l_2=6.1	l_3=0.1	l_4=2.7
l_5=3.3	l_6=0.7	l_7=4.5	l_8=0.2
l_9=0.7	l_{10}=0.5	W_1=7	W_2=0.1
W_3=3.8	W_4=3.8	W_5=3.5	W_6=1.1

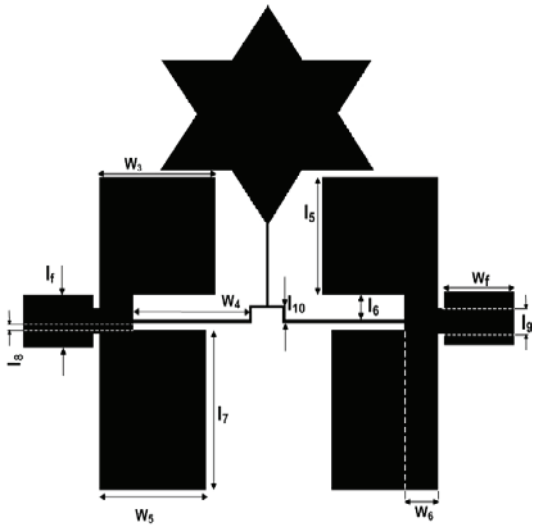

Fig. 11. Layout of proposed LPF.

III. SIMULATION AND MEASUREMENT

The photograph of the fabricated proposed LPF and also measurement and simulation results, are shown in Figs. 12 and 13, respectively. The EM simulation of the LPF is performed by the ADS software. The suggested LPF is fabricated on a RT/Duroid 5880 substrate with the dielectric constant of 2.2, loss-tangent of 0.0009 and height of 0.508 mm.

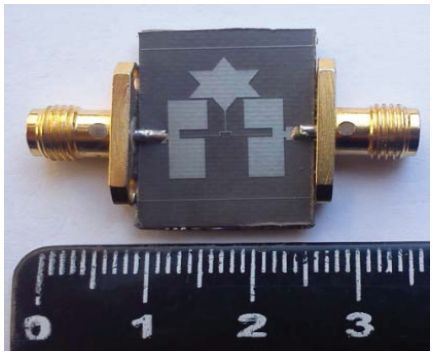

Fig. 12. Photograph of the fabricated LPF.

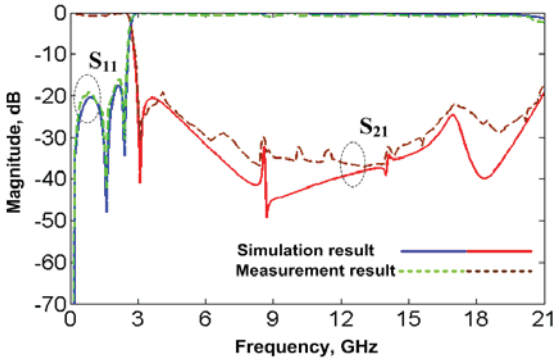

Fig. 13. Measured and simulated S-parameter of the proposed filter.

The measurement is performed by an Agilent network analyzer. As indicated in Fig. 13, there is a good agreement between the simulation and measurement results. The maximum variation of the group delay of the proposed LPF in the 93% of the pass-band region is 0.475 ns; which is a very small amount, nearby an ideal point for a LPF, as illustrated in Fig. 14. The proposed LPF with -3 dB cutoff frequency of 2.57 GHz has the insertion loss less than 0.1 dB from DC to 2.391 GHz (which is about 93% of the pass-band bandwidth). The stop-band bandwidth is 17.81 GHz (from 2.84 GHz to 20.65 GHz), with the attenuation level better than -20.5 dB; thus, the expanded stop-band is 6.93 times of -3 dB cutoff frequency. The transition-band between -3 dB and -20 dB is about 0.27 GHz. In addition, the overall size of the LPF is only 11.4 mm × 13.6 mm.

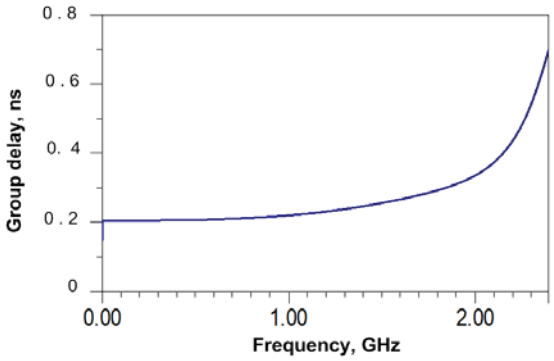

Fig. 14. Group-delay of the proposed LPF.

The performance of the proposed LPF in comparison with other published works is summarized in Table 2. Where ζ is the roll-off rate that is used to evaluate the roll-off sharpness, which is defined as [15]:

$$\xi = \frac{\alpha_{max} - \alpha_{min}}{f_S - f_C}, \quad (3)$$

where α_{max} is the -20 dB attenuation point, α_{min} is the -3 dB attenuation point, f_s is the -20 dB stop-band frequency and f_c is the -3 dB cutoff frequency.

The Relative Stop-band Bandwidth (RSB) is given by [15]:

$$RSB = \frac{stopband(-20dB)}{stopband\ center\ frequency}. \quad (4)$$

The Normalized Circuit Size (NCS) is applied to measure the degree of the miniaturization of different filters and formulated as [15]:

$$NCS = \frac{physical\ size\ (length \times width)}{\lambda_g{}^2}, \quad (5)$$

where λg is the guided wavelength at -3 dB cutoff frequency.

The Suppressing Factor (SF) is related to the suppression in the stop-band and calculated as [15]:

$$SF = \frac{Rejection\ level}{10}. \quad (6)$$

The Architecture Factor (AF) can be identified as the circuit complexity factor, which is signed as 1 when the design is 2D and as 2 when the design is 3D. Finally, the Figure-of-Merit (FOM) is defined as [15]:

$$FOM = \frac{\xi \times RSB \times SF}{NCS \times AF}. \quad (7)$$

Table 2: Performance comparison of the proposed LPF with other published works

Ref.	ζ (dB/GHz)	RSB	NCS (λ_g^2)	FOM
[1]	34.48	1.22	0.096	876
[5]	43.58	1.67	0.029	5020
[6]	27.40	0.68	0.009	4140
[9]	24.28	1.65	0.010	6009
[10]	23.53	1.55	0.007	7815
[11]	25.00	1.51	0.008	8022
[12]	28.33	1.03	0.012	4863
[13]	22.66	1.25	0.006	7081
This work	62.35	1.52	0.021	9252

According to Table 2, the proposed low-pass filter has a good RSB and also has the highest roll-off rate and FOM among the published works.

IV. CONCLUSION

In this paper, a LPF using the star-shaped resonator combined with C-shaped suppressing cells is designed, fabricated and measured. This structure leads to a compact size, sharp roll-off characteristic and an expanded stop-band bandwidth, as well as good insertion loss and return-loss in both stop-band and pass-band region. Also, because of having a simple structure, the fabrication process is so convenient. The proposed structure with such a high performance can be applied in modern high frequency communication systems as an efficient and merit LPF.

ACKNOWLEDGMENT

The authors would like to thank the Islamic Azad University, Kermanshah Branch, for their financial support of this research project.

REFERENCES

[1] A. S. Mohra, "Microstrip low pass filter with wideband rejection using opened circuit stubs and z-slots defected ground structures," *Microwave and Optical Technology Letters*, vol. 53, no. 4, pp. 811-815, April 2011.

[2] M. Al-Sharkawy, A. Boutejdar, F. Alhefnawi, and O. Luxor, "Improvement of compactness of low-pass/band-pass filter using a new electromagnetic coupled crescent defected ground structure resonators," *Applied Computational Electromagnetics Society Journal*, vol. 25, no. 7, pp. 570-577, July 2010.

[3] M. Challal, A. Boutejdar, M. Dehmas, A Azrar, and A. Omar, "Compact microstrip low-pass filter design with ultra-wide reject and using a novel quarter-circle DGS shape," *Applied Computational Electromagnetics Society Journal*, vol. 27, no. 10, October 2012.

[4] G. E. Al-Omair, S. F. Mahmoud, and A. S. Al-Zayed, "Low-pass and band-pass filter designs based on DGS with complementary split ring resonators," *Applied Computational Electromagnetics Society Journal*, vol. 26, no. 11, November 2011.

[5] Y. Yousefzadeh and M. Hayati, "Compact low-pass filter with wide stopband using a tapered microstrip resonator cell," *Microwave Journal*, vol. 55, no. 3, pp. 122-128, March 2012.

[6] M. H. Yang, J. Xu, Q. Zhao, L. Peng, and G. P. Li, "Compact broad stop-band low-pass filters using sirs-loaded circular hairpin resonators," *Progress In Electromagnetics Research*, *vol.* 102, pp. 95-106, 2010.

[7] A. Adinehvand and A. Lotfi, "Compact low-pass filter with wide stop-band using open stubs-loaded spiral microstrip resonant cell," *Applied Computational Electromagnetics Society Journal*, vol. 28, no. 1, January 2013.

[8] H. R. Khakzad, S. H. Sedighy, and M. K. Amirhosseini, "Design of compact SITLs low-pass filter by using invasive weed optimization (IWO) technique," *Applied Computational Electromagnetics Society Journal*, vol. 28, no. 3, March 2013.

[9] J. Wang, H. Cui, and G. Zhang, "Design of compact microstrip low-pass filter with ultra-wide stop band," *Electronics Letters*, vol. 48, no. 14, pp. 854-856, July 2012.

[10] H. Cui, J. Wang, and G. Zhang, "Design of microstrip low-pass filter with compact size and ultra-wide stop-band," *Electronics Letters*, vol. 48, no. 14, pp. 856-857, July 2012.

[11] L. Ge, J. P. Wang, and Y. X. Guo, "Compact microstrip low-pass filter with ultra-wide stop band," *Electronics Letters*, vol. 46, no. 10, pp. 689-691, May 2010.

[12] J. Y. Wu, Y. H. Tseng, and W. H. Tu, "Design of compact low-pass filter with ultra-wide stop band using thin slots," *Progress In Electromagnetics Research C*, vol. 31, pp. 137-151, 2012.

[13] X. B. Wei, P. Wang, M. Q. Liu, and Y. Shi, "Compact wide stop-band low-pass filter using stepped impedance hairpin resonator with radial stubs," *Electronics Letters*, vol. 47, no. 15, pp. 862-863, July 2011.

[14] J. S. Hong and M. J. Lancaster, "Microstrip filters for RF/microwave applications," *John Wiley & Sons, Inc.*, New York, 2001.

[15] M. Hayati, F. Shama, and H. Abbasi, "Compact microstrip low-pass filter with wide stop-band and sharp roll off using tapered resonator," *International Journal of Electronics*, vol. 100, no. 12, pp. 1751-1759, 2013.

Mohsen Hayati received his B.E degree in Electronics and Communication Engineering from Nagarjuna University, India in 1985 and his M.E. and Ph.D. degrees in Electronics Engineering from Delhi University, Delhi, India in 1987 and 1992, respectively. He joined the Electrical Engineering Department at Razi

University, Kermanshah, Iran as an Assistant Professor in 1993. At present, he is an Associate Professor with the Electrical Engineering Department at Razi University. He has published more than 135 papers in international and domestic journals and conferences. His current research interests include microwave and millimeter wave devices and circuits, application of computational intelligence, artificial neural networks, fuzzy systems, neuro-fuzzy systems, electronic circuit synthesis and modeling and simulations.

Zahra Faramarzi received her B.E. and M.E. degrees in Electronics Engineering from Razi University, Kermanshah, Iran in 2005 and 2013, respectively. Her current research interests include design of RF circuits and MMIC.

Mozhgan Amiri received her B.E. and M.E. degrees in Electronics Engineering from Razi University, Kermanshah, Iran in 2005 and 2013, respectively. Her current research interests include RF electronics microwave circuit design and modeling RFIC and MMIC.

Triple Notch UWB Antenna Controlled by Novel Common Direction Pentagon Complementary Split Ring Resonators

Bo Yan [1], Di Jiang [2], Jian Chen [3]

[1] School of Electronic Engineering
University of Electronic Science and Technology of China, Chengdu 611731, China

[2] School of Communication and Information Engineering
University of Electronic Science and Technology of China, Chengdu 611731, China

[3] Center for Advanced Photonics and Electronics, Department of Engineering
University of Cambridge, 9 JJ Thomson Avenue, Cambridge CB3 0FA, UK

Abstract ─ A small-size CPW-feed multi-band planar monopole antenna is presented. A Swallow-Shaped-Patch (SSP) that covers the Ultra-Wideband (UWB) frequency range is used in the proposed design. To create a multi-band antenna, several narrow pentagon slots, acting as resonance paths, can be integrated with the SSP antenna. Triple-band antennas are simulated and good results are obtained, while showing a very sharp band-rejection performance at 3.92 GHz, 5.34 GHz and 5.88 GHz, respectively. The antennas have omnidirectional and stable radiation patterns across all the relevant bands. Moreover, a prototype of the triple-band antenna is fabricated and measurement results are compared with simulation results.

Index Terms - Monopole antenna, multi-band antenna and Ultra-Wideband (UWB) antenna.

I. INTRODUCTION

Ultra-Wideband (UWB) technology is now becoming widely used in a variety of applications, such as radar, short-range communications and positioning systems. This is because this technology offers advantages of large channel capacity, multipath propagation performance and potential for ultra-low-power implementation of transmitting-only devices. As is the case, in conventional wireless communication systems, antennas play a crucial role in UWB systems. However, there are more challenges in designing a UWB antenna than a narrow band one. In particular, a suitable UWB antenna should be capable of operating over an ultra-wide bandwidth, as allocated by the Federal Communications Commission (FCC); that is 3.1-10.6 GHz. At the same time, it needs to exhibit satisfactory radiation properties over the entire frequency range. In addition, the antenna needs to be compact in size and cheap to manufacture for consumer electronic applications. To satisfy these requirements, various wideband antennas have been studied [1]. However, other narrow band services coexist within the UWB spectra, such as C-band (3.7-4.2 GHz) satellite communication systems and Wireless Local-Area Network (WLAN) IEEE802.11a and HIPERLAN/2 systems, operating in the 5.15-5.35 GHz and 5.725-5.825 GHz band, respectively. To overcome this problem, agile software-defined radios provide a solution that demands the use of smart reconfigurable antennas capable of cancelling in-band interference. Hence, a UWB antenna with reconfigurable band-rejection characteristics at the WLAN or C-band satellite frequencies is highly desirable.

In this paper, we present a compact printed antenna with co-directional pentagon Complementary Split-Ring Resonators (CSRR), which has an UWB operating bandwidth with a tunable triple-notched frequency at 3.9 GHz, 5.2 GHz and 5.9 GHz. Band-notched operation is

Submitted On: May 17, 2013
Accepted On: May 3, 2014

achieved by embedding co-directional modified CSRR slots on the radiated patch. The CSRR is under investigation by researchers to implement left-hand materials and the co-directional Complementary Split Ring Resonator (CSRR) is promising for UWB antennas to enable multiple notched bands [2]. Both triple-band-notched characteristics and compact size are achieved. The antenna has promising features, including good impedance matching performance over the whole operating frequency band, stable radiation patterns and flexible frequency notched function.

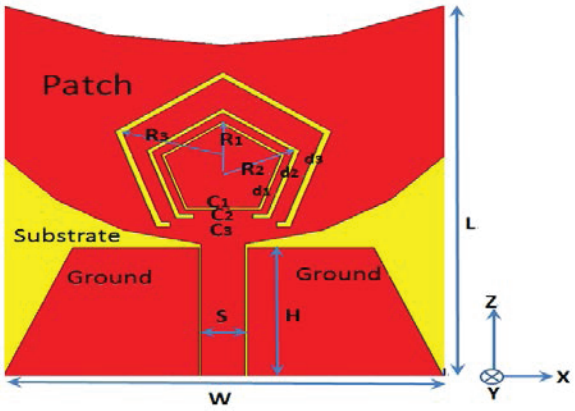

Fig. 1. Geometry of antenna, width dimensions are: R_1=4.01 mm, R_2=4.90 mm, R_3=6.95 mm, C_1=0.6 mm, C_2=3.35 mm, C_3=6 mm, d_1=0.2 mm, d_2=0.32 mm, d_3=0.45 mm, s=2.5 mm, H=9.8 mm, W=25 mm and L=27.9 mm.

II. ANTENNA DESIGN

The geometry of the proposed co-directional pentagon split-ring resonators slot UWB antenna with band-notch function, is depicted in Fig. 1. The antenna is located on the xz-plane and the normal direction is parallel to the xy-axis. The radiating ring is fed via the 50Ω Coplanar Waveguide (CPW) feed-line of width 2.5 mm, as illustrated in Fig. 2. The proposed antenna was fabricated on a dielectric substrate RT5880 with a relative permittivity (ε_r) of 2.2 mm and thickness of 0.508 mm. A common direction pentagon complementary split ring resonators slot are used and fabricated on the radiation patch. To achieve good impedance matching for the ultra-wide band operation, the swallow radiator is fed by a Coplanar Waveguide (CPW) transmission line with trapezoidal ground-plane, which is terminated with a Sub Miniature A (SMA) connector for the measurement purpose. Since the antenna and the feeding are fabricated on the same side of the plane, only one layer of substrate with single-sided metallization is used, which makes the manufacturing of the antenna very easy and extremely cost-effective. Good performance of multiple band-notched characteristic is simply accomplished by embedding common direction pentagon CSRRs to the swallow patch. The simulation is optimized using the commercial 3-D electromagnetic software HFSS [3].

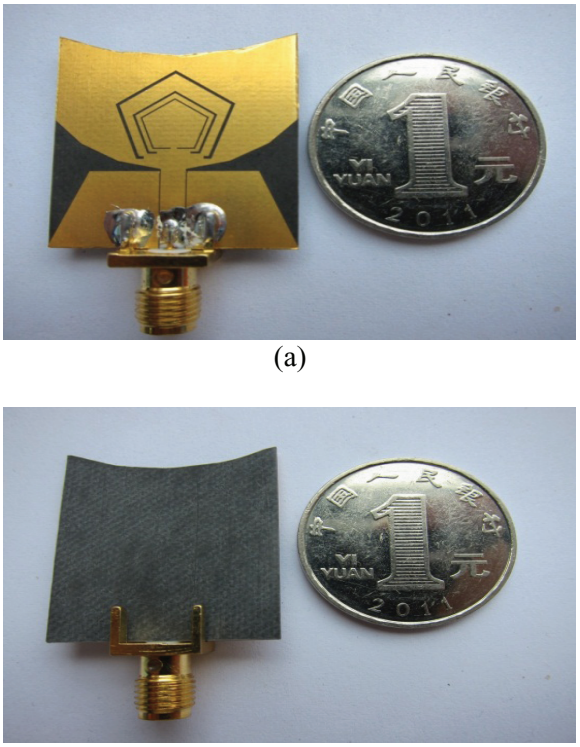

(a)

(b)

Fig. 2. Photograph of the proposed antenna: (a) front view and (b) bottom view.

Figure 3 shows the current distributions at three center notched bands. The dimensions of three co-directional pentagons CSRRs are corresponding to three notched bands. When the antenna is working at the center of the lower notched band near 3.9 GHz, the outer CSRR behaves as a separator, shown in Fig. 3 (a), which almost has no relation to the other band-notches [4]. Similarly, the middle CSRR operates as a second separator for the center of the middle notched band near 5.2 GHz, in Fig. 3 (b). As seen

in Fig. 3 (c), the upper notched band near 5.9 GHz is ensured by the inner CSRR [5]. Additionally, as a certain current crowded on the ground plane near the CPW feed line would affect the antenna performance, we find that the dimension of the ground plane particularly has a significant effect on the triple band-notches performance and the impedance bandwidth, according to the simulation results [6].

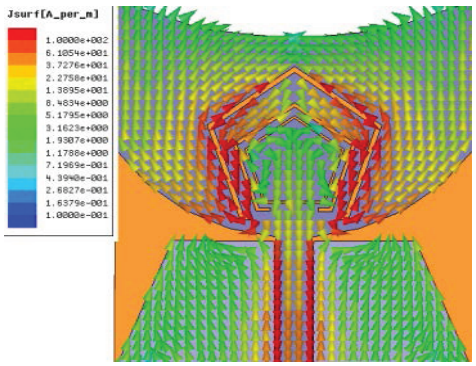

(a)

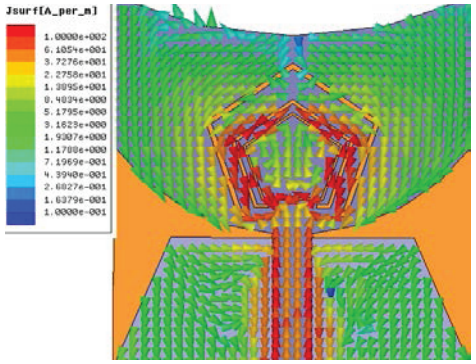

(b)

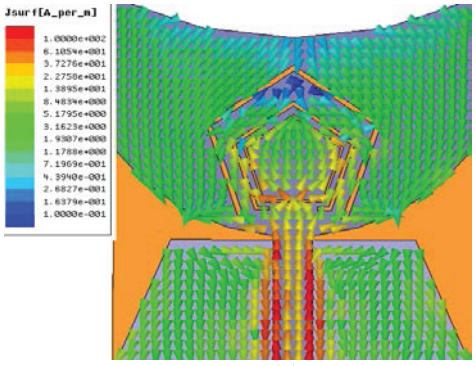

(c)

Fig. 3. The current distribution at: (a) 3.9 GHz, (b) 5.2 GHz and (c) 5.9 GHz.

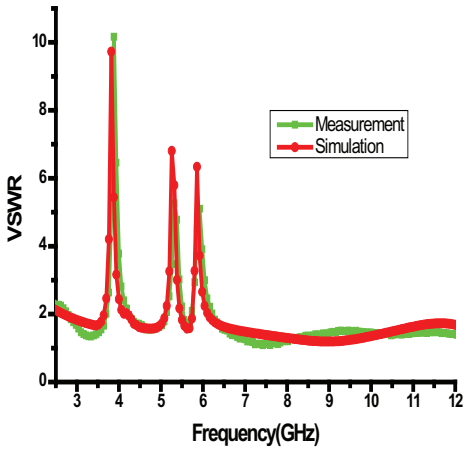

Fig. 4. Comparison of simulated and measured VSWR of proposed antenna.

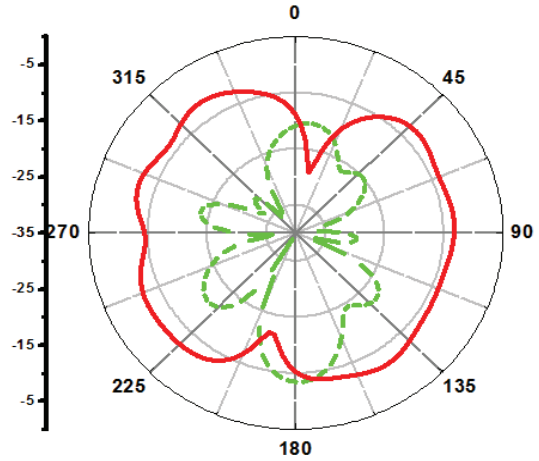

F=3.5 GHz

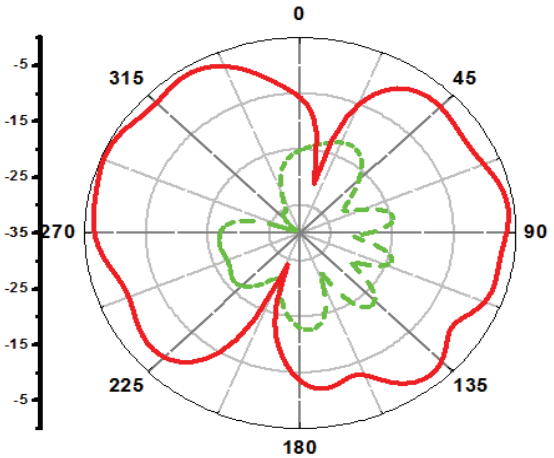

F=7.5 GHz

(a)

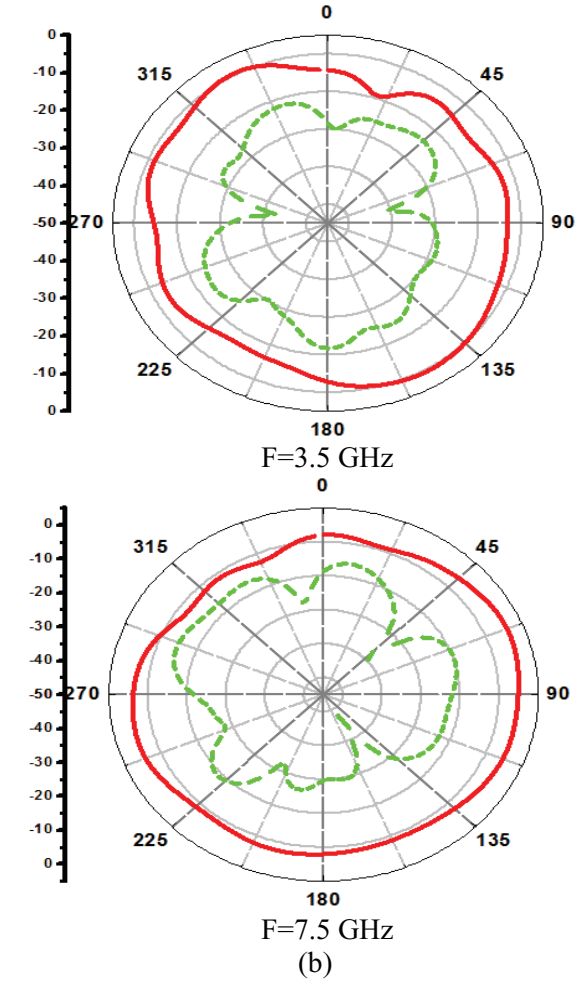

Fig. 5. Measured radiation patterns at: (a) yz-plane and (b) xy-plane.

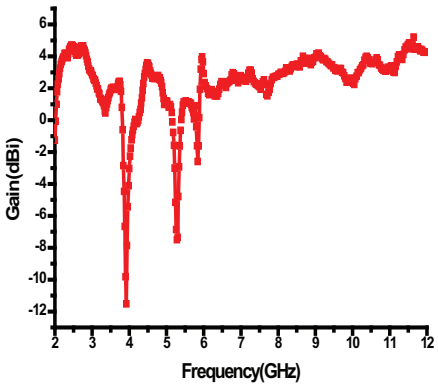

Fig. 6. Measured gain of proposed antenna.

III. RESULTS AND DISCUSSION

The VSWR performance of the fabricated prototype was measured using an Agilent 85052C vector network analyzer. Figure 4 shows the simulated and measured VSWRs for the proposed antenna, as well as the reference antenna. Band-notched function is obtained by introducing the co-directional pentagon CSRRs. The designed antenna has an impedance bandwidth of 2.6-12 GHz for VSWR less than 2, except the frequency-notched band of 3.68-4.20 GHz, 5.12-5.45 GHz and 5.72-6.08 GHz, respectively. Obviously, this measured frequency range covers commercial UWB band (3.1-10.6 GHz) and rejects the frequency band of C-band satellite communication systems and IEEE 802.11a, to overcome Electromagnetic Interference (EMI) problems among UWB and WLAN [7]. As shown in Fig. 4, it is also observed that the measured notched-band width is slightly wider than the simulated result. This may be caused by the use of an SMA connector and fabrication errors.

The measured far-field radiation patterns of the proposed antenna in H-plane (xy-plane) and E-plane (yz-plane) at frequencies 3.5 GHz and 7.5 GHz, are plotted in Fig. 5, respectively. Like the behavior of conventional wide slot antennas, the proposed antenna has relatively omnidirectional xy-plane (H-plane) radiation patterns with non-circularity of about 5-8 dB, over the operating frequency band [8]. The radiation patterns in yz-plane (E-plane) are monopole alike. All the obtained radiation patterns agree with those of the conventional printed UWB monopole antennas [9]. The proposed antenna has proved to be capable of providing favorable spatial-independent band-notched characteristics.

Figure 6 plots measured peak gain against frequency for the band-notched antenna [10]. It reveals that the antenna gain ranges from 1.9 dBi to 5 dBi within the 2-12 GHz frequency band. Note that this doesn't include the notched band in which it decreases significantly to about -12 dB, -8 dB and -3 dB [11]. It is confirmed that the proposed antenna provides a high level of rejection to signal frequencies within the notched band [12-15].

IV. CONCLUSION

A novel compact CPW-fed printed monopole

antenna with three band-notched characteristics has been proposed for UWB applications. We showed that three more resonances are excited by embedding co-directional pentagon CSRRs with proper dimensions and position in the radiation pattern. As a result, wide impedance bandwidth from 2.6 GHz to 12 GHz is achieved. The designed antenna has a simple configuration and an easy fabrication process. The experimental results show that the proposed antenna with a very compact size, simple structure and wide bandwidth can be a good candidate for UWB application.

ACKNOWLEDGMENT

This work is supported by National Natural Science Foundation of China (Grant No. 61106115 and 60971037) and the Fundamental Research Funds for the Central Universities (ZYGX2011J018).

Yan and Jiang（Fundamental Science on EHF Laboratory, University of Electronic Science and Technology of China, Chengdu, China).

Chen is a Ph.D. student in the Engineering Department at the University of Cambridge.

REFERENCES

[1] Z. N. Chen, N. Yang, Y. X. Guo, and M. Y. W. Chia, "An investigation into measurement of handset antennas," *IEEE Trans. Instrum. Meas.*, vol. 54, pp. 1100-1110, June 2005.

[2] L. Liu, Y. Z. Yin, C. Jie, J. P. Xiong, and Z. Cui, "A compact printed antenna using slot-type CSRR for 5.2 GHz / 5.8 GHz band-notched UWB application," *Microw. Opt. Technol. Lett.*, vol. 50, no. 12, pp. 3239-3242, December 2008.

[3] "Ansoft high frequency structure simulation (HFSS)," ver. 10, *Ansoft Corp*, 2005.

[4] F. Falcone, T. Lopetegi, M. A. G. Laso, J. D. Baena, J. Bonache, M. Beruete, R. Marqués, F. Martín, and M. Sorolla, "Babinet principle applied to the design of metasurfaces and metamaterials," *Phys. Rev. Lett*., vol. 93, p. 197401, 2004.

[5] M. T. Partovi, N. Ojaroudi, and M. Ojaroudi, "Small slot antenna with enhanced bandwidth and band-notched performance for UWB applications," *Applied Computational Electromagnetics Society (ACES) Journal*, vol. 27, no. 9, pp. 772-778, September 2012.

[6] J. Ding, Z. Lin, Z. Ying, and S. He, "A compact ultra-wideband slot antenna with multiple notch frequency bands," *Microw. Opt. Technol. Lett*., vol. 49, no. 12, pp. 3056-3060, December 2007.

[7] Y. D. Dong, W. Hong, Z. Q. Kuai, C. Yu, Y. Zhang, J. Y. Zhou, and J. Chen, "Development of ultra-wideband antenna with multiple band-notched characteristics using halfmode substrate integrated waveguide cavity technology," *IEEE Trans. Antennas Propag*., vol. 57, no. 12, pp. 2894-2902, December 2009.

[8] K. S. Ryu and A. A. Kishk, "UWB antenna with single or dual band-notches for lower WLAN band and upper WLAN band," *IEEE Trans. Antennas Propag*., vol. 57, no. 12, pp. 3942-3950, December 2009.

[9] A. M. Montaser, K. R. Mahmoud, and H. A. Elmikati, "Integration of an optimized e-shaped patch antenna into laptop structure for bluetooth and notched-UWB standards using optimization techniques," *Applied Computational Electromagnetics Society (ACES) Journal*, vol. 27, no. 10, pp. 786-794, October 2012.

[10] X. N. Low, Z. N. Chen, and T. S. P. See, "A UWB dipole antenna with enhanced impedance and gain performance," *IEEE Trans. Antennas Propag*., vol. 54, no. 10, pp. 2959-2966, October 2009.

[11] B. H. Siahkal-Mahalle, M. Ojaroudi, and N. Ojaroudi, "Enhanced bandwidth small square monopole antenna with band-notched functions for UWB wireless communications," *Applied Computational Electromagnetics Society (ACES) Journal*, vol. 27, no. 9, pp. 759-765, September 2012.

[12] D. Jiang, X. Yuehang, X. Ruimin, and L. Weigan, "Compact dual-band-notched UWB planar monopole antenna with modified CSRR," *Electronics Letters*, vol. 48, (20), no. 27, pp. 1250-1252, September 2012.

[13] A. Nouri and G. R. Dadashzadeh, "A compact UWB band-notched printed monopole antenna with defected ground structure," *IEEE Antennas and Wireless Propagation Letters*, vol. 10, pp. 1178-1181, 2011.

[14] W. Chao-Ming, C. Yung-Lun, and L. Wen-Chung, "A Compact ultra-wideband slotted patch antenna for wireless USB dongle application," *IEEE Antennas and Wireless Propagation Letters*, vol. 11, pp. 596-599, 2012.

[15] F. Wei, Z. Dan Wang, F. Yang, and X. Wei Shi, "Compact UWB BPF with triple-notched bands based on stub loaded resonator," *Electronic Letters*, vol. 49, no. 2, January 17, 2013.

Bo Yan received his B.Sc., Master and Ph.D. degrees in 1991, 1994 and 1998, respectively in Electromagnetic Field and Microwave Technology from the University of Electronic Science and Technology of China (UESTC). He has been an Associate Professor at UESTC since 2000. His research interests include microwave and millimeter wave circuit designing.

Di Jiang received his B.S. degree in Communication Engineering from Gui Lin University of Electronic Technology (GLIET), China in 2004 and is currently pursuing his Ph.D. degree in Electromagnetic Field and Microwave Technology at the University of Electronic Science and Technology of China (UESTC), Chengdu, China. His research interests include miniature antenna, RF circuit and metamaterial design and its application.

Jian Chen received a joint B.Eng in Electronics and Communication Engineering from the University of Birmingham and Huazhong University of Science and Technology in 2009. He graduated with a Master degree in Electrical Engineering at Columbia University in 2010 and has since worked at Mini-Circuits and LSI Corporation in the USA, respectively. He is currently a Ph.D. student at the University of Cambridge, UK. His research interests include microwave circuit design, antenna design and optical interconnects 1.2×1 inch.

Susceptibility of a Simple Transmission Line Inside an Enclosure Against Normal Incident Plane Wave

S. Abadpour [1], P.Dehkhoda [2], R. Moini [1], S. H. H. Sadeghi [1] and H. R. Karami [3]

[1] Department of Electrical Engineering
AmirKabir University of Technology, Tehran 15875-4413, Iran
sevda.abadpour@aut.ac.ir, moini@aut.ac.ir, sadeghi@aut.ac.ir

[2] Institute of Communications Technology and Applied Electromagnetics
AmirKabir University of Technology, Tehran 15875- 4413, Iran
pdehkhoda@aut.ac.ir

[3] Department of Electrical Engineering
Bu-Ali Sina University, Hamadan 65178, Iran
hamidr.karami@basu.ac.ir

Abstract ─ In this paper, susceptibility of a Microstrip Transmission Line (MTL) as a simple Printed Circuit Board (PCB) against a normal incident plane wave is studied. Here, the induced voltage on the open port of the MTL is considered as the susceptibility criterion for the MTL. Two different approaches are applied: the Method of Moments (MoM) and the Finite Integration Technique (FIT). In addition to simulations, we performed measurements inside a semi-anechoic chamber. Both simulations show very good agreement with the measurements. In addition to frequency domain results, time domain induced open circuit voltage is calculated. The effect of different aperture sizes on the susceptibility of a shielded MTL is examined. It is shown that large apertures can multipy the disagreeable effect of the interfering wave on the MTL, compared to the case where no shield is utilized.

Index Terms - Finite Integral Technique (FIT), Method of Moments (MoM), microstrip transmission line susceptibility, shielding enclosure and susceptibility measurements.

I. INTRODUCTION

Failure and malfunction of electronic systems that are sensitive to electromagnetic disturbances is becoming a serious problem [1]. The malfunctioning of an electronic system can be related to its susceptibility to an external electromagnetic field. As defined in [2], susceptibility is a relative measure of a device or a system's propensity to be disrupted or damaged by Electromagnetic Interference (EMI) exposure to an incident field.

The radiated susceptibility of a Printed Circuit Board (PCB) influenced by an external electromagnetic field can be a criterion to determine the susceptibility of a whole electronic device. The induced interference signal on the traces of a PCB causes partial functional failures or even irreversible damages; depending on the shape and amplitude of the interference signal as well as the trace properties. Different numerical methods such as Method of Moments (MoM) and Finite Element Method (FEM) have been utilized to evaluate the susceptibility of a bare PCB [3-6]. On the other hand, in order to measure susceptibility of a PCB, different test cells are used, such as a transverse Electromagnetic Transmission Cell (TEM cell) [7], an Asymmetric Transverse Electromagnetic Transmission cell (ATEM cell) [8], Gigahertz Transverse Electromagnetic Transmission cell (GTEM cell) [6,9] and reverberating chamber [10]. In those measurements, an unshielded PCB is examined and the induced voltage on different parts of the

Submitted On: April 6, 2013
Accepted On: April 19, 2014

PCB is defined as the susceptibility of the circuit. Generally speaking, metallic enclosures are widely used to hinder electromagnetic leakage from electronic equipment and also to reduce the susceptibility of the sensitive devices against external interference. Numerous techniques have been utilized to evaluate the SE of perforated empty [11-14] and also loaded enclosures [15-19]. In most practical applications, Shielding Effectiveness (SE) and consequently the susceptibility of a PCB inside the enclosure are primarily affected by the apertures perforated to accommodate visibility, ventilation or access to interior components [20].

In this paper, susceptibility of a typical Microstrip Transmission Line (MTL) as a simple PCB enclosed within a perforated cavity is studied. To this end, two different numerical methods are utilized. For a MTL with air cushion, an efficient MoM code is developed to solve the governing Electric Field Integral Equation (EFIE), with the well-known Rao–Wilton–Glisson (RWG) basis functions [10] for the unknown electric currents on the surface of the enclosure. The second approach is the Finite Integration Technique (FIT) by CST, the well-known commercial software that solves the problem of MTL with dielectric substrate. By evaluating the electric filed at the open port of the MTL, the induced open circuit voltage (V_{oc}) as the determinant parameter for MTL susceptibility is calculated.

In addition to simulations, Electromagnetic Susceptibility (EMS) measurements have been performed for different shielded and unshielded MTLs inside a semi-anechoic chamber. To the knowledge of the authors, it is for the first time that EMS test of a PCB inside a semi-anechoic chamber with an interference producing antenna is reported. This setup has been used frequently for SE measurements of empty enclosure [13,18]. It will be shown that measurements are in very good agreement with the simulation results. In this paper, the main goal is to study the susceptibility of a shielded MTL at resonant frequencies of the enclosing perforated enclosure; thus, for the considered enclosure, measurements are performed at 500-1000MHz.

In addition to frequency domain results, time domain induced voltage on the open port of the MTL caused by a Gaussian plane wave is calculated. It will be shown that using the enclosure with a large aperture not only does not protect the MTL against the interfering wave, but also decrease the immunity of the MTL.

This paper is organized as follows: section II reviews the employed numerical solution methods. Then the measurement setup is described. Section III studies the effect of different aperture sizes on the immunity of a shielded MTL. Also, time domain results are discussed. A brief conclusion is presented in section IV.

II. THEORY

Here, the RWG-MoM technique is chosen to solve the governing EFIE in the problem of a shielded MTL with air cushion. A MATLAB code is developed on a Core™ i7-2600 CPU @ 3.4 GHz, with 8 GB of RAM. For the MTL with dielectric substrate, CST software is utilized. Both simulations are compared with the measurements. A brief formulation for RWG-MoM and FIT are found in sub-section A and B, respectively. In subsection C, experimental setup is introduced and the open voltage calculation from the measured data is presented.

A. MoM approach

A rectangular metallic cube with interior dimensions of $a \times b \times c$ and wall thickness of d is illustrated in Fig. 1. A rectangular aperture with length L and width W is located at the center of the cavity's illuminated surface.

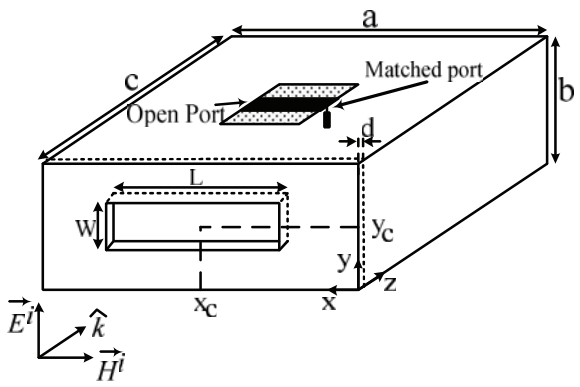

Fig. 1. Geometry of problem.

The incident plane wave is $\vec{E}^i$ and the MTL is placed inside the enclosure. The MTL is matched at one port and is open at the other port.

According to physical equivalence theorem [21], incident wave induces an electric current $\vec{J}$ on the metallic parts of the structure. The scattered fields ($\vec{E}^s$,$\vec{H}^s$) by $\vec{J}$ are calculated at any point inside or outside the enclosure by [21]:

$$\vec{E}^s = -j\omega\mu \iint \vec{J}\, G(r,r')ds' - \frac{j}{\omega\varepsilon}\iint (\vec{\nabla}\cdot\vec{J})\vec{\nabla}_r G(r,r')ds', \quad (1)$$

$$\vec{H}^s = \frac{1}{\mu}\nabla\times\vec{A} = \frac{-1}{4\pi}\iint \vec{J}\times G(r,r'), \quad (2)$$

where $G(r,r')$ is the free space of Green's function, and

$$\vec{\nabla}_r G(r,r') = \frac{\partial}{\partial r}\big(G(r,r')\big) = \frac{\partial}{\partial R}\big(G(r,r')\big)\times \frac{\partial R}{\partial r} = \frac{-e^{-jkR}}{4\pi R}\left(jk+\frac{1}{R}\right)\hat{R}. \quad (3)$$

Applying the boundary condition on the perfect metallic parts of the structure, an EFIE is obtained. Afterward, $\vec{J}$ is expanded by RWG basis functions on the triangular shaped discretization [22]. The resultant integral equation is then solved by MoM. Detailed study on RWG-MoM solution is presented in [22]. Having the coefficients of $\vec{J}$ on the meshes and re-using (1)-(3), the scattered electromagnetic field at any point is achieved. By integrating the obtained total electric field along the length of the MTL open port, V_{oc} is calculated. Please note that if no dielectric with permittivity constant larger than 1 is used in the problem, there is no limitation on the shape of the enclosure, the aperture or the MTL in the applied method. To this end, air substrate is used for the MTL. In order to consider the wall thickness, the aperture surrounding walls and the enclosure, internal and external walls should be discretized.

B. FIT method

Maxwell's equations can be applied in their integral form to the cells of a discretized problem [23,24]. This approach is the basis of the Finite Integration Technique (FIT) that is found to be a suitable numerical method for analyzing electromagnetic problems, due to its high flexibility as well as its ability to deal with arbitrary material distributions, geometrical modeling, curved boundaries and complex shapes. In homogeneous media, the discretization method of FIT is similar to the FDTD method. However, the FIT transforms Maxwell's equations in their integral form to a linear system of equations. This technique treats interfaces between different media in a more accurate manner [24].

Various approaches based on an adaptive mesh, the sub-gridding, the Conformal FIT (CFIT) and Non-Orthogonal Grids (NFIT) have been introduced to overcome staircase approximation. A finer mesh can be used only in sections where higher accuracy is required by employing adaptive mesh approaches; therefore, this reduces the number of grid points in the whole simulation area [23,24]. The powerful Computer Simulation Technology (CST) commercial software is a developed code based on FIT method.

In this paper, CST is used to analyze the susceptibility of shielded and unshielded MTLs with air and dielectric substrates. Respectively, 172, 260 and 1,163,264 mesh cells are required to obtain convergent results for the unshielded and shielded MTL with dielectric substrate. For the MTL with air cushion, necessary mesh cells are 284,026 and 1,608,576 for the unshielded and shielded, respectively. The high number of meshes in the shielded case is due to the relatively small size of MTL when compared to the large size of the enclosure.

C. Experimental setup

Measurements are performed inside a semi-anechoic chamber using a horn antenna as the source of interference. The antenna is placed 2 m away from the MTL (shielded or unshielded) in its line of sight, as shown in Fig. 2, to satisfy the far field region requirement. The absorbers are put between the antenna and the MTL to remove the reflection from the floor.

Figure 3 shows a schematic of the measurement setup. A Vector Network Analyzer (VNA) is used to measure the scattering parameters. The VNA is placed outside of the anechoic chamber and its port 1 is connected to the antenna. MTL is connected to VNA port 2 at one side and at the other side it is matched.

In order to calculate the induced V_{oc} on the MTL from the measurement results, the measured scattering parameters are related to the open circuit voltage by [25]:

$$V_{oc} = \frac{2S_{21}}{(1-S_{11})(1-S_{22})-S_{12}S_{21}} I_1, \quad (4)$$

where I_1 is calculated from the known injected power by the VNA into its port 1 and its 50 Ω

characteristic impedance, neglecting the reflection from the antenna. We set the power of the VNA at its port 1 in a way that the incident field amplitude at the enclosure exposed wall to be 1 V/m. For calculating the necessary power, loss of cables, gain of the antenna and the distance between antenna and the enclosure's perforated wall is considered.

Fig. 2. Experimental setup of test.

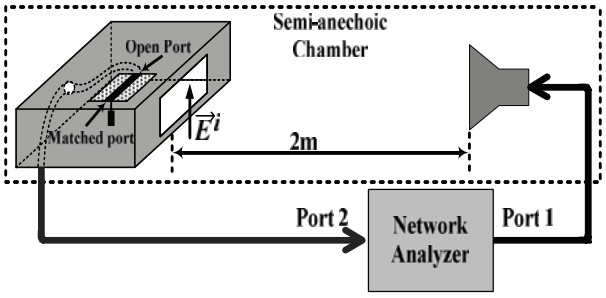

Fig. 3. Schematic of setup test.

III. RESULTS

A. Frequency domain analysis

Utilized shielding enclosure is a 30×12×30 cm^3 box with one 18×5 cm^2 aperture in the illuminated wall. Two different MTLs are examined. The first one has 3.18 mm air substrate with trace width and length of 15.6 mm and 74.9 mm, respectively (Fig. 4 (a)). Since there is no dielectric in this MTL, it is suitable to be analyzed by the developed RWG-MoM code. The second one is a more practical MTL with RO4003 substrate with trace length and width of 45 mm and 1.12 mm, respectively (Fig. 4 (b)). Both are designed to have the characteristic impedance of 50 Ohm at 1 GHz. They are matched at one port and open at the other port.

The MTL is placed inside the enclosure 15 cm away from the front panel, horizontally in a way that the transmission line is perpendicular to the front wall. In the case where the shield is not used, the MTL is placed at the same location as the shielded case.

The effect of an incident plane wave on the MTL of Fig. 4 (a) is studied for two cases; shielded and unshielded. The incident electric field is polarized along y-direction and its amplitude is 1 V/m. V_{oc} is calculated by developed RWG-MoM code and is compared with CST results and measurements in Fig. 5 for unprotected and protected cases. It is clear that a very good agreement exists between the results. As observed, using the mentioned enclosure with 18×5 cm^2 aperture not only does not decrease the effect of impinging wave, but also raise the V_{oc} up to 3 times more at some frequencies.

To investigate this undesirable effect more, SE of the considered empty enclosure at its center point is calculated by CST and depicted in Fig. 6 for different aperture sizes. Please note that SE is the ratio of the field strength in the presence and absence of the enclosure at one point inside the enclosure and is defined for a shielding enclosure to show its ability to hinder the electromagnetic fields. As observed, as the aperture size increases, the bandwidth at which SE is less than zero becomes larger. Negative SE (dB) means that the level of electromagnetic field is intensified at the considered point. This happens at resonant frequencies of the enclosure with the aperture. Clearly, increasing the aperture size would decrease the Q factor of the structure and therefore the bandwidth at which SE (dB) is negative, increases. In this case, shield acts conversely and amplifies the effect of interfering wave on the MTL. Please note that for small apertures, such as 5×0.5 cm^2 in Fig. 6, shield behavior is improved significantly and SE does not have negative values.

To further study the effect of aperture size on the susceptibility of the shielded MTL, the induced voltage on the open port of the MTL with air cushion inside the enclosure is depicted in Fig. 7. The disagreeable effect of large aperture size is re-clarified in this figure.

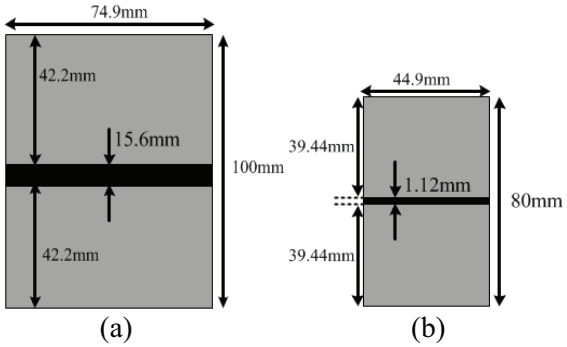

Fig. 4. Top view of MTL with: (a) air substrate and (b) with dielectric substrate.

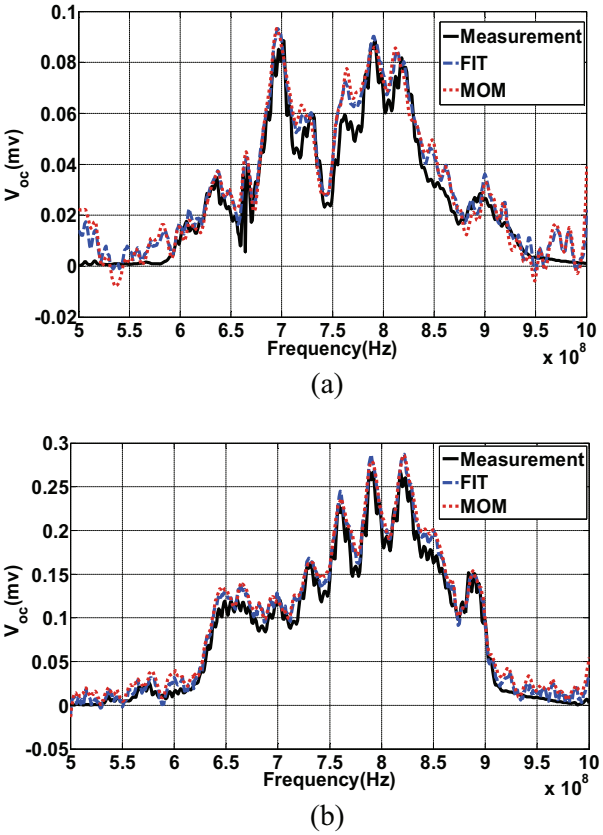

Fig. 5. Induced voltage on the open port of the MTL with air cushion of Fig. 4 (a); measurements, CST and our developed MoM for: (a) unshielded and (b) shielded cases.

As observed, aperture size of 18×5 cm^2 allows large MTL open port voltage at a wide frequency range (250 MHz), while the effect of 10×5 cm^2 aperture is limited to a small frequency band (45 MHz). Please note that for the case of very small aperture (5×0.5 cm^2) the induced open port voltage is negligible. This behavior has already been predictable by considering the SE in Fig. 6.

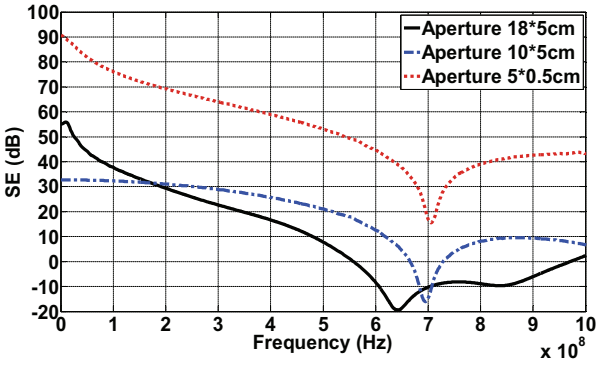

Fig. 6. SE comparison for the 30×12×30 cm^3 empty enclosure with different apertures; CST simulations.

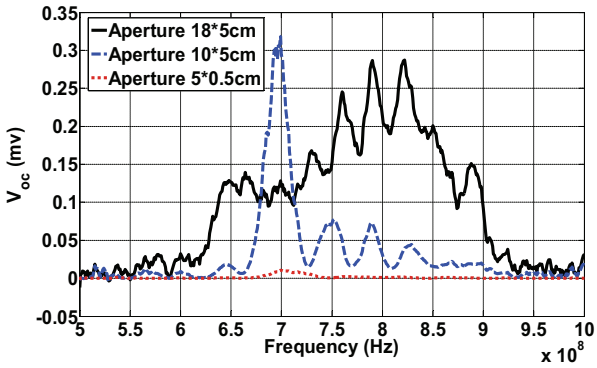

Fig. 7. V_{oc} at the open port of the MTL of Fig. 4 (a), inside the 30×12×30 cm^3 enclosure with different apertures; CST simulations.

In addition to MTL with air cushion, an MTL with RO4003 substrate (Fig. 4 (b)) is studied using CST as the simulation tool. Figure 8 compares the calculated V_{oc} and the measurements. A very good agreement between the results is clear in the figure. As observed, using the shield does not have a significant effect on reducing the induced V_{oc} on the MTL and the maximum value of V_{oc} for shielded and unshielded cases remains the same, occurring at different frequencies. Please be reminded that for the MTL with air cushion, the induced $V_{oc}$was multiplied when the shield was used. It means dielectric substrate with permittivity more than 1 can maintain the immunity of the MTL in an enclosure with large aperture, in the order of the unshielded case. As an

ending conclusion, using an enclosure with large apertures to protect systems against electromagnetic interference degrades the immunity of the system and should not be used definitely.

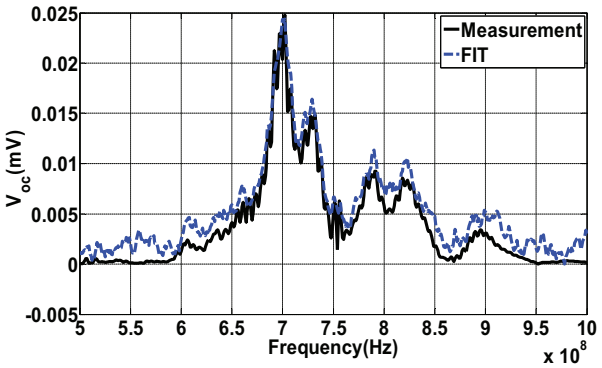

(a)

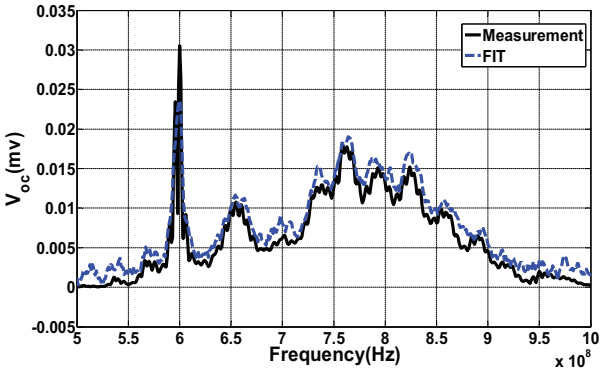

(b)

Fig. 8. Induced voltage on the open port of MTL with RO4003 substrate of Fig. 4 (b) by measurements and CST: (a) unshielded MTL and (b) shielded MTL.

B. Time domain analysis

Time domain results can be calculated by applying an Inverse Fourier Transform (IFFT) on the frequency domain data [26]. To this end, first, the interfering time domain signal should be transformed to frequency domain. Figure 9 illustrates a frequency domain, Gaussian plane wave with the center frequency of 750 MHz. The considered enclosure, MTLs and their location are the same as described in the previous sub-section. For the aperture size of 18×5 cm^2, time-domain V_{oc} for both MTLs of Figs. 4 (a) and (b) is depicted in Figs. 10 and 11, respectively. Please note that IFFT is implemented with 512 points.

As observed in Figs. 10 and 11, the level of the induced voltage on the shielded MTL is larger than the case where no shield is used.

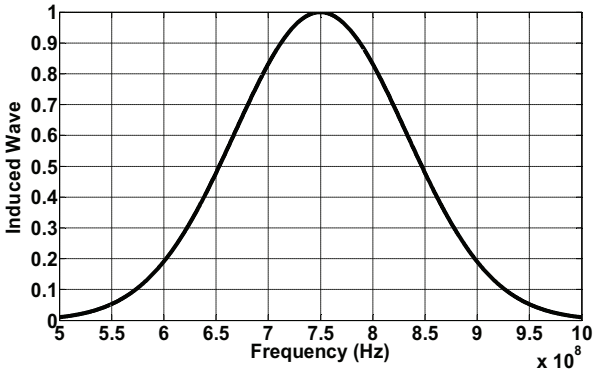

Fig. 9. Gaussian incident plane wave.

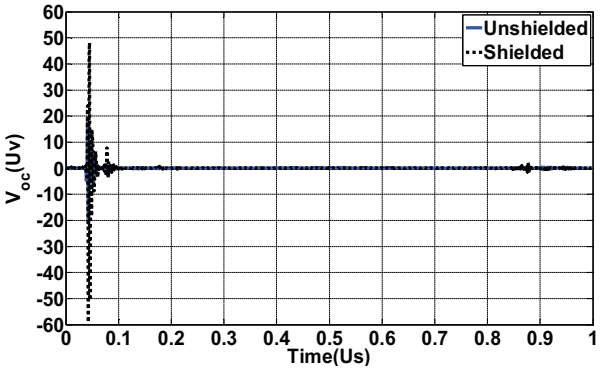

Fig. 10. Time domain V_{oc} comparison for shielded and unshielded MTL with air cushion of Fig. 4 (a).

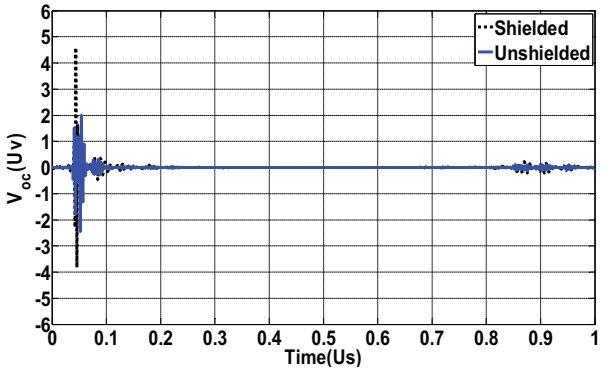

Fig. 11. Time domain V_{oc} comparison for shielded and unshielded MTL with RO4003 substrate of Fig. 4 (b).

In order to be able to compare the time domain results, Root Mean Square (RMS) value of the

induced V_{oc} is considered. RMS voltage is obtained according to [27] by:

$$V_{oc}^{rms} = \sqrt{\frac{\sum_{i=0}^{i=n}(V(t_i))^2}{n}}, \quad (5)$$

where $V(t_1)$, $V(t_2)$, …, and $V(t_n)$ are the induced voltages at *n* time instances of t_1, t_2, …,t_n. Table 1 compares the RMS V_{oc} values for the shielded and unshielded MTLs of Fig. 4.

Table 1: RMS value of induced time domain V_{oc} for the shielded and unshielded MTLs

	V_{oc}^{rms} (μv) Shielded case	V_{oc}^{rms} (μv) Unshielded case	$\frac{V_{oc}^{rms}(shielded)}{V_{oc}^{rms}(unshielded)}$
MTL with air caution	3.4397	1.0724	3.21
MTL with RO4003 substrate	0.2337	0.1583	1.48

As compared in the table, V_{oc}^{rms} of the shielded MTLs is higher than the case where no shield is used. In addition, the ratio of V_{oc}^{rms} for the MTL with air cushion (3.21) is about 2 times larger than that of the MTL with RO4003 substrate (1.48). It is also worth noting that for any case (shielded or unshielded) the induced V_{oc}^{rms} on the MTL with air cushion is larger than that on the MTL with dielectric substrate; i.e., the MTL with air caution is more susceptible to the external field.

IV. CONCLUSION

In this paper, susceptibility of a matched MTL against an interfering plane wave is studied. The induced voltage on the open port of the MTL is considered as a measure for the MTL susceptibility. Two different cases are considered; once the bare MTL is illuminated by the interfering field and then in order to hinder electromagnetic wave, the MTL is placed inside a shielding enclosure. Two MTLs with air cushion and RO4003 substrate were studied. For the MTL with air substrate, a RWG-MoM solution code was developed, while for the MTL with dielectric substrate, CST simulation was applied.

Both simulations were validated by the measurements performed in an anechoic chamber. It was shown that a large size aperture degrades susceptibility of the MTL at a large bandwidth compared to the case where no shield is used. As the aperture size is reduced, SE improves and this disagreeable effect decreases. However, at the enclosure resonance bandwidth, care should be taken of the immunity of the MTL, especially when the aperture size is large.

In addition, it was observed that for the MTL with dielectric substrate, maximum induced voltage remained the same as the case where no shield was used; however, a shift occurred in the frequency of the maximum voltage. For the MTL with air cushion, the induced voltage was very larger than that induced to the bare MTL.

In addition, the time domain effect was studied for an incident Gaussian wave on the shielded and unshielded MTLs.

REFERENCES

[1] R. P. Clayton, "Introduction to electromagnetic compatibility," *John Wiley & Sons Inc.*, 2006.

[2] I. M. Mark and M. N. Edward, "Testing for EMC compliance, approaches and techniques," *John Wiley & Sons Inc*., 2004.

[3] Y. Rousset, V. Arnautovski-Toseva, C. Pasquier, K. E. K. Drissi, and L. Grcev, "Using feko software for analysis of radiated electric field by power converters," *22nd Annual Rev. of Prog. In Applied Computational Electromagnetics (ACES Conf.)*, Miami, USA, pp. 881-888, March 2006.

[4] F. Grassi, G. Spadacini, F. Narliani, and A. S. Pignari, "The use of feko for the modeling of test set-up for radiated susceptibility," *23rd Annual Rev. of Prog. In Applied Computational Electromagnetics (ACES Conf.)*, Verona, Italy, pp. 279-284, March 2007.

[5] A. Nejadpak and O. A. Mohammed, "Finite element physics based modeling of cross-talk effect on PCB traces," *28th Annual Rev. of Prog. In Applied Computational Electromagnetics (ACES Conf.)*, Columbus, Ohio, pp. 768-773, April 2012.

[6] M. Leone, "Radiated susceptibility on the printed-circuit-board level: simulation and measurement," *IEEE Trans. On EMC*, vol. 47, no. 3, pp. 471-478, 2005.

[7] S. Atrous, D. Baudry, E. Gaboriaud, A. Louis, B. Mazari, and D. Blavette, "Near-field investigation of the radiated susceptibility of printed circuit boards," *Proc. IEEE Int. Symp. on Electromagnetic Compatibility-EMC Europe*, Detroit, USA, pp. 1-6, September 2008.

[8] D. Jing and H. Guo, "Study on coupling characteristics for EM pulse into slotted shell of

loaded PCB," *Proc. IEEE Int. Conf. on Computer, Mechatronics, Control and Electronic Engineering (CMCE)*, HongGuo, China, pp. 398-401, August 2010.

[9] L. Tian-Hong and M. J. Alexander, "A method to minimize emission measurement uncertainty of electrically large EUTs in GTEM cells and FARs above 1 GHz," *IEEE Trans. On EMC*, vol. 48, no. 4, pp. 634-640, 2006.

[10] H. Tarhini, M. E. Haffar, C. Guiffaut, G. Andrieu, A. Reineix, B. Pecqueux, and J. C. Joly, "Susceptibility of printed circuit boards in complex electromagnetic environment," *Proc. IEEE Int. Symp. on Electromagnetic Compatibility-EMC Europe*, Detroit, USA, pp. 1-4, September 2008.

[11] T. Namiki and K. Ito, "Numerical simulation using ADI-FDTD method to estimate shielding effectiveness of thin conductive enclosures," *IEEE Trans. on Microwave Theory and Techniques*, vol. 49, no. 6, pp. 1060-1066, 2001.

[12] J. Chen and J. Wang, "A three-dimensional semi-implicit FDTD scheme for calculation of shielding effectiveness of enclosure with thin slots," *IEEE Trans. On EMC*, vol. 49, no. 2, pp. 354-360, 2007.

[13] P. Dehkhoda, A. Tavakoli, and R. Moini, "Shielding effectiveness of a rectangular enclosure with finite wall thickness and rectangular apertures by the generalized modal method of moment," *IET Science, Measurement and Technology*, vol. 3, no. 2, pp. 123-136, 2009.

[14] M. Khorami, P. Dehkhoda, R. Moini, and H. H .S. Sadeghi, "Fast shielding effectiveness calculation of metallic enclosures with apertures using a multi-resolution method of moments technique," *IEEE Trans. On EMC*, vol. 52, no. 1, pp. 230-235, 2010.

[15] S. Yenikaya and A. Akman, "Hybrid MOM/FEM modeling of loaded enclosure with aperture in EMC problems," *International Journal of RF and Microwave Computer-Aided Engineering*, vol. 19, no. 2, pp. 204-210, 2009.

[16] B. Audone and M. Balma, "Shielding effectiveness of slots in rectangular cavities," *IEEE Trans. On EMC*, vol. 3l, no. l, pp. 102-106, 1989.

[17] D. W. P. Thomas, A. C. Denton, T. Konefal, T. Benson, C. Christopoulos, J. F. Dawson, A. Marvin, S. J. Porter, and P. Sewell, "Model of the electromagnetic field inside a cuboidal enclosure populated with conducting planes or printed circuit boards," *IEEE Trans. On EMC*, vol. 43, no. 2, pp. 161-169, 2001.

[18] K. Murano, T. Sanpei, F. Xiao, C. Wang, Y. Kami, and J. L. Drewniak, "Susceptibility characterization of a cavity with an aperture by using slowly rotating EM fields: FDTD analysis and measurements," *IEEE Trans. On EMC*, vol. 46, no. 2, pp. 169-177, 2004.

[19] C. Feng and Z. Shen, "A hybrid FD–MoM technique for predicting shielding effectiveness of metallic enclosures with apertures," *IEEE Trans. On EMC*, vol. 47, no. 3, pp. 456-462, 2005.

[20] S. Abadpour, P. Dehkhoda, H. R. Karami and R. Moini, "Aperture size effect on the susceptibility of a PCB inside an enclosure," *IEEE Int. Conf. on Electromagnetics in Advanced Applications*, Torin, Italy, pp. 741-744, September 2011.

[21] R. F. Harrington, "Time harmonic electromagnetic fields," *McGraw-Hill*, New York, 1961.

[22] S. M. Rao, D. R. Wilton, and A. W. Glisson, "Electromagnetic scattering by surfaces of arbitrary shape," *IEEE Trans. On Antennas and Propagation*, vol. 30, pp. 409-418, 1982.

[23] T. Weiland, "A discretization method for the solution of Maxwell's equations for six-component fields," *Electronics and Communication (AEÜ)*, vol. 31, pp. 116, 1977.

[24] Z. Rahimi, "The finite integration technique (FIT) and the application in lithography simulation," *Technical Department, University of Erlangen-Nuremberg*, Ph.D., 2011.

[25] D. M. Pozar, "Microwave engineering," *Wiley*, 2005.

[26] J. G. Proakis and D. K. Manolakis, "Digital signal processing, principles, algorithms and applications," *Prentice Hall*, 2006.

[27] A. V. Oppenheim, R. W. Schafer, and J. R. Buck, "Discrete-time signal processing," *Prentice-Hall*, 1999.